Università Politecnica delle Marche
Scuola di Dottorato di Ricerca in Scienze dell'Ingegneria
Curriculum in Ingegneria Industriale

Microgrid scale Liquid Air Energy Storage: plant optimization and thermal characterization of phase change materials for High Grade Cold Storage

Ph.D. Dissertation of:
Emiliano Borri

Advisor:
Prof. Gabriele Comodi

Coadvisor:
Asst. Prof. Alessandro Romagnoli

XVII edition - new series

Università Politecnica delle Marche
Scuola di Dottorato di Ricerca in Scienze dell'Ingegneria
Curriculum in Ingegneria Industriale

Microgrid scale Liquid Air Energy Storage: plant optimization and thermal characterization of phase change materials for High Grade Cold Storage

Ph.D. Dissertation of:
Emiliano Borri

Advisor:
Prof. Gabriele Comodi

Coadvisor:
Asst. Prof. Alessandro Romagnoli

XVII edition - new series

Università Politecnica delle Marche
Scuola di Dottorato di Ricerca in Scienze dell'Ingegneria
Facoltà di Ingegneria
Via Brecce Bianche – 60131 Ancona (AN), Italy

Alla mia famiglia

Acknowledgments

I would like to express my gratitude to my supervisor Prof. Gabriele Comodi for offering me this experience. I'm glad to have had this research opportunity which has contributed significantly to expand my knowledge and gave me the opportunity to study around the world. I would like to thanks to my mentor Prof. Giovanni di Nicola that first introduced me to the scientific research and gave me precious advice before to start this experience. Thanks also to Dr. Alessandro Romagnoli to welcoming me at the Nanyang Technological University of Singapore and gave me the opportunity to collaborate with your team. With your support, I had the opportunity to dress a lab coat and carry out a huge part of my work.

Many thanks also to Dr. Yongliang Li to gave me the opportunity to spend time with his group at the University of Birmingham. I'm glad to have been part of your team in the place where the research on liquid air energy storage began. Alessio, I'm glad for collaborating on this project with you, we spent a lot of effort together and we become good friends since the beginning. The destiny wanted that we were also flatmates but that's another story.

Thanks, Jia Yin for your kindness and your support. During my Ph.D., it was a pleasure to collaborate in the NTU lab with you. Out of the work, you are my mentor of the Singaporean culture and I'm glad for being welcomed in your wonderful family and feel like your Italo-Singaporean nephew.

Thanks, Andrea and Francesco, colleagues and good friends since I've started university. It was amazing to be part of the same group during our Ph.D. and share beautiful moments together in and out of the work. Thank you, Michele, I hope I was a good co-advisor for your thesis. I would like to thanks also Manuel, Stefano, Haoxin, Fadhel and all the NTU team for the support. Thanks also to my greek mate Argyris, Lucia, Marco, Serena, Rob and all the Birmingham friends. Thank you, Matteo, with which I've started my Ph.D. I've always admired your strength and your effort in science, and I wish you a brilliant career. Thanks also to all the "PhD and more" lunch crew.

I would like to thanks my Ph.D. friend and old flatmate "Liutone" for his support and his precious advise every time I need to do choice. Thank you Marco Sbaragna and Sir Alberto to always support me even at a distance while I was abroad. Thank you, Marco, since we have met in Istanbul, you always influenced me with your positivity.

I would like to thanks all the people that I've met in Singapore and become part of my life. Henny, our passion for the music started an amazing friendship and a lot of adventures together.

Thank you for your positive vibes and your support. Tommy Padang, if Singapore was an amazing experience it was also thanks to you. Thank you for welcoming me in the Nobel House and for your support. I hope that the Bidlis will tour again together in another part of the world. I would like to thanks also all the "Nobel Ladies" Trini, Valentina and Erica to stand me and Tommy together. I would like to thanks all the "Penangians": Peppe Panjang, Maurizio Pasir, Fabio Villa, Paolo Ban Mian, Ramesh, Pierre Baynan and FrancescoGelly. Thanks, Yunus to let me win Tavla just once. Thank you, Sumida, Ana Maria, Prachi, Rahul, Vani, Shaun, Jereon, Kim, Federico, Claudia, Rahul, Ania, Michele, Ezequiel and all the people that I've met in Singapore with which I've spent beautiful moments. Thanks also to the Tanglin Blues Club to have played together some good music. Last but not least thanks to my family for your support and patience.

Ancona, Novembre 2018

Emiliano Borri

Abstract

The increasing of the energy consumption related to the global energy demand is the main cause of environmental issues, such as greenhouse effect and climate change. The new policies related to the energy sector are aiming to a deep decarbonization of the grid that has led to reducing the energy produced from fossil fuels increasing the penetration of renewable energy sources in the actual energy system. The main drawback of clean energy sources is related to their unpredictable nature. The new challenge of the energy sector is then to overcome the problem related to the intermittency of renewable sources optimizing the balance between energy supply and energy demand. The use of energy storages has a fundamental role to guarantee the flexibility of the energy system capturing the wrong-time power from the renewables giving the possibility to be used in a later time or in a different place.

The large amounts of cold thermal energy wasted (from spare liquid nitrogen and LNG regasification) and the research of a new and sustainable energy vector have led to study the potential of cryogens on grid, transport and cooling applications defining a possible "liquid air economy". In the grid context, Liquid Air Energy Storage (LAES) is based on the concept that air at ambient pressure can be liquefied at -196°C, reducing the specific volume of around 700 times, to be stored in low-pressure vessels. The liquid air then can be expanded in a later time in a power producing device (e.g. turboexpander, reciprocating engine) to produce electric power.

The first concept son using the liquid air as storage medium was proposed in 1977 and again in the early 2000 but with no further developments. In 2005 University of Leeds and Highview Power patented a LAES system with a liquefaction system based on a Linde-Hampson cycle. The research starting from lab scale components has led to develop a 300kW/2.5MWh LAES pilot plant. The plant initially commissioned in April 2010 was located at Scottish and Southern Energy 80MW biomass plant at Slough Heat and Power in Greater London and now relocated at the University of Birmingham. In the recent years, the realization of the first pilot plant and the demonstration of the potential of cryogens as an energy vector, have led the LAES to attract the attention of many researchers due to their several advantages, such as long lifetime and no geological constraints. Furthermore, LAES can be easily scalable to large size due to the system made with existing mature components and sustainable ma-

terials. Although those benefits, the main disadvantage that compromises the LAES feasibility, is the low round-trip efficiency that is estimated around 50-60 % for large-scale systems. The most of the interest in the literature available is dedicated to industrial scale systems (up to 300 tons per day) to compete with large-scale technologies used for medium or long-term storage such as compressed air energy storage (CAES) and pumped hydroelectric (PHE). However, although a large portion of electric power produced still realize on large centralized systems, the energy system is moving towards to a decentralized energy production system with distributed energy resources (DER) and microgrids. The potential of the LAES technology and the related advantages make it interesting to investigate a small-scale (microgrid scale) that can be suitable for DER and microgrid applications as a medium or long-term energy storage.

In this work, a microgrid scale LAES is proposed defining a system that integrates a liquefaction plant with a daily production ranging between few tons and few tens of tons of liquid air. The aim of this work is to start the challenge of scaling down and reduce the size of the LAES contributing to the scientific community to understand the potential of this technology and inspire future research.
The first part of this thesis analyzes different liquefaction cycles, suitable for small-scale LAES with the aim to find an optimal configuration that minimizes the specific consumption of the plant. Indeed, the liquefaction cycle mainly affects the roundtrip efficiency of the system. The analysis, done by software simulation Aspen HYSYS, is based on parametric analysis and a comparison between the liquefaction cycles. A Kapitza cycle configuration with a two-stage compression working at supercritical pressures (over 40 bar), is the best cycle configuration that, if integrated to a pressurized phase separator, can achieve a specific consumption below 500 kWh/t. Furthermore, the high exergy loss at the compressor aftercoolers suggests that the integration of a waste heat recycle can increase the exergy efficiency of the system. Combining the system with a 105.5 kW single-effect water-Lithium Bromide absorption chiller the specific consumption of the microgrid scale LAES liquefier can be reduced of around 10%.

In the second part of the work, the Kapitza cycle has been integrated into a complete configuration of a microgrid LAES system that includes both the discharge section and the waste heat and cold thermal energy recovery system. A wide range of operating conditions has been assumed to evaluate the effect on the system performance. The results have been used to elaborated four performance maps to be used as a simple and immediate method that can be applied by engineers and researcher to estimate the LAES performance and optimize the design in terms of term of specific consumption, specific electric

power output, and round-trip efficiency.

The performance maps highlight that the reuse of the cold energy released by the liquid air before the expansion in the discharge cycle allows to improve the performance of the charge side of the LAES decreasing the specific consumption of the liquefaction cycle and increase the overall roundtrip efficiency of the system. Therefore, the last part of the thesis focuses on the High Grade Cold Storage (HGCS) that represents the main component of the waste cold recovery system. HGCS is fundamental to improve the performance the microgrid LAES and decrease the specific consumption of the liquefaction plant. To reduce the dimension of the storage increasing the energy density, a hybrid HGCS solution that integrates one or more part of phase change materials (PCM) has been proposed to improve the actual bulky solutions based on a sensible heat storage. The hybrid HGCS is part of a project based at TESLAB@NTU in the Nanyang Technological University of Singapore. The design of the storage using PCM requires a good understanding of the thermal behaviour of the storage medium during the charging and the discharging. Therefore, this work focuses on the thermal response and thermal characterization of PCM proposing a methodology to measure and predict the thermal behaviour of low temperature PCM. In particular, an experimental rig has been designed to measure the temperature in different points of a PCM placed inside a cylindrical shape container. The results are then used to validate a simple 1-D model that can be used to predict the thermal behaviour of different low temperature PCM. For this purpose, the container has been designed to obtain a similar thermal behaviour of the PCM involving a one-dimensional heat transfer process. The 1-D model has been calibrated and validated with the experimental results obtained with the melting and the solidification of pure deionized water. The reliability of the results has been verified with two different tests evaluating the solidification and the melting in different positions of the container. The methodology has been tested with a solution with a concentration of 30% of ethylene glycol (EG30) by weight in deionized water. Although aqueous alcohols are difficult to test due to their low latent heat and slow nucleation rate, the results of the 1-D model shows a good agreement with the experimental data representing a valid and simple method to approximate and predict the time of charge and discharge of the PCM and to compare the thermal profiles of different materials. Furthermore, the simplicity of the code allows the numerical model to be integrated into a more complex numerical model, particularly suitable for the complete modelling of HGCS.

Sommario

L'incremento del consumo energetico legato ad un forte aumento della domanda energetica mondiale, rappresenta la principale causa delle attuali problematiche ambientali legate al riscaldamento globale, come l'effetto serra e il cambiamento climatico. Le nuove politiche del settore energetico mirano ad una radicale decarbonizzazione della rete che ha notevolmente ridotto la produzione energia prodotta da fonti fossili, incrementando la penetrazione delle fonti rinnovabili. Il maggiore svantaggio di queste ultime è legato alla loro intermittenza e alla loro imprevedibilità. I nuovi obiettivi del settore energetico, sono quindi focalizzati nel risolvere le problematiche legate alle fonti rinnovabili e l'ottimizzazione del bilancio tra potenza prodotta e la domanda energetica. L'integrazione di sistemi di accumulo (energy storage) risulta quindi fondamentale per garantire la flessibilità del sistema energetico. Infatti questi ultimi hanno la capacità di accumulare la potenza elettrica per essere utilizzata in un tempo successivo.

Le grandi quantità di energia termica a temperatura criogenica dissipate nell'ambiente durante la rigassificazione del GNL (gas naturale liquefatto) e i grandi volumi di azoto liquido prodotto non utilizzato, hanno suggerito lo studio dei liquidi criogenici come vettori energetici alternativi che possono utilizzati sia essere mezzi di stoccaggio, ma anche applicati nel settore dei trasporti definendo una "liquid air economy". In questo contesto i sistemi LAES (Liquid Air Energy Storage) rappresentano un sistema di accumulo basato sul concetto che l'aria ambiente può essere liquefatta a -196°C riducendo il suo volume specifico di circa 700 volte, ed essere stoccata in serbatoi a bassa pressione. L'aria liquida può essere quindi utilizzata nuovamente, per produrre potenza elettrica mediante un espansore.

Alcune idee per utilizzare l'aria liquida come mezzo di stoccaggio sono state proposte nel 1977 e nei primi anni 2000, ma senza ulteriori sviluppi. Nel 2005 University of Leeds e Highview Power hanno brevettato un sistema LAES con un ciclo di liquefazione basato su un ciclo Linde-Hampson. Il progetto di ricerca ha portato allo sviluppo e alla realizzazione di un impianto pilota LAES con una potenza di 300 kW e una capacità di stoccaggio di 2.5 MWh. L'impianto, commissionato ad Aprile 2010, è stato inizialmente integrato con un impianto a biomasse di 80MW locato allo Slough Heat and Power di Greater London e successivamente rilocato a University of Birmingham. Negli ultimi anni, grazie

alla realizzazione del primo impianto pilota e alla dimostrazione potenziale dei liquidi criogenici come vettori energetici, il LAES è diventato oggetto di interesse di molti ricercatori grazie ai diversi vantaggi che la tecnologia offre, come la durata dell'impianto e l'assenza di vincoli ambientali. Inoltre il LAES può essere facilmente scalabile, grazie alla consolidata tecnologia basata su componenti già utilizzati in ambito criogenico. Il maggiore svantaggio, che compromette la fattibilità dei sistemi LAES, è la bassa efficienza che può essere stimata del 50-60 % per sistemi di larga scala. La maggior parte dell'interesse in letteratura è dedicato a sistemi di scala industriale con un ciclo di liquefazione basato su una produzione giornaliera di aria liquida maggiore di 300 tonnellate. Questi sistemi sono studiati per competere con i sistemi di accumulo energetico di larga scala di medio o lungo periodo come gli storage ad aria compressa (CAES) o i sistemi di accumulo con pompaggio di acqua (PHE).

Sebbene ancora una grande porzione di potenza elettrica viene prodotta da grandi sistemi centralizzati, negli ultimi anni il sistema energetico mondiale si sta muovendo verso sistemi decentralizzati con le sorgenti di generazione distribuita (DER) e le microgrids. Il potenziale della tecnologia LAES e i suoi vantaggi, rendono interessante lo studio di un LAES di piccola scala (microgrid scale LAES) che può essere dedicato come sistema di accumulo di medio o lungo periodo per applicazioni di generazione distribuita e microgrid.

In questa tesi il microgrid scale LAES è stato proposto definendo un impianto che integra un ciclo di liquefazione con una produzione giornaliera di aria liquida da poche tonnellate a poche decine di tonnellate al giorno. L'obiettivo di questo lavoro è quello di intraprendere la sfida nel ridurre la scala di un sistema LAES contribuendo alla comunità scientifica a definirne le potenzialità e ispirare la ricerca a possibili lavori futuri.

La prima parte di questa tesi analizza diversi cicli di liquefazione, adatti per essere applicati ad un LAES di piccola scala, con l'obiettivo di trovare una configurazione ottimale che minimizza il consumo specifico. Il confronto dei diversi cicli di liquefazione è stato basato su una analisi parametrica eseguita tramite il software di simulazione Aspen HYSYS. Un ciclo Kapitza supercritico (oltre 40 bar) con un doppio stadio di compressione, risulta la migliore configurazione e, se integrato ad un serbatoio di aria liquida pressurizzato, il consumo specifico stimato può essere inferiore ai 500 kWh/t. Inoltre, l'analisi exergetica, evidenzia una grande porzione di exergia persa durante l'interrefrigerazione tra i due stadi di compressione che suggerisce l'integrazione di un sistema di recupero dell'energia termica ad alta temperatura. Combinando il ciclo di liquefazione con un ciclo ad assorbimento a singolo effetto basato su un ciclo con acqua e bromuro di litio (LiBr), il consumo specifico del microgrid scale LAES può essere ridotto del 10%.

nella seconda parte del lavoro, il ciclo di liquefazione Kapitza è stato integrato

in una configurazione completa del microgrid scale LAES che include sia la sezione di scarica, che i sistemi di recupero dell'energia termica ad alta e bassa temperatura. Una analisi parametrica del sistema è stata eseguita assumendo un' ampia variazione delle condizioni operative del sistema valutandone l'effetto nelle prestazioni e nell'efficienza finale. I risultati, sono stati usati per elaborare quattro mappe di performance. Queste possono essere usate come un semplice strumento che può essere usato per stimare l'efficienza del sistema LAES e trovare le configurazioni ottimali che migliorano il consumo specifico, la potenza prodotta e l'efficienza globale dell'impianto.

Lo storage termico a bassa temperatura o "High Grade Cold Storage" (HGCS) è il componente principale del sistema di recupero di energia termica a bassa temperatura che risulta fondamentale per migliorare le prestazioni del microgrid LAES e diminuire il consumo specifico del ciclo di liquefazione. Per ridurre le dimensioni del sistema di accumulo termico incrementando la densità energetica, una soluzione di HGCS ibrida è stata proposta in questo lavoro. Lo storage ibrido è parte di un progetto basato al TESLAB@NTU nella Nanyang Technological Uuniversity di Singapore, e prevede l'integrazione di una o più parti di materiali a cambiamento di fase (PCM) nelle attuali soluzioni di HGCS basate su sistemi di accumulo termico a calore sensibile.

Il design dei sistemi di accumulo termico che utilizzano PCM, richiedono la conoscenza del comportamento termico del mezzo di stoccaggio durante le fasi di carica e scarica. Questa tesi si focalizza nella caratterizzazione termica dei materiali a cambiamento di fase a bassa temperatura, proponendo una metodologia che può essere utilizzata per misurare e prevedere il comportamento termico dei PCM.

In particolare un apparato sperimentale è stato progettato per misurare la temperatura in differenti punti di un PCM contenuto in un contenitore cilindrico. I risultati sono stati quindi usati per validare un semplice modello 1-D che può essere utilizzato per prevedere il comportamento termico di PCM a bassa temperatura. Per questo obiettivo, il container è stato progettato per ottenere dal PCM un comportamento simile ad un processo di trasferimento di calore monodimensionale.

il modello 1-D è stato calibrato e validato con i risultati sperimentali ottenuti con la carica e la scarica di acqua deionizzata. L'attendibilità dei risultati è stata verificata con due test differenti, valutando la solidificazione e lo scioglimento in differenti punti del container. La metodologia è stata quindi testata con diverso PCM basato una soluzione di glicole etilenico (EG) dissolta con una concentrazione del 30% in acqua pura. Le soluzioni alcoliche acquose risultano difficili da testare a causa del basso valore di calore latente (o entalpia di fusione) e la bassa velocità di nucleazione. I risultati ottenuti con il modello 1-D, mostrano una buona corrispondenza con i dati sperimentali. Il metodo

proposto risulta quindi essere un valido e semplice strumento per approssimare e prevedere il tempo di carica e scarica di diversi PCM e confrontare i differenti comportamenti. Inoltre, la semplicità del codice numerico, permette a quest'ultimo di essere facilmente integrato in modelli numerici più complessi ed essere utilizzato per un modello completo dello storage termico a bassa temperatura.

Contents

List of Figures

List of Tables

Chapter 1.

Introduction

Energy is part of our all-day life. The rising number of developing countries and the growth of population has led our society to become strongly dependent on energy sources with an increase the global energy demand. EIA reports that from the year 2015 the world energy consumption is expected to increase of 28% until 2040[1]. Nowadays, the energy consumption is the major contribution of the greenhouse effect accounting the 80% of CO2 emissions with the energy produced by fossil fuels that still accounts the fourth-fifth of the total energy production[2]. The policies related to environmental sustainability, energy security, and climate change are leading to a radical transformation of the energy sector aiming to achieve a deep decarbonization of the grid. The strongest evidence of the energy transition is represented by the shifting of the energy production from fossil fuels towards to clean and sustainable sources of energy. In 2016, renewables represent the 18.2% of the energy production with an increase of the generating capacity in 2017 by 9% over 2016[3]. The cost of solar photovoltaics and wind systems had a rapid decrease in the last few years and today accounts the main power capacity additions to the grid. The main challenge of a low carbon network is to design an energy system able to support a high penetration of renewable energy sources (REs). One of the main drawback related with the REs is their “non-dispatchable” behavior due to their unpredictable nature that generates a mismatch between the power supply and power demand. Capturing the wrong-time power from the renewables with the use of energy vectors, the energy can be stored and used in a later time or different place. In this context, the integration of energy storage (either thermal or electrical) has a fundamental role to overcome those challenges and guarantee the flexibility of the energy system. Strbc [4] highlights the importance of energy storage in shaping the energy demand in the context of the "demand side management", where they can use in peak shaving or load leveling strategies. Indeed, the wrong time energy stored can be used, for example, to cover the energy demand during the peak periods that would be otherwise displaced by the fossil fuels.

1.1. Energy storage classification

According to Chen et al.[5], electrical energy storages (EEs) can be classified with two different criteria: function and form. In terms of function storages can be divided (Figure 1.1) in storages suitable for high power ratings (to guarantee power quality) and storage that can be used for energy management. The classification by from can divide EEs into:

- Electrical energy storage
  - Electrostatic energy storage (Capacitors and supercapacitors)
  - Magnetic/current energy storage
- Mechanical energy storage
  - Kinetic energy storage
  - Potential energy storage
- Chemical energy storage
  - Electrochemical energy storage (batteries)
  - Chemical energy storage (fuel cells)
  - Thermochemical energy storage
- Thermal energy storage
  - Low temperature energy storage (Aquiferous cold energy storage, cryogenic energy storage)
  - High temperature energy storage (sensible heat systems such as steam or hot water accumulators, graphite, hot rocks and concrete, latent heat systems such as phase change materials)

In order to balance the gap between energy supply and energy demand, the traditional solutions rely on the use of hydro plants [6], suitable for a grid with a small number of large power plants. The decentralization of energy production and the increasing number of small power plants affects the needs of more

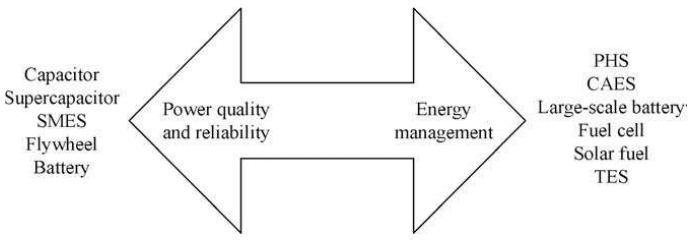

Figure 1.1.: Classification of energy storage by function, Chen et al. 2009

flexible and sustainable systems. In this case, the chemical energy storages such as batteries and fuel cells, are able to provide high storage efficiency, but they are costly and their lifetime (10-15 years) is shorter compared to other storage technologies. When the storage life is over, the materials need to be recycled and processed increasing the economic and the environmental costs. Nowadays, two mature solutions, sustainable and long lifetime is represented by Pumped Hydro (PHE) and Compressed Air Energy Storage (CAES). PHE can be classified in the category of mechanical/potential energy storage; in those systems, water is pumped from two different reservoirs at two different height levels. When the power is needed, the potential energy of the water at the higher level is converted into electrical energy by means of a turbine. Those systems can achieve an efficiency of around 70-80 % [6]. On the other hand, CAES uses the low-cost or wrong time power to produced compressed air to be stored in pressurized vessels located in underground caverns. The compressed air is then heated using natural gas or waste heat sources and expanded in a turbine to generate electricity. A thermodynamic analysis conducted by Grazzini et al. [7]on a CAES system shows that it is possible to achieve a round trip efficiency of 72% if the heat generated during the compression is recovered and reused during the discharge phase. The main disadvantage that strongly limits the applicability of those two technologies, is represented by the geographical constraints. An alternative to CAES and PHE is represented by Liquid Air Energy Storage (LAES) systems that use cryogens as the energy vector.

1.2. Introduction to LAES

LAES is based on the concept that air at ambient pressure can be liquefied at -196°C, reducing the specific volume of around 700 times, to be stored in unpressurized vessels. The liquid air then can be expanded in a later time in a power producing device (e.g. turboexpander, reciprocating engine) to produce electric power. The potential of the high grade cold thermal energy as energy vector is investigated by Li et al.[8] that proposed four different systems based on Rankine and Brayton cycles to efficiently use the energy from cryogens. Indeed the use of liquid air allows operating with an energy vector with a higher energy density compared with the compressed air (150-250 Wh/kg vs. 30-60 Wh/kg) that allows reducing the storage dimension compared, for example, to CAES [5].

The advantage of LAES can be resumed as [9]:

- Low capital cost ($ 200-400 per kWh that could decrease to 150-250 per kWh)
- Low lifetime cost ($ 150-250 per MWh)
- Easy scalability of the system
- Long lifetime (30 years)
- No geological constraints
- System made with existing mature components and sustainable materials
- Possibility to be integrated with other industrial process plant and systems (Hybrid LAES)

Although those benefits, the main disadvantage that compromises the LAES feasibility, is the low round-trip efficiency that can be estimated at around 50-60% for large-scale systems [10]. A LAES system can be considered made of three main parts as shown in Figure 1.2: a charge section, a storage section, and a discharge section.

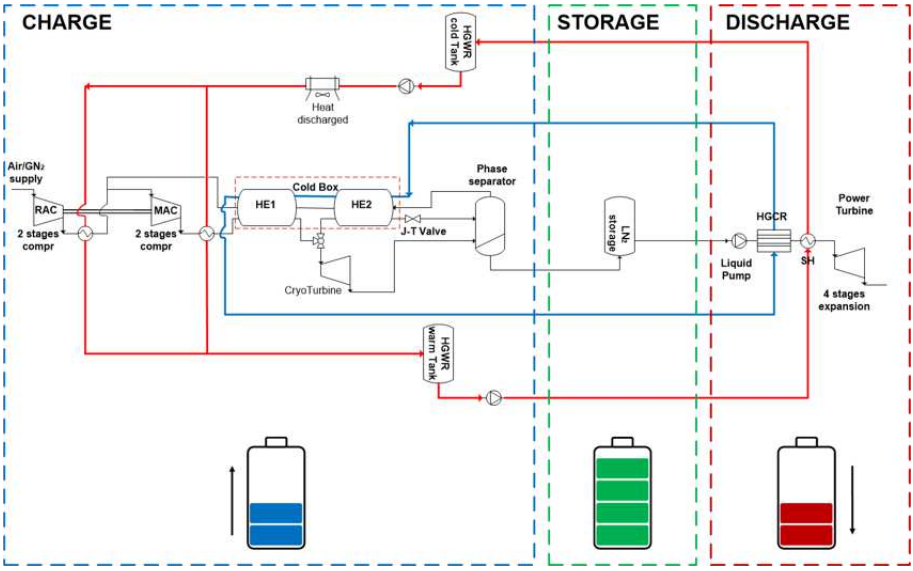

Figure 1.2.: Schematic of a stand-alone LAES

The charge section includes the liquefaction cycle used to produce liquid air during a surplus of power produced from renewable energy or during the off-peak period when the price of electricity is cheaper. The liquefaction of gases

is a mature process mainly applied to decrease the specific volume of gases to be easily stored and transported in different locations. One of the most common applications is, for example, the liquefaction of natural gas (LNG). The simplest liquefaction process is the Linde-Hampson cycle (described in detail in the next Chapter) where the liquefaction of the gas is based on the isenthalpic expansion through a Joule-Thomson valve. The low efficiencies of the Linde-Hampson cycle have lead to some modification which, the most popular, is represented by the Claude cycle that combines the isenthalpic and the isentropic expansion by means the introduction of a cryogenic expander to the cycle. The most efficient process used in the gas liquefaction is the cascade process and the mixed refrigerant process mainly used to produce LNG[11]. A cascade cycle used different gases with different liquefaction temperatures to better match the cooling curve the LNG increasing the efficiency of the entire process reducing the work required for the gas liquefaction. Each gas is cooled down by means of a vapor refrigeration cycle. The mixed refrigerant process has a similar principle to the cascade cycle, but in this case, different gases are mixed together. Those solutions, although are more efficient, they present high maintenance cost and the higher number of components leads to a longer start-up phase of the liquefaction cycle, that leads the current LAES solutions to be mostly based on a Linde or Claude based liquefaction cycle. The storage section of the LAES stores the liquid air produced by the charge section in unpressurized or low pressurized insulated vessels. The discharge section allows, in a later time, to recover the energy stored in the liquid air. Li et al.[8] compare different methods to extract the energy from cryogens that are: direct expansion, Rankine Cycle, and Brayton cycle. In the direct expansion, the liquid air extracted from the tank is pumped at high pressure and heated to the ambient temperature (or higher if a waste heat source is available) and then expanded one or more turbines to produce electric power for the final user. In the case of the Rankine cycle, the cold thermal energy is used to cool down and liquefy, through a condenser, another fluid that works in a separate Rankine cycle. In the Brayton cycle that uses gas turbines and engines to produce electric power, the cryogen is used to reduce the specific work of compression reducing the temperature at the inlet. The results of the study affirm that the best solution depends on the heat source available. Indeed, if a high-grade heat source is available, a combination with a Brayton and direct expansion results in the most efficient way. On the other hand, with a low-grade heat source, a combination of direct expansion and Rankine cycle results in a lower power consumption in the compression process resulting attractive when also carbon capture is considered. The actual LAES solutions are mostly based on a direct expansion method. The work of by Li et al.[8] classified the direct expansion method inefficient due to a large amount of cold

Table 1.1.: Specific Consumption of the Highview Pilot Plant and Commercial Scale LAES

	Pilot Plant (30 tons per day and 300 kW output)	Commercial Scale (>300 tons per day and 10 MW output)
Liquefaction Plant	0.6-0.75 kWh/kg	0.4 kWh/kg
Liquefaction plant + Cold Recycle via High Grade Cold Storage	0.45-0.55 kWh/kg	0.2 kWh/kg

energy wasted to the environment. Actually, if the energy extraction of cryogen is considered in a LAES system, the cold energy released by the evaporation of the liquid air can be recovered and used to help and improve the performance of the liquefaction cycle in the charge side of the LAES. In this case, a system of *waste cold recycle* is integrated to the LAES, including a heat transfer fluid that recovers the cold thermal energy and stores it into a High Grade Cold Storage (HGCS). The cold thermal energy can be later used it to support the liquefaction of air. Table 1.1 reports the results of the specific consumption from the data available from Highview Power [9]. The results show that the specific consumption can be reduced of around 25% (from 0.6-0.75 kWh/kg to 0.45-0.55 kWh/kg) in the case of the pilot plant with a liquid air production of $\tilde{3}0$ tons per day and of 50% in the case of the commercial scale (from 0.4 kWh/kg to 0.2 kWh/kg). A similar concept can be applied on the charge section of the LAES integrating a *waste heat recycle*. In this case, the hot thermal power released from the compression, instead to be wasted to the ambient, is recovered and stored in a High Grade Warm Storage (HGWS) to be later used to increase the temperature at the inlet of the turbines in the discharge section of the LAES.

1.2.1. History of the LAES

The first concept of using the liquid air as storage medium was proposed in 1977 by Smith [12]. In the system, shown in Figure 1.3.

During the operation, the liquid air, supplied from an additional liquefaction cycle, is pumped through the regenerator to cool down the system. During the off-peak periods, ambient air (A) is compressed by means of a two-stage compressor. After the first stage of compressor (B), the compressed air with a pressure of around 7 atm is cooled down in a regenerative heat exchanger first (C) and a freon refrigeration plant to be dehumidified at a temperature of 5°C. The dry air is then heated up first in the condenser of the refrigeration cycle (E) and successively by mean of the regenerative heat exchanger, reaching

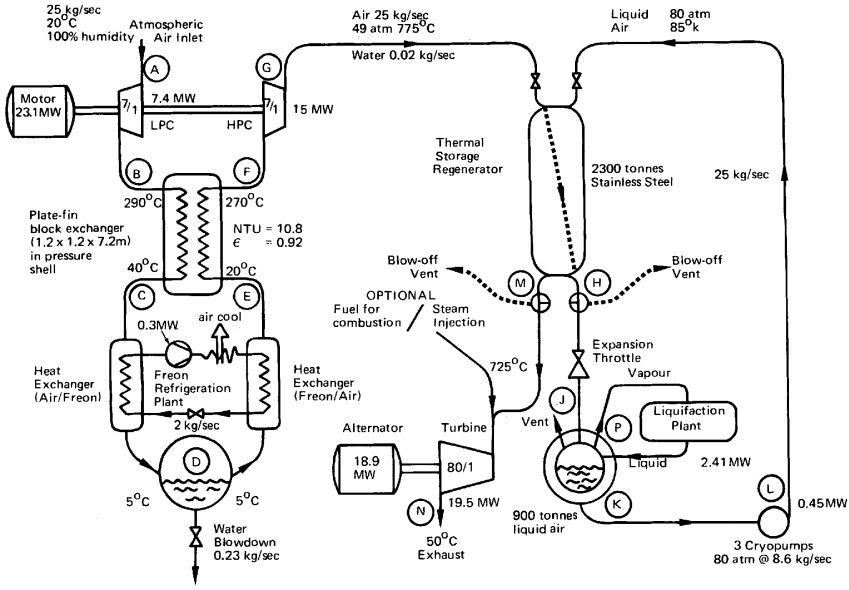

Figure 1.3.: Schematic of the cryogenic energy storage proposed by Smith

a temperature of 270 °C. The hot pressurized air is then cooled down in the regenerator (H) precooled with liquid nitrogen and liquefied by means of an expansion throttle (J). The regenerator is then heated at a temperature of around 800 °C. When power is needed the liquid air stored in the tank, is pumped at high pressure (80 atm) and heated up in the regenerator before being expanded in a turbine. Although the roundtrip efficiency estimated, can be as high as 75%, the system has many critical areas mainly limited from the cycle temperature. Indeed the design of a regenerator operating between the two extreme temperatures (-200°C and 800°C) and high pressures, is the main critical part that compromises the reliability of the system. The second work proposed in the literature was from Chino and Araki at Hitachi in early 2000. Chino et al.[13] proposed a system that uses the liquid air produced by means of a Claude cycle during the off-peak period time to feed a combustor of a gas turbine during the daytime. Starting from the Smith's concept, Araki[14] proposes a simpler version of the regenerator that consists of an array of small diameter stainless-steel pipes with concrete filled around as storage medium. An experimental rig was also developed to validate a numerical model, but with no future developments.

(a) *External view of the LAES pilot-plant*

(b) *Internal view of power container of the LAES pilot-plant*

Figure 1.4.: Highview power LAES pilot-plant located at university of Birmingham

In 2005 University of Leeds and Highview Power[9] patented a LAES system with a liquefaction system based on a Linde-Hampson cycle. In this system, the air is expanded in a power turbine without being integrated into a combustion process and a low pressure cold thermal energy storage is integrated to the LAES to recover the cold thermal energy wasted during the regasification of the liquid air in the discharge process. The research starting from lab scale components has lead to developed a 300kW/2.5MWh LAES pilot plant (Figure 1.4). The plant initially commissioned in April 2010 and located at Scottish and Southern Energy SSE's 80MW biomass plant at Slough Heat and Power in Greater London. The first prototype was only made of a liquid nitrogen

tank and a power turbine, able to process the 47% of the low-grade waste heat (60°C) from the biomass plant into electrical power. The liquefaction plant, with a liquid production rate of around 1.4 tonnes per hour, was later commisioned realizing the first LAES prototype in the world for a total cost of 3.253.538 pounds [9]. The pilot plant also includes a waste cold recovery section where the cold thermal energy from the liquid air is recovered, using dry air as the storage medium, in a High Grade Cold Storage based on a packed bed configuration made of quartzite rocks. The concept of *waste cold recycle* system is mainly designed to simplify the system and reduce the total cost of the plant.

1.2.2. LAES and the "liquid air economy"

With a focus on the UK energy system, a full report published in 2013 from the Centre of Low Carbon Futures (CLCF) [10] evidences the need of a new energy vector to overcome the problem related to the intermittency of the renewables (and balancing the energy supply and demand) and transform the electricity produced with low carbon sources, in a form suitable for transport. Furthermore, the increasing of cooling demand, mainly due to the rising number of developing countries, has to lead to consider different ways to produce and deliver cold in a sustainable way. A smarter way to produce cold is also moved by the fact that a lot of cold energy is wasted to the environment from industrial processes. Indeed, since air is composed by 72% of nitrogen, all the gases industries that separate and liquefies air products for over a century, waste a large amount of liquid nitrogen that could be exploited, for example, to fuel transports. The second major source of waste cold is the LNG regasification. Centre of Low Carbon Futures estimates, that the LNG imports in the UK will rise in 30 billion cubic meters in 2030 and, if the cold wasted from the regasification were exploited in the air liquefaction, it could produce around 8 million tonnes of liquid air per year [10]. In this case, liquid air has been considered a potential sustainable energy vector for the grid, transport, and cooling. In an energy system based on "liquid air economy" the liquid air has the main role to satisfy at the same time more than one energy needs. This can be feasible, today with the progress on the research and development of liquid air technologies and the market evolution. In the context of the "liquid air economy", LAES is the key technology to produce the liquid air and balance the energy supply and energy demand of a grid based on energy produced with low carbon sources. Furthermore, LAES can be used as a sink of waste cold and waste heat thermal energy. An example in the full report of CLCF proposes the LAES as the core of an industrial park as shown in Figure1.5.

In this context, the LAES can be charged with the off-peak electricity from

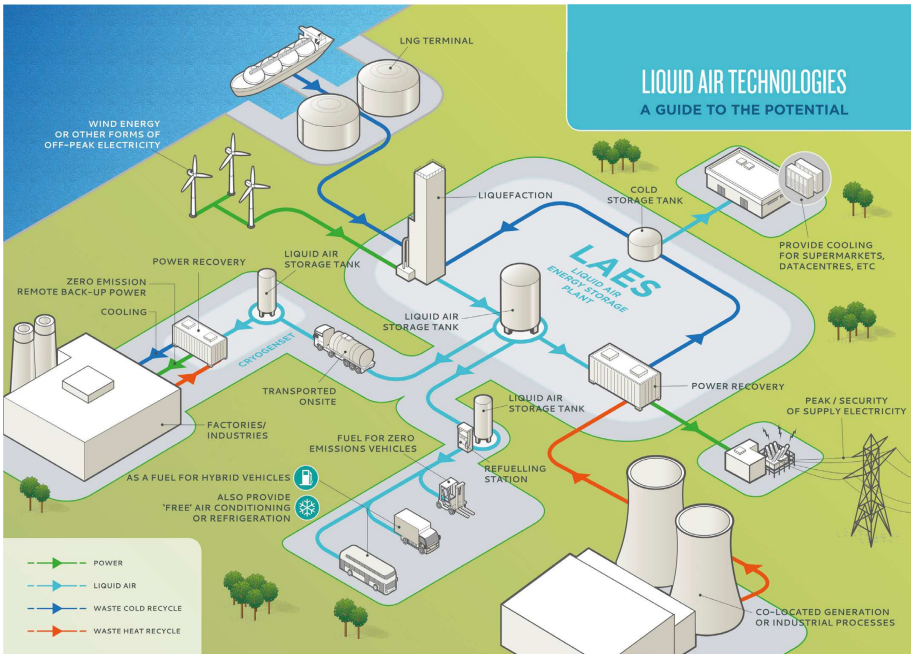

Figure 1.5.: Industrial park intergrating LAES, Centre for Low Carbon Futures 2013

renewables, and if located next to an LNG terminal, the specific consumption can be reduced using the waste cold energy coming from the LNG regasification. The liquid air stored in the LAES tank can be used to produced electric power at peak times or extracted for different applications such as transport and cooling. Furthermore, the small specific volume, allows the possibility to be transported and be used to different sites for different porupses.

1.2.3. Literature review of LAES

The potential of the liquid air as energy vector and energy storage medium attracted the attention of many researchers on the study of LAES systems. This is evidence can be noticed in the numbers of works published in the scientific literature. Most of the literature available focuses on the thermodynamics of the system with the aim to find an optimal configuration and maximize storage efficiency. Ameel et al.[15] conducted a thermodynamic analysis of a LAES based on a Linde-Hampson cycle combined with a Rankine cycle reaching an efficiency up to 43.3% for an ideal case. could be achieved. Guizzi et al.[16] carried out a thermodynamic analysis of a LAES in which they considered a recovery section for the hot and cold energy; the analysis showed that a round trip efficiency of 50% could be achieved and that the most critical component is the

turbine of the liquefaction side. A similar work was conducted by Xue et al.[17] where the integration of a cold and hot thermal energy storage allows achieving a LAES roundtrip efficiency of 47%. Vandoor and Expansion Energy[18] patented a cycle to store liquid air in which the waste heat of compression is used to drive an absorption refrigeration cycle that acts as an intercooler and an aftercooler to the compressor. Abdo et al.[19] compared different systems for storing liquid air. Starting from the method proposed by Chen et al. [20], two different options based on the Claude and Collins cycles were assessed. Although these two cycles present lower specific consumption than that proposed by Chen et al.[20], the Claude cycle appears to be the best option from a techno-economic perspective. A comparison of the LAES with other large-scale storage technologies has been carried out by Krawczyk et al.[21] and Georgiou et al.[22] where the system is compared with CAES and PHES respectively. An economic analysis of the LAES was conducted by Xie et al.[23] by using a genetic algorithm. The results show that the integration of waste heat and the increasing of the system size can increase the system economic profitability with a payback period that could vary from 25.7 years to 5.6 years for a 200 MW system. Tugberk et al. [24] studied the potential of a LAES integrated to a geothermal power plant. The results show that LAES can be a good option for load shifting of the geothermal power plant, estimating an overall efficiency of the system of 24.4%.

Hybrid LAES Solutions

In order to increase the system efficiency of the LAES, different solutions have been proposed in the literature that hybridizing the storage with other energy systems to increase the overall efficiency. Pimm et al.[25] proposed a hybrid energy storage combining a CAES and a LAES system, developing an algorithm to find the maximum profit available from the hybrid system proposed. A thermodynamic analysis of the same hybrid solution has been conducted by Kantharaj et al.[26]. The results of the work show, that integrating a heat pump/heat engine in the system is possible to achieve a roundtrip 53% to convert compressed air to liquid air and back. Farres-Antunez et al. [27] proposed a combination of LAES and PHE where the round trip efficiency of the entire system can be increased of 10% compared to the individual technologies. Li et al. [28] proposed a solution integrating a LAES in a nuclear power plant. The liquid air is produced during off-peak hours and used to produce energy during peak hours. The thermal energy of the nuclear plant in the power extraction process is used to superheat the liquid air during the discharge phase of the LAES achieving a round trip efficiency up to 70%. Kim et al.[29] proposed a hybrid LAEs combined during the expansion with natural gas as fuel. The work compared the hybrid system in terms of thermodynamic, environmental,

and economic performances. The system proposed is able to reach roundtrip efficiencies as high as 73.4 % and a storage efficiency of 64.2% with a maximum levelized cost of energy of 190 $/MWh that depends on the system scales and storage time. The hybrid solution has also been compared with CAES and adiabatic LAES systems. Antonelli et al.[30] conducted a thermodynamic analysis of different hybrid LAES configuration that integrates Organic Rankine Cycle (ORC) cycle and Brayton cycle. The solution proposed, (with and without natural gas combustion) are compared with the LAES baseline case. The results report that a hybrid solution allows reaching efficiency as high as 80% with a fuel utilization of 100%. The combination of LAES with ORC cycle has also been proposed by She et al. [31] and Peng et al.[32]. The cycle integrates also a vapor compression refrigeration cycle as a heat sink. the thermodynamic analysis results show that the round-trip efficiency can be increased of 9-18% with the solution proposed compared to the baseline LAES. A similar approach has been conducted by Tafone et al. [33]. In this case, a LAES system has been integrated with a waste heat recovery system that includes an ORC cycle, to produce useful electric power, and an absorption chiller to reduce the specific consumption of the liquefaction cycle. Barsali et al.[34] proposes a hybrid LAES analyzed through a thermodynamic analysis, where during the liquefaction cycle only oxygen is liquefied. This can be used in the discharge phase in an oxy-combustion chamber with natural gas as fuel. Optimized arrangements of the system proposed are able to reach round trip efficiencies higher than 90%. Zhang et al. [35] proposed a hybrid LAES where the heat of compression is used to drive a two-stage ORC. the system is coupled with an LNG source to assist the liquefaction process and an external heat source is applied to increase the efficiency of the ORC, achieving a total roundtrip efficiency of the system of 45.44%.

Trigeneration LAES

LAES hybrid solutions are adopted to increase the performance of the system increasing the power output of the discharge section or reducing the specific consumption of the liquefaction cycle. Actually, the waste heat and the waste cold thermal energy of the system allows the LAES to provide heating, cooling, and electric power. The potential of the LAES for cooling applications has been investigated by Comodi et al.[36] where different systems are compared. Al-Zareer et al.[37] proposes a LAES with a waste heat recovery integrated to provide district heating and cooling by mean of an absorption chiller. Tafone et al.[33] investigated a hybrid LAES with ORC and absorption chiller in a trigenerative configuration, where the high utilization of waste heat can improve the round trip efficiency of 30%.

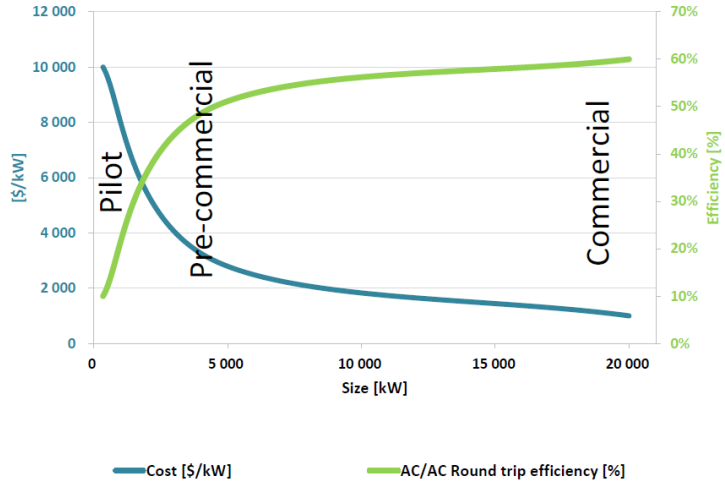

Figure 1.6.: Estimated cost of LAES based on the size of the plant

1.3. Characteristics of microgrid scale LAES and aim of this work

In the literature reported, most of the interest is dedicated to industrial scale LAES (with a liquid air production up to 300 tons per day) to compete with large-scale energy storage technologies such as CAES and PHE. There are mainly two reasons that have to lead the actual research on large-scale LAES. The first reason regards the application, indeed large-scale energy storages can be integrated into an energy system based on extensive centralized energy production plants. Furthermore, large scale is more suitable to be coupled with a waste heat source from industrial sites such as the LNG regasification terminals where plenty of waste cold, that could be used to produce liquid air, is available. Highview Power, for example, has been working on the development of a LAES that can deliver around 5MW/15MWh – to significantly more than 50MW/200MWh [9]. The other advantage of large-scale LAES is due to the higher round-trip efficiency and the reduction of the capital cost when the LAES is scaled-up. Figure1.6 shows that, at the actual state of research, the cost of the plant increase at small size due to the poor efficiency estimated.

However, although a large portion of the electric power produced still realize on large centralized systems, the energy system is moving towards to a decentralized energy production system with distributed energy resources (DER) and Microgrids. DER refer to a small source of electric power that is connected directly to the power system distribution and directly consumed by the user. The

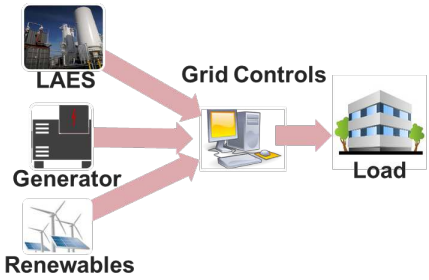

Figure 1.7.: Small-scale LAES integrated to a Microgrid

term "microgrid", proposed by the Consortium for Electric Reliability Technology Solutions, defines as multiple systems of DER, controls and final user able to enhance the local reliability and flexibility of the system[38]. The interest to move on decentralized systems is their ability to reduce the transmission cost of the electricity and allow a better integration with the energy produced from renewable sources. A microgrid system supplied with REs must guarantee the balance between the supply and the energy demand. Therefore in this context, energy storage is a fundamental component. The potential of the LAES technology and the related advantages make it interesting to the investigation of a small-scale (microgrid scale) that can be suitable for DER and microgrid applications as shown in Figure1.7. The novel term of microgrid scale LAES proposed in this work defines a system that integrates a liquefaction plant with a daily production ranging between few tons and few tens of tons of liquid air, that corresponds to a size of air liquefaction plant between the lab and industrial scale. The aim of this work is to start the challenge of scaling down and reduce the size of the LAES contributing to the scientific community to understand the potential of this technology and inspire future research.

When scaling down the LAES, the high specific consumption of the liquefaction cycle mainly affects the final value of the roundtrip efficiency of the system. Chapter 2 aims to investigate the liquefaction plant configuration that minimizes the specific consumption of a microgrid scale LAES. In particular different liquefaction cycles, suitable for the small scale, are analyzed and compared by mean of simulation software and an optimal configuration that minimizes the specific consumption is proposed. At the end of the chapter, a novel solution to recover the waste heat of compression is proposed to reduce the specific consumption of the microgrid LAES liquefaction plant with the integration of a LiBr-water absorption chiller. A complete configuration of microgrid LAES is presented in Chapter 3. The system has been modeled and a parametric analysis has been conducted varying the main operative parameters and analyzing the key performance parameters of the LAES system. The

results, that consist of a large amount of data, have been elaborated and novel performance maps are proposed. The four maps proposed, can be a useful tool to assist the design of microgrid scale LAES offering a simple graphical method to estimate the performance of the system. Chapter 4 and Chapter 5 focus on the waste cold recycle of the system, in particular on the design of the High Grade Cold Storage (HGCS). The actual solutions of HGCS are packed bed sensible heat storage characterized by a low energy density and bulky in terms of dimensions. The idea proposed in this work is to integrate into the HGCS, one or more part of phase change materials (PCMs) to increase the storage energy density and reduce the dimensions. The design of a hybrid HGCS is part of a project done in collaboration with TESLAB@NTU based in the Nanyang Technological University of Singapore consisting of different steps. In this work, the task of thermal characterization of low temperature PCM for the hybrid HGCS has been afforded. In particular, the aim was to address a methodology to measure the thermal response and predict the thermal behavior of low temperature PCM. In particular, an experimental rig has been designed to test the thermal response. The results obtained have been used to validate a 1-D numerical model that can be used to predict the thermal behavior of the PCM. Due to their well-known properties, the methodology has been first validated using pure deionized water as PCM materials. Then the methodology has been tested and further validated to on a sub-zero PCM material based on aqueous ethylene glycol solution. The last chapter of this work reports the overall conclusions and ideas that can be addressed for future works.

Chapter 2.

Preliminary study on a microgrid scale LAES air liquefaction plant

All the literature published on LAES system highlights that the high specific consumption of the liquefaction process represents the main hurdle which adversely affects the LAES round trip efficiency. Since the plant size has a significant impact on the liquefaction process, the aim of this part of the work mainly lies in the following aspects:

- To analyze and compare the main cycles used for air liquefaction that can be used to a small-scale LAES
- To find an optimal configuration and operating range aiming at minimizing the specific consumption
- Propose a solution to improve the efficiency of the liquefaction cycle decreasing the specific consumption
- The liquefaction plant considered for a microgrid scale is supposed to produce 10 tons/day hypothesizing a LAES charging process of 12 hours.

2.1. Optimal configuration and operating range of a "microgrid scale" LAES air liquefaction plant

The present study contributes to provide a preliminary analysis for the estimation of the specific consumption of small-scale liquefaction plants and to suggest an optimal configuration with an optimal operating range to be used as a guideline for future researches and applications of LAES in microgrid and demand side applications. The most common plants used for the air liquefaction are first described and then compared by means of a parametric analysis conducted by simulation by means of the software Aspen HYSYS. The comparison is based on the evaluation of the specific consumption, the component efficiency and an exergy analysis. An additional case study for air liquefaction cycles considering a pressurized phase separator is evaluated. At the end of this section a results and comments are reported and an optimal configuration for a microgrid scale LAES liquefaction cycle is suggested.

2.1.1. Introduction to the air liquefaction cycles

One of the first air liquefaction cycles was patented in 1985 by Linde and Hampson. An ideal Linde-Hampson cycle consists of an isothermal compressor, a heat exchanger, a Joule-Thompson (J-T) valve and a phase separator. Due to its irreversibility, the liquid yield is usually less than 10%. Variants of the Linde-Hampson consist of the precooled J-T and the dual pressure cycle [39]. The ideal Claude cycle derives from the Linde cycle and combines the isenthalpic expansion of the J-T valve and the isentropic expansion of an expander. The main variants of the Claude cycle are the Heylandt and the Kapitza cycle; the former is mainly used for high pressure liquefaction cycles whereas the latter is used for low operating pressures. Modern development of air liquefaction cycles make use of single mixed refrigerants process [11]. This process is also widely used in the natural gas industry [40] where the liquefaction is assisted by the vaporization of a mixture of different gases that better match the cooling profile of the natural gas. This leads to an increase in the performance of the liquefaction process but, on the other hand, its complexity and costs increase substantially. In the case of air liquefaction, the single mixed refrigerants process can be used in the Linde and in the Kapitza cycles to precool the air. In this chapter an analysis of the Linde-Hampson, Claude and Kapitza liquefaction cycles is conducted in order to find the configuration and the range of operating conditions that minimize the specific consumption of a small-scale air liquefaction cycle. The description of each cycle and the assumptions behind the simulations set-up are described below.

2.1.2. Materials and methods

Simulation of the processes

The simulation of Linde-Hampson, Claude and Kapitza liquefaction cycles were carried out using the software Aspen Hysys [41]. The boundary conditions used for the simulation of the cycles are given in Table 2.1.

Linde-Hampson process A Linde-Hampson cycle is shown in Figure 2.1 and is composed by a compressor (C-1), an aftercooler (AFTC), a heat exchanger (HEX-1), a J-T valve and a phase separator (PS). The ambient air is firstly compressed at high pressure (1-2) and then cooled down near ambient temperature (2-3). Then, the air passes through the heat exchanger (HEX-1) in which it is further cooled down (3-4) by the cold vapor recirculating from the phase separator (6-7). The J-T valve then completes the liquefaction process by expanding the air down to ambient pressure (4-5); this leads to a two-phase mixture which is then separated in the phase separator where the liquid air is extracted. The cold vapor (7) after passing through the heat exchanger (HEX-1) is then mixed with the ambient air at inlet of the compressor.

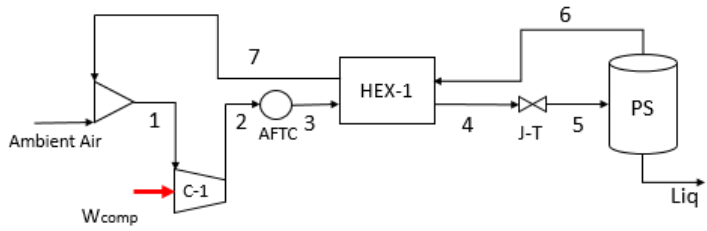

Figure 2.1.: Schematic of the Linde-Hampson liquefaction cycle

Claude process Unlike the Linde-Hampson cycle, the Claude cycle includes an cryoturbine (CT) and two more heat exchangers (HEX-2, HEX-3). As shown in Figure 2.2, the compression phase is the same as that of the Linde-Hampson cycle. After the high temperature heat exchanger (HEX-1) the main stream of air (4) is separated into two streams (5a) and (5b). The first stream (5a) passes through the medium temperature (HEX-2) and the low temperature heat exchanger (HEX-3) for then being expanded through the J-T valve; the resulting two-phase mixture is separated in the phase separator (PS), where the liquid air is extracted. The second stream (5b) is expanded directly through

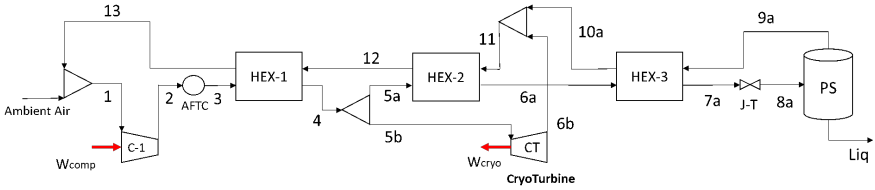

Figure 2.2.: Schematic of Claude liquefaction cycle

the cryoturbine (CT); the expansion (5b-6b) results in a temperature drop and a work output. The cold vapor leaving the cryoturbine (6b), is then mixed with the stream (10a) coming from the low temperature heat exchanger (HEX-3) in which the air from the compression process (6a) is further cooled down. In this cycle, it is important to evaluate the optimal recirculation fraction corresponding to the ratio of the mass flow going to the Joule Thomson valve (5a) to the total compressed mass flow (4); this parameter is influenced by the operating pressure.

Kapitza process The Kapitza cycle differs from the Claude cycle in that the low temperature heat exchanger (HEX-3) is removed. As shown in Figure 2.3, the compression phase is the same as the Linde-Hampson and the Claude cycle. After the high temperature heat exchanger (HEX-1) the main stream is separated in two flows (5a) and (5b). Unlike the Claude cycle, the first stream (5a) passes through one heat exchanger (HEX-2) before being expanded in the J-T valve and separated in the phase separator (PS), whereas the second stream (5b) is directly used to drive the cryoturbine. The cold air leaving the cryoturbine (6b) is mixed directly with the vapor coming from the phase separator (8a) and cools down the air in the low temperature heat exchanger (in this case HEX-2). Unlike the Claude cycle, the cold vapor (9) enters the heat exchanger (HEX-2) at higher temperature, thus affecting the final temperature of the air entering the J-T valve (6a) and hence the liquid air of the two-phase mixture (7a) entering the phase separator. Likewise the Claude cycle, in the Kapitza cycle is important to evaluate the optimal recirculation fraction.

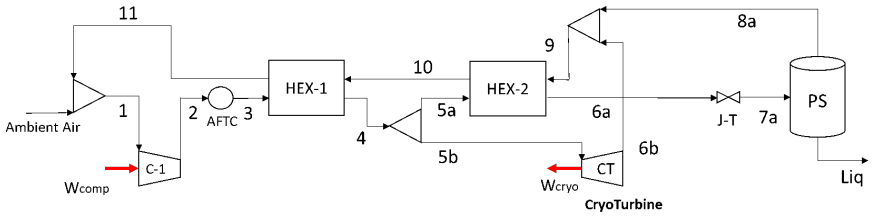

Figure 2.3.: Schematic of Kapitza liquefaction cycle

Simulation assumptions

In order to define an optimal configuration that minimizes the specific consumption for the liquid air production, the following assumptions have been made:

- cryogenic cycles are considered in steady flow conditions
- air is the main working fluid and properties are calculated by means of Aspen HYSYS
- the target liquid air production rate is assumed around 0.834 t/h (i.e. 10t/day considering an operating period of 12 hours per day for charging the LAES)

The optimization process consisted in a parametric analysis; in particular, two parameters were investigated: operating pressure and recirculation fraction (for Claude and Kapitza cycles). The range of operating pressures investigated during the analysis of the Claude cycle and the Kapitza cycle goes from 6 bar to 60 bar, that covers both the subcritical and supercritical conditions (critical pressure of the air is 37.7 bar). The lower value represents the typical operating pressure adopted in the air separation [42], while the higher value is adopted in high pressure gas liquefiers [43]. For the Linde cycle the range of operating pressures for the parametric analysis is different since the typical operating pressures for this cycle are around 200 bar; in the current study the pressure range considered is between 150 and 300 bar. For each cycle two different configurations are considered:

- One stage compression
- Two stage compression (with intercooling)

In the case of the two stage compression the pressure ratio and the adiabatic efficiency are assumed to be the same for both compressors in order to reduce the specific work. Table 2.1 summarizes the the boundary conditions for each cycle.

Table 2.1.: Boundary conditions for Linde, Claude and Kapitza cycles simulations

	Linde	Claude	Kapitza
AFTC outlet temperature	30°C	30°C	30°C
AFTC pressure loss	0.0 bar	0.0 bar	0.0 bar
Outlet J-T Valve pressure	1 bar	1 bar	1 bar
Cryoturbine outlet pressure	-	1 bar	1 bar
HEX pressure loss	0.0 bar	0.0 bar	0.0 bar
Compressor adiabatic Efficiency	85%	85%	85%
Cryoturbine adiabatic Efficiency	-	70%	70%
Minimum pinch point temperature difference			
HEX-1	5°C ±0.5	5°C ±0.5	5°C ±0.5
HEX-2	-	5°C ±0.5	3°C ±0.3
HEX-3	-	3°C ±0.3	-

From Table 2.1, it is possible to notice that the pressure losses along the cycle have been neglected in order to have a solution which compares different cycles under the same conditions. In addition to this, the specific consumption is calculated assuming a conservative value of the adiabatic efficiency of the cryoturbine compared to the actual cryoturbines used in the liquefaction process that reach adiabatic efficiencies up to 88% [44].

In order to compare the performance of the various cryogenic cycles the specific consumption is defined as follows:

$$\text{Specific consumption(SC)}[kWh/t] = \frac{W_{net}}{\text{hourly liquid air produced}} \tag{2.1}$$

where W_{net} is calculated as follows:

$$W_{net} = \sum_{i}^{n_c} W_{comp} - W_{cryoT} \tag{2.2}$$

where W_{comp} and W_{cryoT} are the work of the compressors (where n_c indicates the number of the compressors) and cryoturbine respectively.

The fraction of the liquefied air is represented by the liquid yield that is defined as follows:

$$\text{Liquid Yield} = \frac{\dot{m}_{LA}}{\dot{m}_{comp}} \tag{2.3}$$

where m_{compr} is the total mass flow rate of compressed air and m_{LA} represents the mass flow rate of the liquid air produced by the liquefaction cycle.

Exergy analysis

In order to evaluate the exergy efficiency of the different liquefaction cycles investigated and to study their critical components, the exergy analysis has been carried out. In general, the exergy balance equation in a closed volume control can be written as follows:

$$\sum_{in} Ex_{stream} - \sum_{out} Ex_{stream} + \sum_{i} Q_i \left(1 - \frac{T_0}{T_i}\right) - P_{net} - Ex_{loss} = 0 \tag{2.4}$$

Where the first two terms $\sum_{in} Ex_{stream}$ and $\sum_{out} Ex_{stream}$ are associated with the exergy of the streams entering and leaving the control volume; these can be defined as:

$$Ex_{stream} = \dot{m}_{stream} \cdot ex_{stream} = \dot{m}_{stream}[(h - h_0)] - T_0(s - s_0)] \tag{2.5}$$

Where m_{stream} is the mass flow rate $[kg/s]$, ex_{stream} is the specific exergy $[kJ/Kg]$, h represents the specific enthalpy $[kJ/kg]$ and s the specific entropy $[kJ/kgK]$ of the inlet and outlet streams. The terms h_0 ,s_0, T_0, are associated to the enthalpy, entropy and temperature at the reference state, that are the air thermodynamic properties at 25°C and 1 bar. The third term of Eq. 2.5 represents the exergy related with the heat transfer: Q_i is the thermal power, T_o is the temperature of the reference state and T_i is the exchange temperature at the boundary of the control volume. The fourth term P_{net} $[kW]$ represents the net power (electrical or mechanical) supplied to the system. In the exergy analysis, the system is assumed to be in steady state conditions and thermal losses in the heat exchangers are neglected. The exergy efficiency η_{ex} can be calculated for each liquefaction cycle as follows [11]:

$$\eta_{ex} = \frac{\dot{m}_{liq}(ex_{liq} - ex_{amb})}{P_{net}} \tag{2.6}$$

where ex_{liq} and ex_{amb} refer to the specific exergy related with the liquid air and with the ambient air respectively. The exergy loss Ex_{loss} can be calculated

by considering a control volume and applying the general exergy balance Eq. 2.5 to each component [11]. The equations used are summarized in Table 2.2 and the subscripts refer to the stream entering and leaving each component; the exergy loss in both phase separator and air mixers is neglected.

Table 2.2.: Exergy loss equations for each component of the liquefaction cycle

Component	Exergy loss balance equation
Compressor	$Ex_{loss} = Ex_{in} - Ex_{out} + P_{comp}$
AFTC	$Ex_{loss} = Ex_{in} - Ex_{out}$
Cryoturbine	$Ex_{loss} = Ex_{in} - Ex_{out} - P_{cryoT}$
HEX	$Ex_{loss} = (Ex_{in_{cold}} - Ex_{out_{cold}}) + (Ex_{in_{hot}} - Ex_{out_{hot}})$
J-T valve	$Ex_{loss} = Ex_{in} - Ex_{out}$

2.1.3. Results

Based on the methodology and assumptions described earlier, this section reports the main results of the parametric analysis. Figure 2.4 reports the results for the Linde-Hampson cycle in terms of specific consumption versus operating pressure.

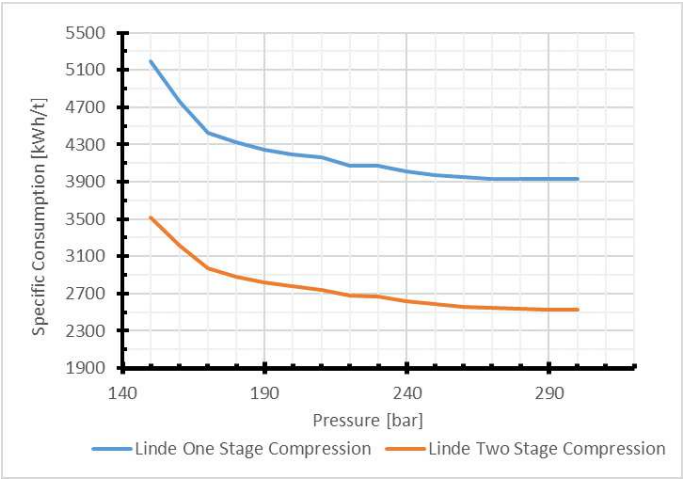

Figure 2.4.: Specific Consumption of the Linde-Hampson cycle at different operating pressures

The figure shows that the Linde–Hampson cycle should operate with high pressures in order to substantially reduce the specific consumption. The main reason for the low efficiency is due to the large temperature difference between the cold vapor and the air in the heat exchanger (HEX-1 in Figure 2.1) which leads to a significant loss in the whole cycle performance and in a low liquid yield that increases the specific consumption; the two stage compression instead shows that the specific consumption can be reduced by at least 25%.

Figure 2.5 reports the results for the Claude cycle with one stage compressor under different recirculation fractions and operating pressures. The lowest specific consumption ($\approx$ 900 kWh/t) occurs for 10 bar operating pressure and 0.1 recirculation fraction. For higher pressures both the specific consumption and the optimal recirculation fraction increase, meaning that more air should be expanded directly into the J-T valve. Indeed, the specific consumption of the cycle is affected by the heat exchangers performance that, in turn, depends on both the recirculation fraction and the operating pressure. The effects of the operating pressure and recirculation fraction on the heat exchangers performance are further discussed when the Kapitza cycle is described (Figure 2.9 and Figure 2.10).

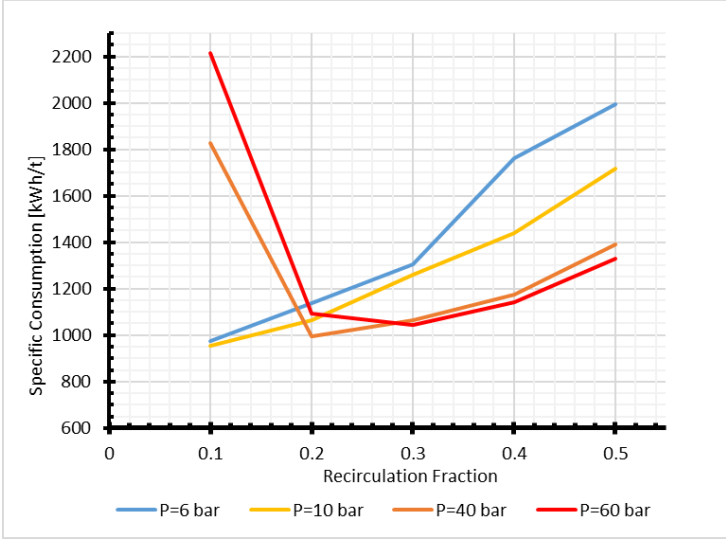

Figure 2.5.: Specific consumption of Claude cycle with one stage compression at different operating pressures

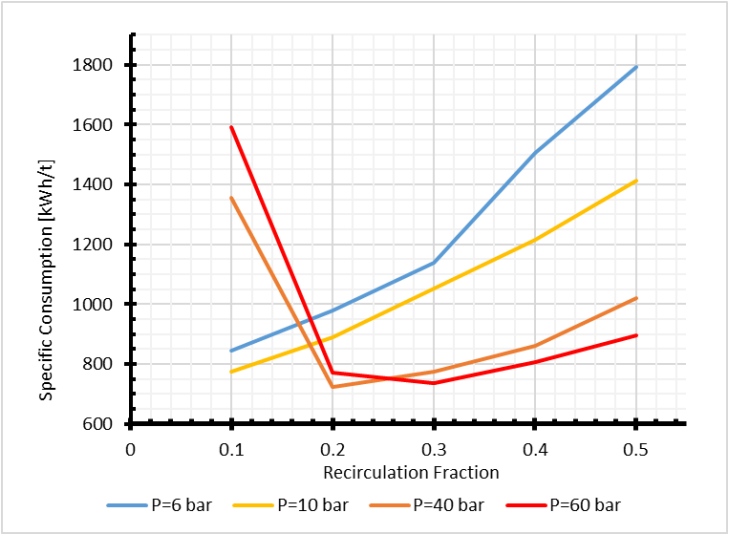

Figure 2.6.: Specific consumption of Claude cycle with two stage compression at different operating pressures

Figure 2.6 shows the case with two stage compression where the minimum specific consumption of around 720 kWh/t is achieved at 40 bar (supercritical pressure) and 0.2 recirculation fraction. For higher values of the operating pressure, the minimum specific consumption does not vary significantly.

Results from the Kapitza cycle for one and two stage compression are shown in Figure 2.7 and Figure 2.8 , respectively. In particular, the simulations show that for two stage compression, the minimum specific consumption decreases as compared with the one stage (from $\approx$ 900 kWh/t down to $\approx$ 700 kWh/t), with the minimum specific consumption occurring for higher operating pressures. As mentioned before, the specific consumption of the cycle is influenced by the heat exchangers performance and consequently by the operating pressure and the recirculation fraction: the higher the performance of the heat exchangers the higher the yield of the liquefaction plant. Moreover, in the case of the two stage compression cycles, the specific consumption is furtherly reduced thanks to the lower compression work resulting from the intercooling. Figure 2.8 shows that the minimum specific consumption for the two stage compression Kapitza cycle is achieved for subcritical pressure at 10 bar and recirculation fraction of 0.1 and for supercritical pressure at 40 bar and recirculation fraction of 0.2.

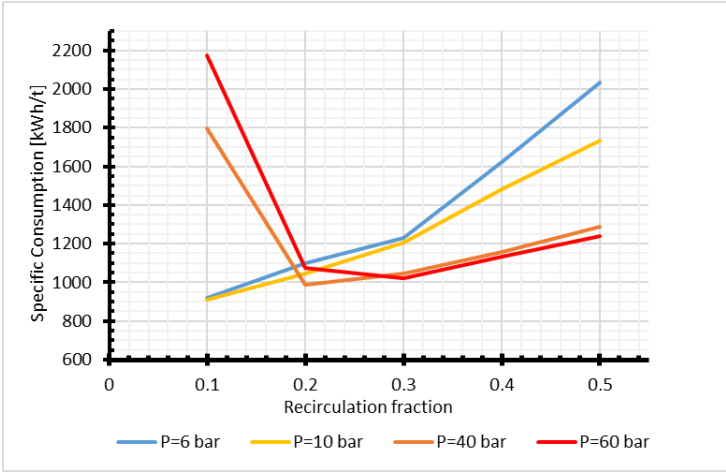

Figure 2.7.: Specific consumption of Kapitza cycle with one stage compression at different operating pressures

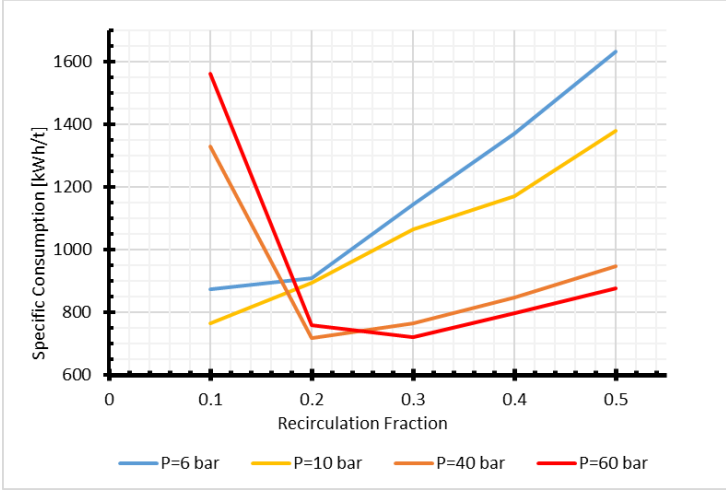

Figure 2.8.: Specific consumption of Kapitza cycle with two stage compression at different operating pressures

In order to understand the effect of both the operating pressure and recirculation fraction on the performance of the heat exchangers, Figure 2.9 and Figure 2.10 report, for the two stage compression Kapitza cycle, the temperature profiles of the two heat exchangers (HEX-1 and HEX-2) under different operating conditions. Figure 2.9 refers to the two cases of minimum specific consumption pointed out in Figure 2.8: the one occurring at subcritical pressure (Figures 2.9a and 2.9b) and the one occurring at supercritical pressure (Figures 2.9c and 2.9d). In particular, Figure 2.9 shows that the heat exchangers (HEX-1 and HEX-2) better perform in the supercritical Kapitza. Indeed, by comparing the temperature profile of both heat exchangers, it is apparent that, at supercritical pressure, the curve profile of the hot streams (3-4 and 5a-6a) better matches the curve profile of the cold streams (11-12 and 10-11a).

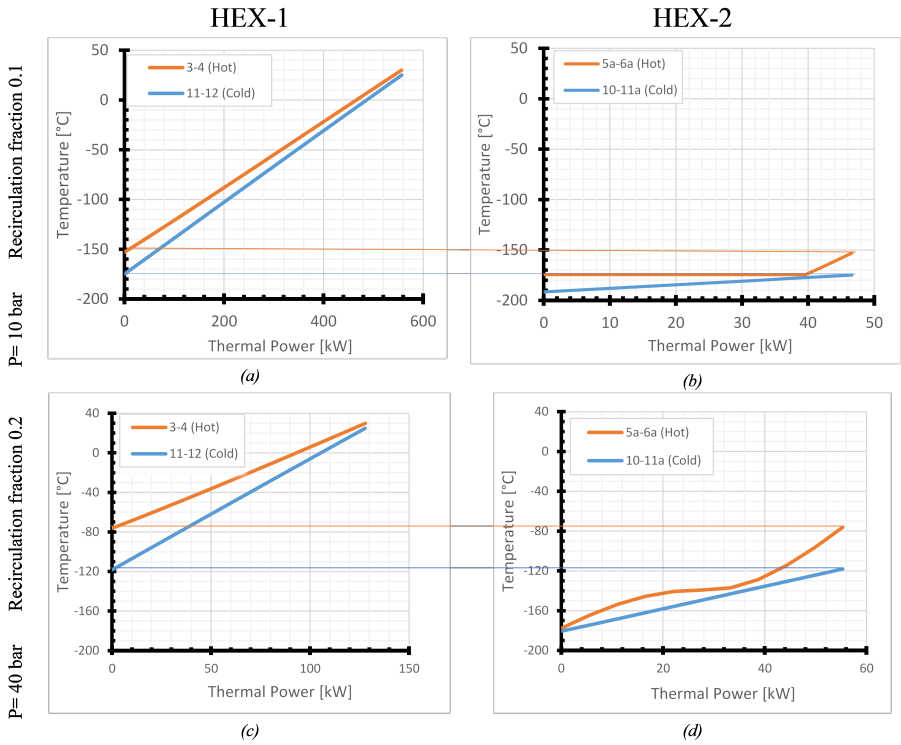

Figure 2.9.: Plots of the temperature profile of the Heat Exchangers HEX-1(a, c) and HEX-2 (b,d) of Kapitza cycle with two stage compression for 10 bar and 0.1 of recirculation fraction (a,b) and for 40 bar and 0.2 of recirculation fraction (c,d)

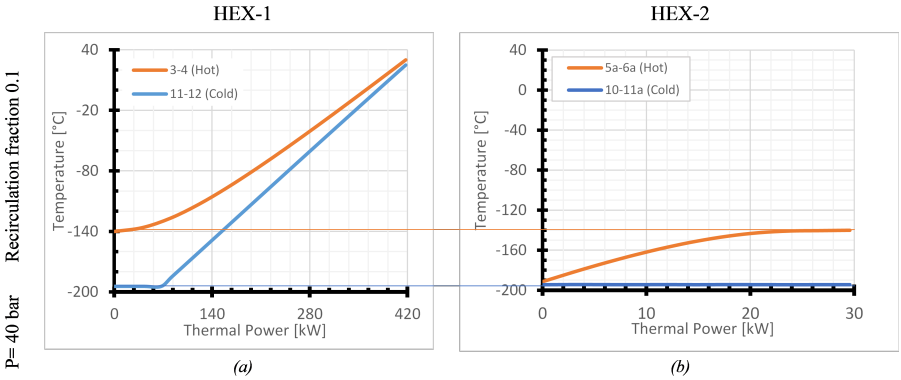

Figure 2.10.: Plots of the Heat Exchanger HEX-1 and HEX-2 profile of Kapitza cycle with two stage compression for 40 bar operating pressure and 0.1 of recirculation fraction

Figure 2.10 shows the behaviour of the two heat exchangers (HEX-1 and HEX-2) for an operating pressure of 40 bar but with a recirculation fraction of 0.1. This configuration allows the comparison between the subcritical Kapitza cycle operating at 10 bar and recirculation fraction of 0.1 with the supercritical Kapitza cycle operating at 40 bar with the same recirculation fraction: the comparison of Figure 2.9 (a,b) and Figure 2.10 shows that with a recirculation fraction of 0.1, the two heat exchangers (HEX-1 and HEX-2) perform better for the subcritical Kapitza as confirmed by the lower specific consumption shown in Figure 2.8. Figure 2.10 also allows the comparison of Kapitza supercritical cycle with different recirculation fraction: from Figure 2.9 (c, d) and Figure 2.10, it is apparent that, the 0.2 recirculation fraction improves the overall heat transfer reducing the specific consumption.

Figure 2.11 shows the total air mass flow rate, the two stage compressor power, the cryoturbine power and the specific consumption as a function of the recirculation fraction for a Kapitza cycle with two stage compression operating at 40 bar. Figure 2.11 highlights that the variation of the cryoturbine power is relatively small as compared with the two stage compressor power that is the parameter that mainly affects the specific consumption of the liquefaction process.

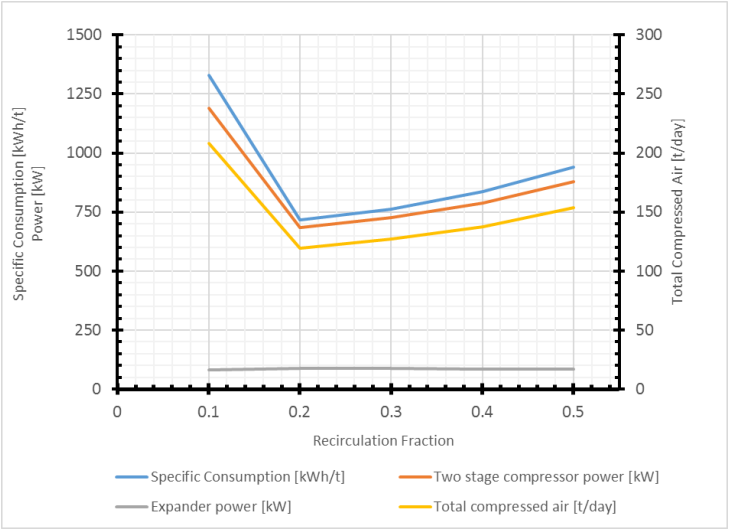

Figure 2.11.: Total air mass flow rate, Two stage compressor power, Cryoturbine power and specific consumption of the two stage compression Kapitza cycle for an operating pressure of 40 bar

Figure 2.12 shows the liquid yield as a function of recirculation fraction. The maximum liquid yield (16.7%) occurs with a recirculation fraction of 0.2; this is due to the high performance of the two heat exchangers (HEX-1 and HEX-2) as already shown in Figure 2.9c and Figure 2.9d. By increasing the recirculation fraction, the liquid yield decreases. Indeed, as shown in Figure 2.12, more mass of air is compressed in order to reach the final liquid production of 0.834 ton/hour, thus raising the final specific consumption.

Figure 2.13 reports a direct comparison between the specific consumption of the Claude and Kapitza cycles with two stage compression. From the results, the specific consumption of the two cycles is almost the same as it apparent by comparing Figures 2.5 and 2.7 (one stage compression) and Figures 2.6, 2.8 and 2.13 (two stage compression). Therefore, in order to understand the difference between the two liquefaction cycles it is necessary to investigate in depth the behaviour of the components, in particular the heat exchangers that are determinant for the cycle efficiency.

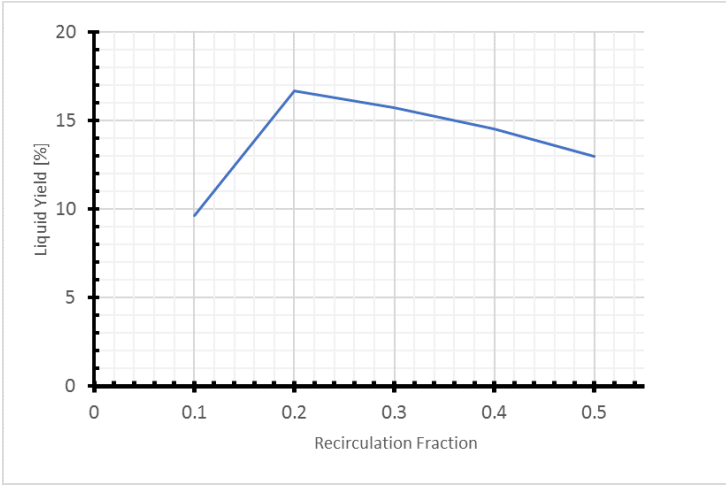

Figure 2.12.: Liquid Yield of the two stage compression Kapitza cycle for an operating pressure of 40 bar

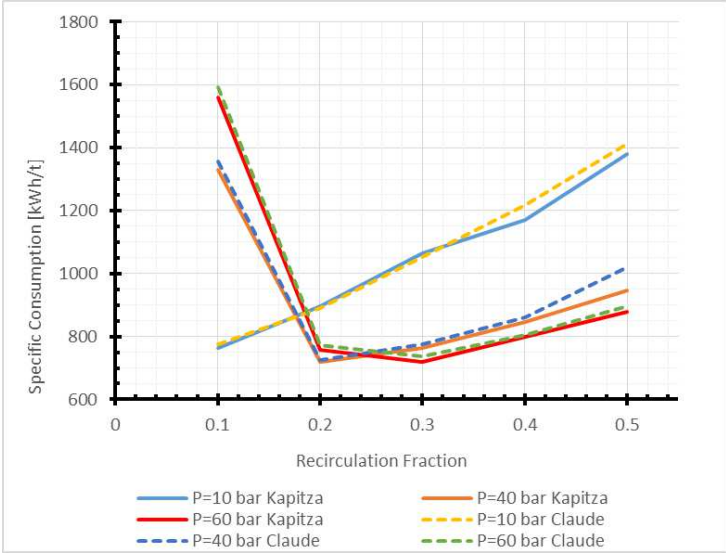

Figure 2.13.: Comparison of the specific consumption of Claude and Kapitza cycles with two stage compression at different operating pressures

With respect to the condition of minimum specific consumption presented in Figure 2.13 (two stage compression, operating pressure of 40 bar and recirculation fraction of 0.2), Figure 2.14 shows the temperature profile of the three heat exchangers of the Claude cycle. In more detail, Figure 2.14 a shows the heat flow profile of the high temperature heat exchanger (HEX-1); Figure 2.14 b shows the medium temperature heat exchanger (HEX-2), where is possible to notice a non-linearity of the curves due to the phase change inside the heat exchanger; Figure 2.14 c shows the heat flow profiles of the low temperature heat exchanger (HEX-3). In particular, Figure 2.14c highlights that the thermal power exchanged by HEX-3 is negligible. This can be explained by the fact that the mass flow rate of the cold stream in HEX-3 is significantly smaller than the one of the hot stream: the discrepancy between the mass flow rate of the two stream results in a small temperature drop of the hot stream and a substantial temperature rise of the cold stream; this represents an increase of irreversibility and a decrease of the performances.

With regards the two stage compression, a summary of the minimum specific consumption and an optimal range of operating conditions for each liquefaction cycle investigated is reported in the Table 2.3.

Table 2.3.: Summary of the optimal operating conditions range for two stage compression cycles

Cycle	Linde (two stage)	Claude (two stage)	Kapitza (two stage)
Operating Pressure [bar]	240-260	38-45	38-45
Recirculation Fraction Estimated	-	0.2-0.25	0.2-0.25
Specific Consumption (SC) [kWh/t]	2500-2600	720-730	710-720

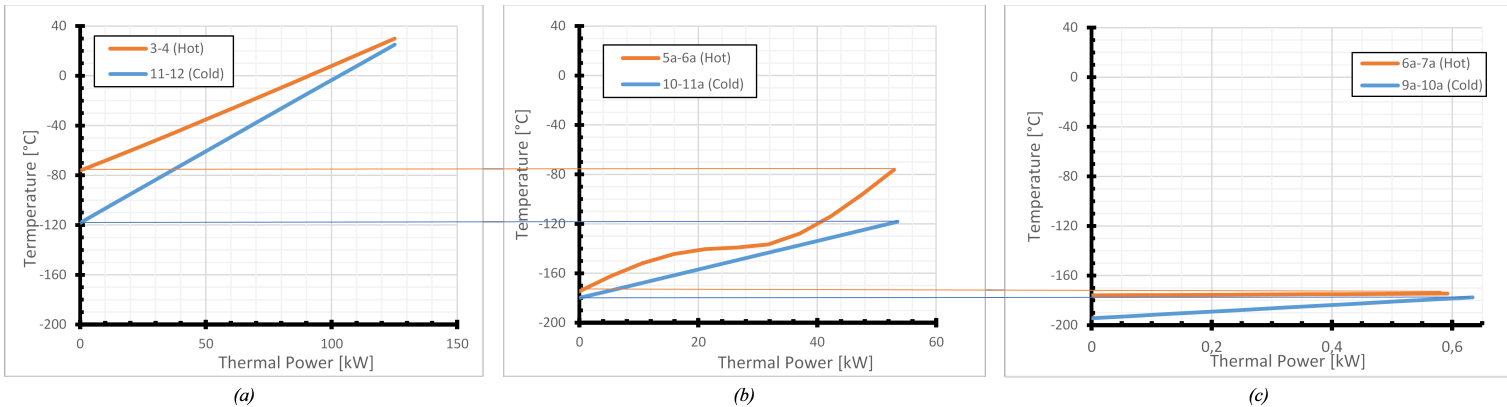

Figure 2.14.: Heat exchangers temperature profiles of the two stage compression Claude cycle

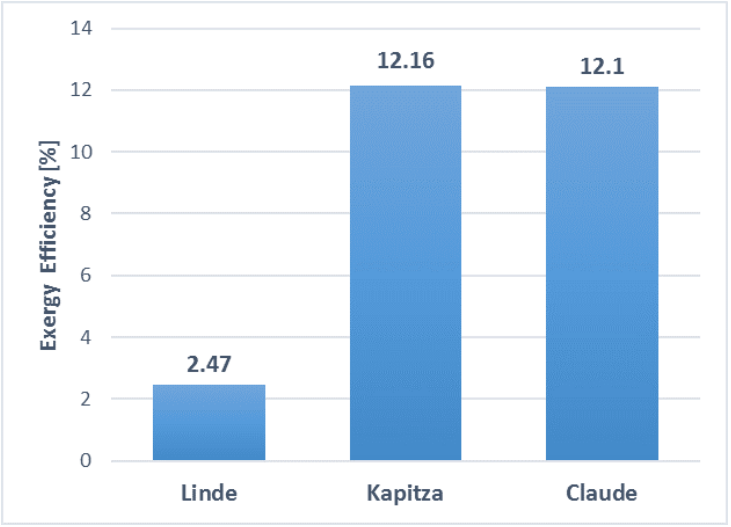

Figure 2.15.: Exergy efficiency of the Linde, Kapitza and Claude liquefaction cycles

Figure 2.15 reports the results of the exergy analysis conducted for each cycle. The calculations were carried out considering the configuration with two stage compression in the conditions of minimum specific consumption reported in 2.3.

Although the value of the exergy efficiency is low for all the three configurations, the Claude and Kapitza cycles give better results than the Linde cycle. The small difference of 0.06% between the Kapitza and Claude cycles can be attributed to the presence of the third heat exchanger (HEX-3) that contributes to an additional exergy loss.

In order to understand the low value of the exergy efficiency, the exergy loss in each component of the Kapitza cycle (with two stage compression operating at 40 bar and 0.2 of recirculation fraction) is reported in Table 2.4.

The 12.16% exergy efficiency reported in Figure 2.15, is due to the relevant exergy loss at the AFTC. Indeed, the heat of compression is rejected directly into the environment without being recovered.

Table 2.4 shows that the exergy loss in the J-T valve and in the two heat exchangers (HEX-1 and HEX-2) is relatively small as compared with the cryoturbine (CT) that results to be the critical component of the liquefaction cycle, apart from the aftercoolers. This high value of exergy loss, can be attributed to the low adiabatic efficiency of 70% set as boundary condition.

Table 2.4.: Exergy loss in the components of the Kapitza cycle with two stage compression operating at 40 bar and 0.2 of recirculation fraction

Components	Exergy loss $[kW]$
C-1	1.916
C-2	1.920
AFTC	235.360
AFTC	251.972
HEX-1	1.62
HEX-2	1.084
CT	8.514
J-T	0.436

2.2. Effect of the phase separator/air liquid tank pressurization

In this section, the effect of phase separator pressurization (and liquid air tank of the LAES) is evaluated for the Kaptiza cycle with two stage compression under various operating conditions. The layout of the Kapitza cycle with pressurized phase separator is almost the same as that already shown in Figure 2.3; the main difference lies in the compression stage, which is shown in some detail in Figure 2.16: the return air from the phase separator (12) mixes with the ambient air which is at lower pressure; hence, it is necessary to add another compressor (C-3), with another aftercooler, to pre-compress the ambient air before mixing.

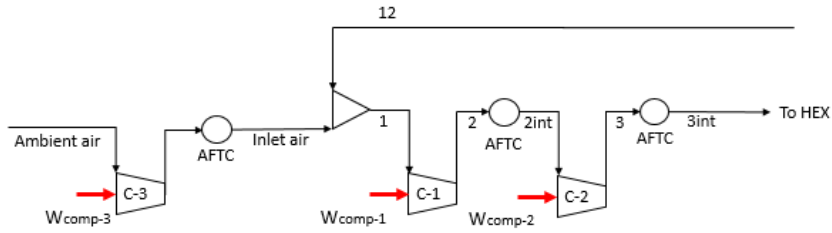

Figure 2.16.: Schematic of the compressor stage of the Kapitza liquefaction cycle with pressurized phase separator

The parametric analysis for the cycle with pressurized phase separator was carried out by varying the total pressure of the cycle, the pressure of the air phase separator and the recirculation fraction. In order to reduce the specific work, the pressure ratios of the compressors (C-1, C-2) are assumed to be the same:

$$\beta_{pre} = \beta_{PS} \tag{2.7}$$

$$\beta_1 = \beta_2 = \sqrt{\frac{\beta_{tot}}{\beta_{pre}}} \tag{2.8}$$

where β_{tot} is the total pressure ratio of the cycle; β_{PS} is the pressure ratio of the compressor (C-3) calculated as the ratio between the pressure of the phase separator and the ambient pressure; β_1 and β_2 are the pressure ratios of the compressors C-1 and C-2 respectively. The boundary conditions for the Kapitza cycle with pressurized phase separator are summarized in Table 2.5 and the results of the simulations are reported in Figure 2.17.

Table 2.5.: Boundary conditions for the simulations of the Kapitza cycle with pressurized phase separator

AFTC outlet temperature	30 °C
AFTC pressure loss	0.0 bar
HEX pressure loss	0.0 bar
Compressor adiabatic Efficiency	85%
Cryoturbine adiabatic Efficiency	70%
Minimum pinch point difference	
HEX-1	5°C ±0.5
HEX-2	3°C ±0.3

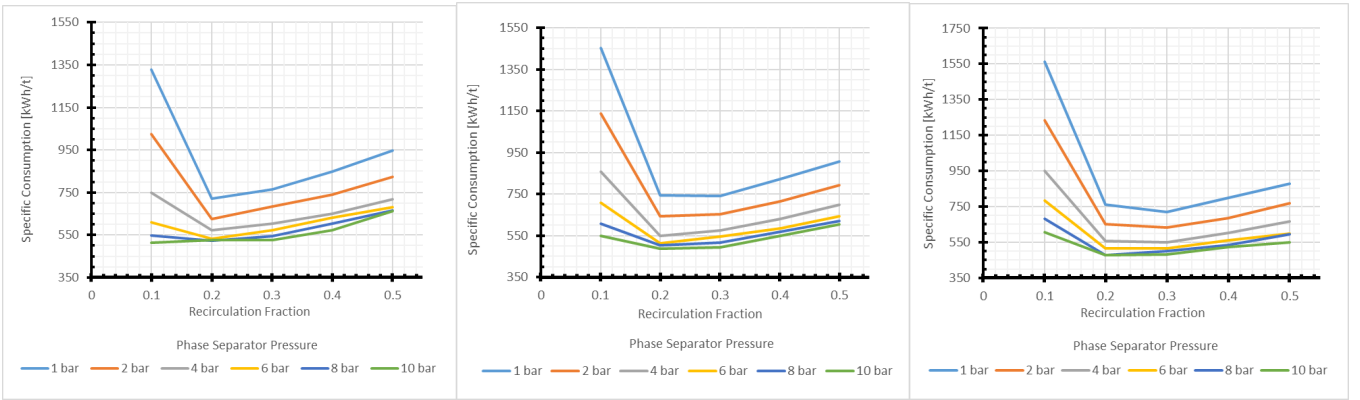

(a) *Kapitza cycle with operating pressure of 40 bar* (b) *Kapitza cycle with operating pressure of 50 bar* (c) *Kapitza cycle with operating pressure of 60 bar*

Figure 2.17.: Specific consumption of Kapitza cycle at different phase separator pressures

Figure 2.17 shows that the phase separator pressurization contributes to an increase of the performance of the cycle and consequently to a reduction in the specific consumption. This reduction also takes into account the additional aftercooler of the third compressor (C-3) which reduces the total work of compression. Figure 2.17 shows that at 40 bar and for phase separator pressure of 4 bar, the specific consumption can be reduced by 21% if compared with the ambient pressure phase separator case (from≈ 700 kWh/t down to ≈ 500 kWh/t). At 6 bar this reduction can go up to 25% with a specific consumption of 532 kWh/t. Figure 2.17b and Figure 2.17c show that by increasing the phase separator pressure, the specific consumption significantly reduces even at lower recirculation fraction: this can be explained with the increase of the heat exchangers performance. The effect of the phase separator pressurization has more benefit for higher values of the operating pressure where it is possible to reduce the consumption under 500 kWh/t, with a minimum of 475 kWh/t for an operating pressure of 50 bar and 10 bar of phase separator pressure.

2.2.1. Discussion and optimal congifuration proposed

The results of the analysis showed in the previous section, reports the values of specific consumption at different operating conditions for different liquefaction cycles. The Linde cycle with one stage compression, holds the highest specific consumption as compared with the other liquefaction cycles. Although the intercooling reduces the specific consumption, the two stage compression Linde cycle efficiency is still low and high operating pressures are required. Considering the Claude and Kapitza cycles with one stage compression, subcritical operating pressures (6 bar and 10 bar) result to be a better option than the supercritical ones (40 bar and 60 bar); indeed, the increase of the compression work for high pressure does not offset the benefit of higher performance of the heat exchangers, thus increasing the specific consumption. The two stage compression improves the performance of both Claude and Kapitza cycles reducing the specific consumption by 20% (from ≈ 900 kWh/t down to ≈ 700 kWh/t) even though supercritical operating pressure is required (40 bar). Table 2.3 shows that the Claude and Kapitza cycles have the lowest specific consumption and similar results in terms of operating range (pressure and recirculation fraction). This similarity is also found in terms of exergy efficiency as reported in Figure 2.15. However, the results shown in Figure 2.14, demonstrate that the third heat exchanger in the Claude cycle can be avoided and that the Kapitza cycle results to be slightly more effective in terms of minimum specific consumption. This led to propose the Kapitza cycle as the best configuration. Finally, the use of pressurized phase separator contributes to further reduce the specific consumption of the Kapitza cycle down to 532 kWh/t. Exergy

Table 2.6.: Optimal operating parameters for the Kapitza cycle

Configuration Proposed	
Cycle	Kapitza
Operating Pressure [bar]	38-45
Recirculation Fraction	0.15-0.3
Storage Pressure [bar] 6-8 bar	
Estimate Specific Consumption [kWh/t]	520-560

analysis shows that the configuration proposed can be furtherly improved by reducing the impact of exergy losses in the aftercooler. Although the results presented in Figure 2.17c show that high operating pressure (50 bar) and high phase separator pressure (10 bar) can reduce specific consumption below 500 kWh/t, a conservative optimal range of operating conditions is proposed in Table 2.6. This range of operating conditions achieves a specific consumption range of 520-560 kWh/t that is an interesting figure for a microgrid scale LAES liquefaction plant.

2.3. Improving liquefaction of microgrid scale LAES through waste heat recovery (WHR) and absorption chiller

In the previous section a preliminary study on the configuration of an air liquefaction cycle for a microgrid LAES application has been conducted. The results shows that a Kapitza liquefaction cycle with pressurized phase separator (and air tank in the case of a full LAES) is the best option amongst the other cycles used for the small scale liquefaction, estimating a specific consumption around 500 kWh/t. The exergy analisys, highlites a low value due to the high amount of exergy loss in the aftercoolers during the two stage of compression. This address to the possibility of further improvements of the liquefaction cycle aimed to the recovery and the reutilizzation of the waste heat of compression. In the literature different solutions are employed in the LAES to recover the waste heat thermal power of compression. The work presented in this section, proposes a novel solution where part of the heat of the aftercooling process, in the compression phase of the liquefaction cycle, is used to drive a single effect water-Lithium Bromide (LiBr) absorption chiller where the chilled water

is then used directly to cool down the air at the inlet of the two main compressors below the ambient temperature. This effect allows to reduce the work of compression and consequently descrease the specific consumption of theliquefaction cycle. Furthermore the heat recovered has benefit on the improoving of the exergy efficiency. In the following paragraph, materials and methods describes the cycle solution proposed and the simulation details including the absorption chiller modelling.

2.3.1. Materials and Methods

Baseline Liquefaction cycle The baseline liquefaction cycle considered in this work is based on the results of the optimal configuration studied in the previous section. Therefore, a Kapiza cycle with pressurized phase separator showed in Figure 2.16 and described in section 2.2 has been taken in account as a baseline case. The operative parameters reported in Table2.7, refers to the oprimal range proposed.

Proposed solution In the proposed solution, the waste heat of the compression is partially recovered to drive a single stage 105.5 kW water-LiBr absorption chiller. The size of the absorption chiller has been chosen based on the results presented in section 2.2.1 thus to maximize the heat recovery of a Kapitza cycle with 40 bar operating pressure and phase separator pressure of 8 bar. Figure 2.18 shows the schematic of the compressor phase of the Kapitza, with the integration of the absorption chiller showed in Figure 2.19 .

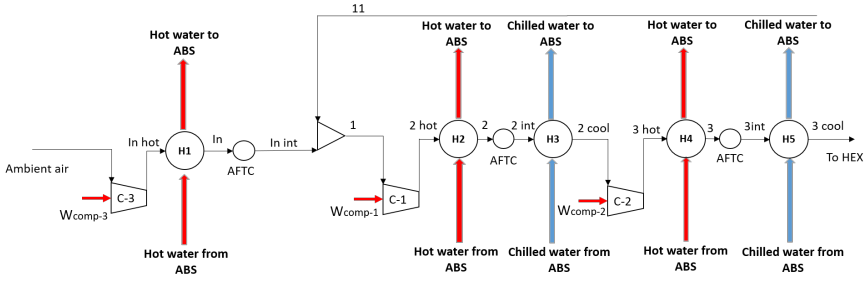

Figure 2.18.: compression phase of the Kapitza cycle with pressurized phase separator with absorption chiller integrated

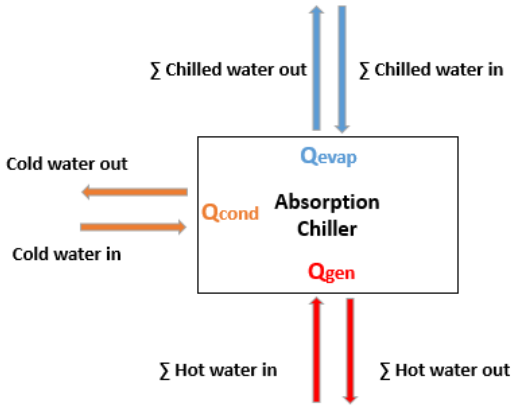

Figure 2.19.: Schematic of the absoprtion chiller

In this case, the waste heat of the compression is recovered by means of three heat exchangers (H1, H2, H4) to rise the temperature of the hot water that drives the absorption chiller. After the heat recovery, the aftercoolers (AFTC) cool down the air at nearly ambient temperature, then the chilled water coming from the absorption chiller is used to further cool down the air below the ambient temperature by means of two heat exchangers (H3 and H5). The first (H3) is used to cool down the air before entering the second compressor (C-2) thus reducing its specific work. The second heat exchanger (H5) is used to cool down the air before entering the high temperature heat exchanger (HEX-1). This results in a lower temperature of the return stream (11) that mixes with the inlet air (In int) thus reducing the specific work of the first compressor (C-1).

Absorption chiller modelling

The single stage water-LiBr absorption chiller is modelled considering the system made up of three main components as shown in Figure2.19:

- Generator (Q_{gen})
- Evaporator (Q_{evap})
- Absorber-Condenser (Q_{cond})

These components are modelled using the characteristic equation method to fit the technical data of a commercial single effect water-LiBr model with a cooling capacity of 105.5 kW. The characteristic equation method is based on the approach of Kühn and Ziegler [45].

In this method, the thermal power (Q_k) of each k-component of the absorption chiller is calculated by a linear correlation with an arbitrary characteristic temperature function defined as:

$$Q_k = s' \cdot \Delta\Delta t' + r \tag{2.9}$$

$$\Delta\Delta t' = T_{gen} - a \cdot T_{ac} + e \cdot T_{evap} \tag{2.10}$$

Where T [°C] represents the average temperature of the medium fluids of the chiller and the four parameters (a, s', r, e) of equation 2.9 and equation 2.10 are the constant parameters estimated by multipole regression from the technical data.

Simulation assumptions

The analysis of the integration of the absorption chiller in the Kapitza cycle with pressurized phase separator has been made with the following assumptions:

1. Cryogenic cycles are considered in steady flow conditions
2. The size of the liquefaction plant is assumed to be a microgrid scale with a liquid air production rate of 0.834 t/h (i.e 10 t/day considering an operating period of 12 h)

Table 2.7 reports the boundary conditions for both the Kapitza cycles with pressurized phase separator with or without the absorption chiller.

In the Kapitza liquefaction cycle with pressurized phase separator, the outlet pressure of the pre-compressor (C-3) is assumed to be the same of the phase separator pressure and the outlet of the cryoturbine. The pressure ratio of the two main compressors (C-1, C-2) is then assumed to be the equal to reduce the specific consumption. In the case of the liquefaction cycle with the absorption chiller integrated, the AFTC temperature is a variable calculated during the simulation to maintain a constant value of the chiller water temperature. The mass flow rate of the hot water and the chiller water is distributed equally along the heat exchangers.

The performances of the liquefaction cycle are calculated and compared by means of the specific consumption defined as:

$$\text{Specific consumption (SC)}[kWh/t] = \frac{W_{net} + W_{abs}}{\text{hourly liquid air produced}} \tag{2.11}$$

In this case, the specific consumption differes from Eq. 2.1 with the add of the term W_{abs} that represents the work input of the absorption chiller.

Table 2.7.: Boundary conditions for the simulation of the Kapitza cycle with pressurized phase separator (PS) with absorption chiller (Abs) and without heat recovery

	Kapitza pressurized PS	Kapitza pressurized PS+ Abs
AFTC outlet temperature	30 °C	-
AFTC pressure loss	0.0 bar	0.0 bar
HEX pressure loss	0.0 bar	0.0 bar
Compressor adiabatic Efficiency	85%	85%
Cryoturbine adiabatic Efficiency	70%	70%
Recirculation Fraction	0.2	0.2
Minimum pinch point temperature difference		
HEX-1	5°C ± 0.5 5°C ± 0.5	
HEX-2	3°C ± 0.3	3°C ± 0.3
Absorber HEX (H1, H2, H3, H4, H5)	-	5°C ± 0.5
Absorption chiller boundary conditions		
Hot Water		
v Mass flow rate [m3/h]	-	26
Max allowed temperature [°C]	-	95
Chilled Water		
Mass flow rate [m3/h]	-	16.5
Inlet temperature [°C]	-	7
Cold Water		
Mass flow rate [m3/h]	-	55
Inlet temperature [°C]	-	31
Absorption chiller input Power [W]	-	310

Exergy Analysis The exergy analysis has been carried out to compare the exergy efficiency η_{ex} that can be calculated for both configuration from eq. 2.6.

2.3.2. Results

Absorption chiller model Figure 2.20 reports the results of the cooling capacity, the heat input and the condenser capacity related with the characteristic temperature difference for a single stage 105.5 kW water-LiBr absorption chiller modelled with the method proposed by Kühn and Ziegler [45]. The results show a good agreement between the technical data and the relation proposed can be considered a valid solution for the absorption chiller model.

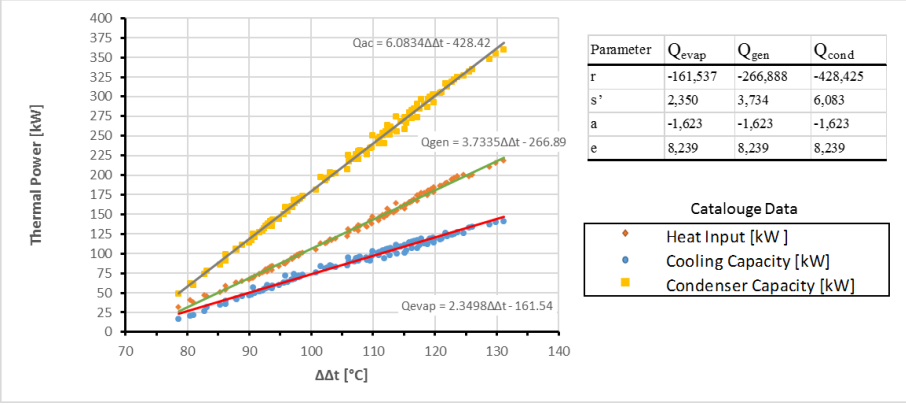

Parameter	Q_{evap}	Q_{gen}	Q_{cond}
r	-161,537	-266,888	-428,425
s'	2,350	3,734	6,083
a	-1,623	-1,623	-1,623
e	8,239	8,239	8,239

Figure 2.20.: Results of the characteristic equation method and the parameters used for equation 2.9 and 2.10 applied for a 105.5 kW single stage water-Li-Br absorption chiller

Kapitza cycle with pressurized phase separator + Absorption chiller Table 2.8 shows the results of the specific consumption of the Kapitza cycle with pressurized phase separator (PS)/liquid air tank with the integration of a 105.5 kW single stage water-LiBr absorption chiller compared to the case without heat recovery.

The results show that for all the operating conditions considered is not possible to integrate the absorption chiller proposed (40-10 bar, 50-6 bar and 60-6 bar)). Therefore, the size of the absorption chiller has to be optimized according to the operating conditions of the liquefaction cycle. However, this temperature can be reduced increasing the mass flow ratio of the hot water but this is limited with the size of the absorption chiller. The integration of a single stage 105.5 kW water-LiBr absorption chiller can reduce of 11% in the case of operating pressure 40 bar and a phase separator pressure of 6 bar (from

Table 2.8.: Results of the simulations for Kapitza cycle with pressurized phase separator (PS) with absorption chiller (Abs) and without heat recovery

		Specifc Consumption [kWh/t]		Exergy Efficiency	[%]		
Pressure	Pressure PS	Kapitza	Kapitza+ Abs	Kapitza	Kapitza + Abs		
40	6	537.03	477.80	11.02	14,91	16.63	11.52
	8	520.53	463.91	10.87	14.94	16.78	12.36
	10	514.89	-	-	14.82	-	-
50	6	508.51	-	-	15.68	-	-
	8	490.72	439.68	10.41	15.85	17.68	11.58
	10	482.20	432.16	10.41	15.83	17.69	11.73
60	6	513.74	-	-	15.52	-	-
	8	487.41	440.32	9.66	16.01	17.68	10.46
	10	471.02	425.52	9.66	16.18	17.95	10.92

537 kWh/t to 478 kWh/t). Indeed, this corresponds to the size for which the absorption chiller has been selected to maximize the heat recovery. The exergy analysis shows that the value of exergy efficiency slightly improves (11.5% in the case of 40 bar and 6 bar of phase separator pressure) but still results in a low value. Indeed, although most of the waste heat of compression is recovered, the absorption chiller introduces a further exergy loss mainly due to the heat rejected through the condenser. The integration of the absorption chiller with the microgrid LAES liquefaction cycle can be considered an interesting solution where the heat is recovered and the specific consumption is reduced in the same working period without the use of further energy storage. However, the introduction of an additional system represents an extra cost that must be considered in a future thermo-economic analysis in order to evaluate the real benefit in terms of efficiency-cost and payback period.

2.4. Discussion and main findings

In the first section of this chapter an optimal configuration for a microgrid scale air liquefier for a microgrid LAES concept is presented. A preliminary analysis is conducted comparing different liquefaction cycles. The cycles are modelled with the software Aspen HYSYS and simulations are conducted by changing the operating conditions such as pressure and recirculation fraction. From the simulation results, the Claude and Kapitza cycles have the lowest specific consumption; with the two stage compression, it is possible to increase the performance by 25%. However, the third low temperature heat exchanger of the Claude cycle results to be inefficient due to the great temperature difference; for this reason, the Kapitza cycle - that does not include the third heat exchanger - results to be a better option. From the analysis of the specific consumption, the heat exchangers result to have the highest impact on the cycle performance. The pressurization of the phase separator/air liquid tank is shown to positively affect the performance, reducing the specific consumption by 21% with a phase separator pressure of 4 bar. Moreover, the combined effect of both pressurized phase separator and increased operating pressure can reduce the specific consumption below 500 kWh/t. However, increasing the operating pressures, the dimensions of the components led to increase the complexity of the cycle and the costs. A conservative final optimal configuration of an air liquefier can be considered a two stage compression Kapitza cycle with an operating pressure in the range of 38-45 bar and a phase separator pressure of 6-8 bar. This range of operating conditions achieves a specific consumption range of 520-560 kWh/t that is an interesting figure for LAES application in microgrids. However, the exergy analysis shows that the thermal power wasted by intercooling is detrimental to exergy efficiency of the cycle and that also the

cryoturbine results to be a critical component. In the second part of this chapter a solution to recover the waste heat of compression is proposed with the aim to decrease the specific consumption and increase the exergy efficiency. In the proposed work a 105.5 kW cooling capacity single-effect absorption chiller using a water-Lithium Bromide solution is integrated with the microgrid scale liquefier studied in the first section. The absorber has been modelled with the characteristic equation method considering the specification of the most common commercial models available in the market resulting in a good match between the technical data and the numerical model. The results of simulation of the absorption chiller integrated with the liquefaction cycle gives a reduction of the specific consumption of around 10% (537 kWh/t to 478 kWh/t) compared with the solution proposed) and an increase of exergy efficiency of around 11.5%.

Chapter 3.

Parametric performance maps for microgrid scale LAES

The previous chapter focuses on the charge section of the microgrid scale LAES with a preliminary study on the optimal configuration of the liquefaction cycle that minimizes the specific consumption. Although the liquefaction cycle has a major impact of the entire LAES performance, the final roundtrip efficiency of the LAES system is also a function of other factors, including the operative parameters discharge section and the quality of waste heat and waste cold recovery. In this chapter, a complete configuration of a microgrid scale LAES system is presented integrating the liquefaction cycle configuration previously studied. The microgrid LAES presented has been modeled by means of the simulation software Aspen HYSYS v8.8 and a sensitivity analysis has been carried out to investigate the effect of the main operative parameter on the system performances in a wide range of operating conditions. The results have been elaborated to carried out novel performance maps that can be particularly useful to assist the preliminary design of a microgrid scale LAES. The main advantage of the maps is the simple and immediate method that can be applied by engineers and researcher to estimate the LAES performance and optimize the design.

In this chapter, section 3.1 describes the LAES charge and discharge section and the simulation assumptions including the main operative parameters used to design the performance maps. The use of the maps is then shown in the two application examples reported in section 3.3.

3.1. Materials and methods

This section describes the modeling of the microgrid scale LAES used to obtain the data to develop the performance maps. The charge and discharge section of the system are described separately and, successively, the simulation assumptions are presented including the operative range of the system used for the parametric analysis.

3.1.1. Microgrid scale LAES charge section

Figure 3.1 shows a schematic of the liquefaction cycle of the charge section used for the numerical simulation of the microgrid scale LAES model. The configuration the same proposed in Chapter 2 based on a Kapitza cycle with a pressurized phase separator with the integration of a High Grade Warm Storage (HGWS) and a High Grade Cold Storage (HGCS). In this case, the waste heat rejected by the aftercoolers after the compressors (C-1, C-2, C-2) is recovered by a heat transfer fluid medium and stored in the High Grade Warm Storage. Another difference with the liquefaction cycle proposed in Chapter 2, concern in the number of cold flows in the heat exchangers (HEX-1 and HEX-2) that in this case can be simplified as only one recuperative heat exchanger (COLD BOX) that integrates the cold flow coming from the High Grade Cold Storage used to assist the liquefaction process. After the two stages of compression, the air flow is divided into two parts: a first fraction is cooled down in the COLD BOX by the flow coming from the HGCS and the cold vapor coming from the phase separator (PS), before being expanded in a Joule Thomson (J-T) valve. The resulting two-phase mixture is then separate in the pressurized phase separator (PS) and the liquid fraction is then stored in an l tank to be used in the discharge section in a later time. The other air flow fraction from

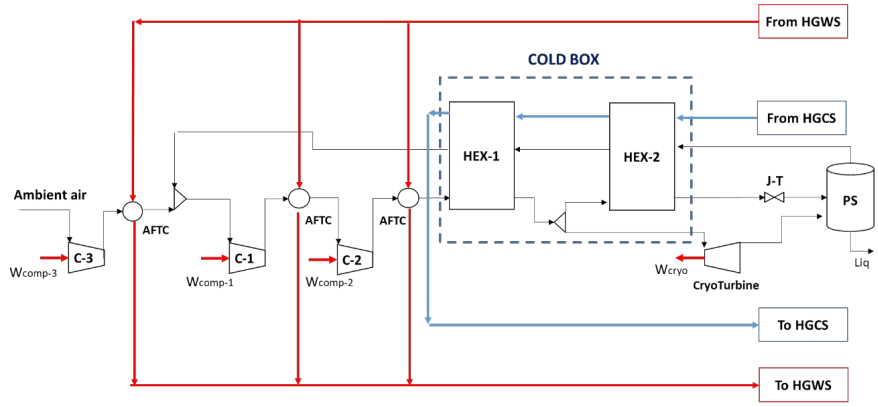

Figure 3.1.: Schematic of LAES charge section

the COLD box is cooled down by isentropic expansion in the CryoTurbine and sent directly to the phase separator (PS).

3.1.2. Microgrid scale LAES discharge section

Figure 3.2 shows the schematic of the discharge section of the microgrid scale LAES. In this stage, the liquid air produced by the liquefaction cycle and stored in the liquid air tank is used in a separate period from the charge phase to produce electric power. The discharge section is made of a cryogenic pump (CryoPump), a liquid air evaporator (HEX-EVAP) connected with the HGCS, 4 stage power turbine section (E-1, E-2, E-3, E-4) with 4 superheaters (SH) integrated with the HGWS. During the discharge, the liquid air stored in the liquid air tank is first pumped ad high pressure by means of the CryoPump before to be regasified in an evaporator (HEX-EVAP) until the air temperature almost reaches the ambient temperature. In this step, the cold thermal energy released by the liquid air, during the evaporation, is recovered with a heat transfer fluid and stored in the HGCS. The cold thermal energy recovered from the liquid air is then used to help the air liquefaction in the charge section described above. The electric power output of the 4 turbines (E-1, E-2, E-3, E-4) in discharge section of the LAES, is boosted by increasing the temperature of the air at the inlet of the expanders by means of the superheaters (SH) using the waste heat of compression recovered in the HGWS.

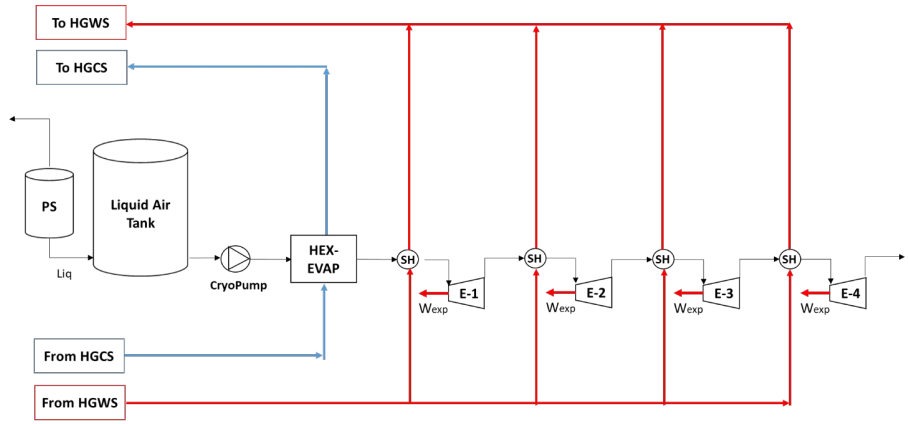

Figure 3.2.: Schematic of LAES discharge section

3.1.3. Simulation Assumptions

The microgrid scale LAES presented above, has been modeled by means of the software tool Aspen HYSYS. The simulations are based on the following assumptions:

1. Cryogenic cycles are considered in steady flow conditions
2. Air and heat transfer fluid properties are calculated by means of Aspen HYSYS
3. Pressure losses in the components other than the expanders are neglected;
4. Auxiliary electrical losses are not included in the model.
5. The liquid air production rate is assumed around 1 t/h (microgrid scale LAES)

The novel performance maps presented in this work are elaborated from the parametric analysis based on the main operative parameters and the main key performance indicators reported in Table 3.1.

In the Table3.1 is worth to notice that the thermal energy storages (HGCS and HGWS) used to recover the hot and cold waste heat thermal energy of the LAES, are considered in terms of their performance (eta_{HGCS} and eta_{HGWS}) where $Q_{u,HGWS}[kW_{th}]$ and $Q_{u,HGWS}$ $[kW_{th}]$ are the waste cold and waste heat power effectively utilized over the heat thermal power totally available from the waste heat recovered from HGCS and HGWS ($Q_{tot,HGCS}[kW_{th}]$, $Q_{tot,HGWS}[kW_{th}]$). The specific electric power output of the LAES is calculated from the net electric power output $P_{net,discharge}$ that is the sum of the power of each expander (n_e) at the net of the power consumed by the CryoPump P_{cryoP}. The calculation of the specific consumption (SC) refers to eq 2.2.

Table 3.2 shows the range of simulation of the main performance parameters that serve as a variable input for the LAES model while the outputs are represented by the key performance parameters. The working fluids selected to transport waste heat and cold energy recovered in the LAES system are *dowtherm Q* and *air*, respectively. Table 3.2 shows the range of simulation of the main performance parameters. The compressors and turbines isentropic efficiencies are considered as constant. In this case, the phase separator/ liquid air tank pressure (8 *bar*) is fixed at the optimal value evaluated in the previous chapter. In the parametric analysis, different level of HGSC and HGSW are first considered at various discharge pressures. Then the charge section has been investigated varying the charge pressure and the recirculation fraction that minimize the specific consumption. The results of all the simulation

Table 3.1.: Operative parameters and key performance indicators used for the parametric analysis

Parameter		Description
p_{ch}	Charge pressure $[bar]$	Pressure of the liquefaction cycle
p_d	Discharge pressure $[bar]$	Pressure of Cryopump of the LAES discharge section
x_{rf}	Liquefaction cycle Recirculation fraction	Ratio of the mass flow elaborated by the J-T valve and the mass flow entering the COLD BOX
SP	Specific electric power output of the LAES $[kWe/kg]$	$\text{SP} = \frac{P_{net,discharge}}{\text{hourly liquid air produced}} = \frac{\sum^{n_e} P_{exp} - P_{cryoP}}{\text{hourly liquid air produced}}$
SC	LAES Specific consumption $[kWhe/kg]$	$\text{SC} = \frac{W_{net,charge}}{\text{hourly liquid air produced}} = \frac{\sum^{n_c} W_{comp} - W_{cryoT}}{\text{hourly liquid air produced}}$
TIT	Discharge Turbine Inlet Temperature	Temperature of the air after the superheaters (SH)
$etaHGCS$	Efficiencies of high grade cold thermal energy storage [%]	$\eta_{HGCS} = \frac{Q_{u,HGCS}}{Q_{tot,HGCS}}$
$etaHGWS$	Efficiencies of high grade warm thermal energy storage [%]	$\eta_{HGWS} = \frac{Q_{u,HGWS}}{Q_{tot,HGWS}}$
η_{RT}	LAES Round trip efficiency [%]	$\eta_{RT} = \frac{P_{net,discharge}}{P_{net,charge}}$

Table 3.2.: Value and range of the operative parameters used for the LAES parametric analysis

Parameters	Value-Range
Air inlet temperature [°C]	25
Charge pressure [bar]	40-90
Recirculation fraction	0.10-0.55
CryoPump discharge pressure [bar]	60-160
$eta_{HGCS,HGWS}$ [%]	12.5-100
Phase separator (PS) / Air liquid tank pressure [bar]	8
AFTC outlet temperature [°C]	30
HEX-1 pinch point ΔT [°C]	5
HEX-2 pinch point ΔT [°C]	3
HEX-EVAP pinch point ΔT [°C]	5
Hot end temperature approach SH [°C]	10
Compressor adiabatic Efficiency (Charge) [%]	85
CryoPump adiabatic Efficiency [%]	80
CryoTurbine adiabatic Efficiency [%]	70
Expander adiabatic Efficiency (Discharge) [%]	80

combinations are the base of the performance maps that have been printed out by MATLAB software using the Curve Fitting Toolbox App [46] (Figure 3.3). The curve fitting capability integrated into the program allows obtaining an easy view of the data plots by means of a linear interpolation.

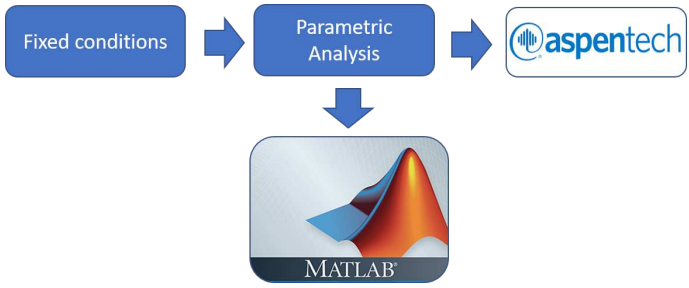

Figure 3.3.: methodology used for the performance maps

3.2. Results and discussion

This section reports the results of the simulations of the LAES plotted in the form of performance maps, considering the simulation assumptions presented in the previous section. The four different maps are based on the operative parameters and the key performance indicators reported in Table 3.1. With the maps, some analytic relations related to the thermodynamic analysis of the LAES are presented as an alternative to calculating the LAES performance.

3.2.1. Effect of charge pressure and waste cold power on the Specific consumption

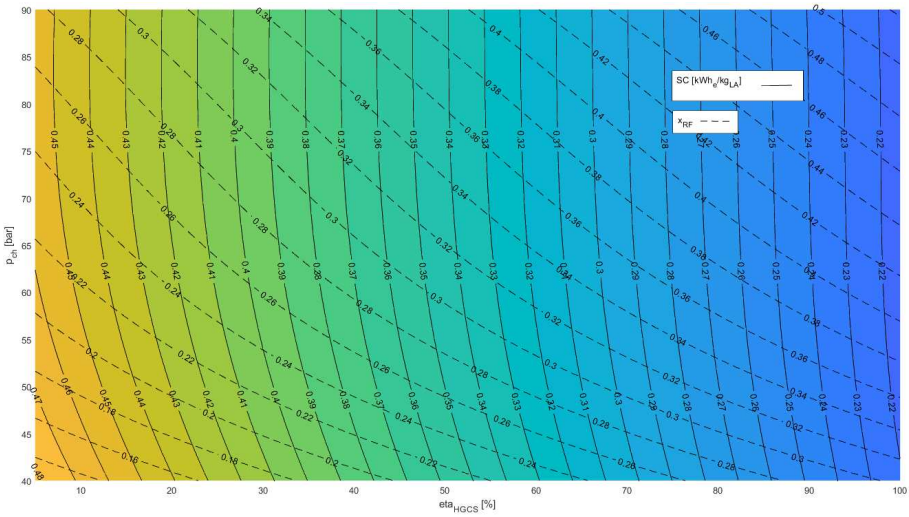

Figure 3.4.: Effect of charge pressure and waste cold recovery efficiency on specific consumption for different optimum values of recirculation fraction

Figure 3.4 reports the first perfromance map related to the charge section of the LAES system and represented by the operative parameters of the liquefaction cycle. This map, allows to estimate the specific consumption SC $[kWh_e/kg_{LA}]$ of the microgrid scale LAES that correspond to the value obtained with the optimal recirculation fraction x_{rf} reported in the map. The two main operative parameters considered in this chart are the charging pressure of the LAES $p_{ch}[bar]$ and the efficiency of the High Grade Cold Storage $eta_{HGCS}[\%]$. As showed in Figure 3.1, the High Grade Cold Storage provides, by means of a heat transfer fuild, the cold flow that cools down the high pressure air entering the COLD BOX affetting the performance of the liquefaction cycle. Indeed, the map in Figure 3.4 clearly shows that the specific consumption can

be highly reduced whit an high efficiency of waste cold recovery and HGCS. Furthermore, the maps show that for high value of the HGCS efficiency, the charge pressure has not a relevant effect on the specific consumption. Therefore, the design cold storage is crucial to minimize the specific consumption and optimize the performance of the entire system. Considering the equation reported in Table 3.1, the specific consumption (SC) can be analitically calculated from the work of each compressor and the work of expansion of the CryoTurbine that can be written as:

$$W_{comp,tot} = \sum^{n_c} W_{comp} = \sum^{n_c} m_{comp,in} c_{p,ave} T_{comp,in} \left(\theta_{comp}^{\frac{1}{\eta_{poly,comp}}} - 1\right) \tag{3.1}$$

$$\theta_{compr} = (\beta_{compr})^{(\frac{\gamma-1}{\gamma})} \tag{3.2}$$

$$\gamma = \frac{c_p}{c_v} \tag{3.3}$$

$$\eta_{iso} = \frac{\theta - 1}{\theta^{1/\eta_{poly}} - 1} \tag{3.4}$$

$$W_{cryoT} = m_{cryoT,in}(h_{cryoT,in} - h_{cryoT,out}) \tag{3.5}$$

In eq.3.1, $\eta_{poly,comp}$ refers to the polytropic efficiency of the compressor, that can be related to the isentropic efficiency by eq. 3.4. The value of θ can be calculated with eq. 3.2 from the compression ratio β and the heat capacity ratio γ defined from eq. 3.3 as the ratio between the specific heat capacity at constant pressure c_p and the specific heat capacity at constant volume c_v. In eq. 3.5, $h_{cryoT,in}$ and $h_{cryoT,out}$ refers to the value of the enthalpy at the inlet and at the outlet of the cryoturbine respectively. The mass of air elaborated from each compressor $m_{comp,in}$ $[kg]$ and the cryoturbine $m_{cryoT,in}$ $[kg]$ can be calculated from the mass balance on the charge side of the LAES as:

$$m_{C-3} = \text{hourly liquid air produced} \tag{3.6}$$

$$m_{C-1} = m_{C-2} = \text{hourly liquid air produced} \cdot \text{Liquid Yield} \tag{3.7}$$

$$m_{cryoT,in} = m_{C-1} \cdot (1 - x_{rf}) \tag{3.8}$$

Where y represents the liquid yield that can be calculated from eq.2.3 as a funcion of the avaliable high grade waste cold $Q_{tot,HGWS}$ and the efficiency of the HGCS η_{HGCS} from the energy balance of Figure 3.5:

$$\text{Liquid Yield} = \frac{h_{CB,out} - h_{CB,in} + \left(\frac{Q_{tot,HGCS}}{\dot{m}_{LA}} eta_{HGCS}\right)}{h_{CB,out} - h_{LA}} \tag{3.9}$$

where $h_{CB,in}$ and $h_{CB,out}$ refeers to the enthalpy at of the flow at the inlet

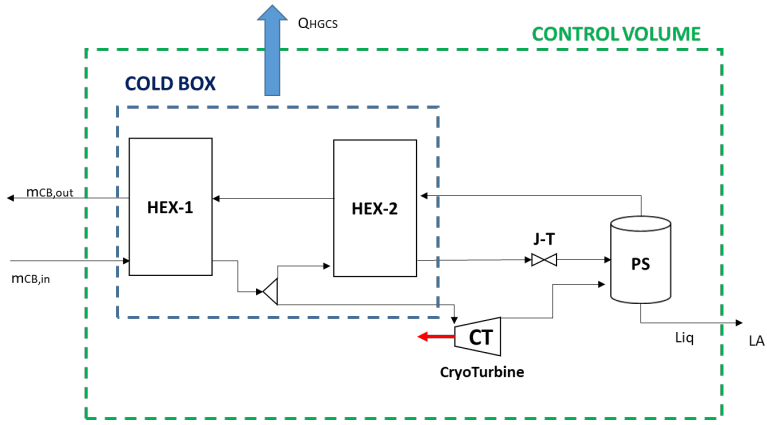

Figure 3.5.: Energy balance over the control volume

and the outlet of the COLD BOX respectively and $\cdot m_{LA}$ is the mass flow rate of the liquid air. The total waste cold thermal power available can be calulcated considering the specific work of the cryopump w_{cryoP} as:

$$Q_{tot,HGCS} = (h_{EVAP,out} - h_{cryoP,in} + w_{cryoP}) \cdot (m_{LA}) \tag{3.10}$$

$$w_{cryoP} = \frac{(p_{out} - p_{in}) \cdot v_{in}}{\eta_{iso,cryoP}} \tag{3.11}$$

where in the eq. 3.10, $h_{EVAP,out}$ and $h_{cryoP,in}$ refers to the enthalpy of the air at the outlet of the evaporator (HEX-EVAP) and of the liquid air at the inlet of the CryoPump. The terms p_{in} and p_{out} in eq. 3.11 refers to the inlet to the inlet and the outlet pressure CryoPump, while v_{in} refers to the specific volume of the liquid air at phase separator pressure and $\eta_{iso,cryoP}$ refers to the adiabatic efficiency of the CryoPump.

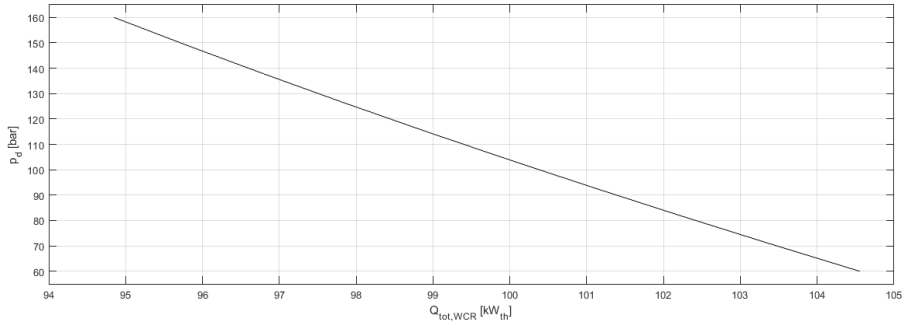

Figure 3.6.: $Q_{tot,HGCS}$ as a function of discharge pressure

Figure 3.6 shows the total waste cold thermal power available as a function of the discharge pressure. From the results is possible to note that the variation of the $Q_{tot,HGCS}$ can be negligible compared to the wide range of discharge pressure (60-160 bar), therefore the total waste cold thermal power can be assumed as constant ($\approx$ 100 kW_{th})

3.2.2. Charge pressure-TIT relation

The second map showed in Figure 3.7 reports the TIT [°C] of the discharge cycle according to the charging pressure $p_{ch}[bar]$ and the efficiency of the HGWS $eta_{HGCS}[\%]$.

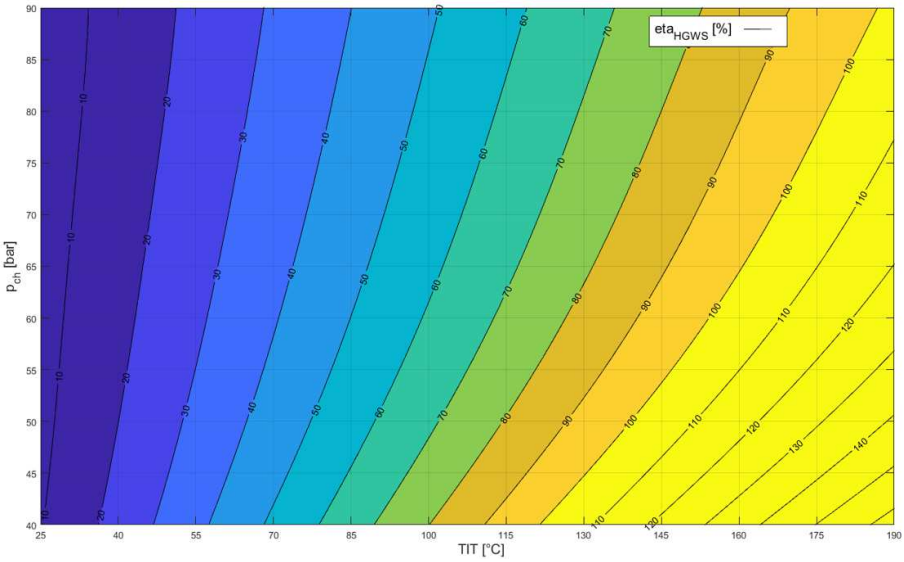

Figure 3.7.: Effect of charge pressure and waste heat recovery on the turbine inlet temperature

The map clearly shows that increasing the pressure of the liquefaction cycle (p_{ch}) is it possible to obtain higher TIT with a lower HGWS efficiency. The TIT can be calculated as a function of thermal power available from the HGWS, assuming that the heat transfer fluid HTF (Dowtherm Q) entering the HGCS is at ambient temperature as:

$$\mathrm{TIT} = T_{ambient} + \frac{Q_{tot,HGWS} \cdot eta_{HGWS}}{\dot{m}_{HTF} \cdot cp_{HTF}} - \Delta T_{SH} \tag{3.12}$$

In the eq.3.12 is assumed that t the heat transfer fluid enetering the HGCS is at ambient temperature. The total waste heat avaliable $Q_{tot,HGWS}$ can be calculated considering the waste heat power available for each compressor in

the charge section as:

$$\begin{aligned} Q_{tot,HGWS} &= \sum^{n_c} Q_{comp,HGWS} \\ &= \sum^{n_c} \dot{m}_{comp,in} \cdot cp_{ave,air} \cdot \left(\left(T_{comp,in} \cdot \theta_{comp}^{\frac{1}{\eta_{poly}}} \right) - T_{AFTC} \right) \end{aligned} \tag{3.13}$$

3.2.3. Discharge pressure-TIT relation

The effect of the TIT $[°C]$ on the specific electric power output (SP) $[kWh_e/kg_{LA}]$ produced from the discharge side of the LAES is showed in Figure 3.8 for different discharge pressures of the cryogenic pump.

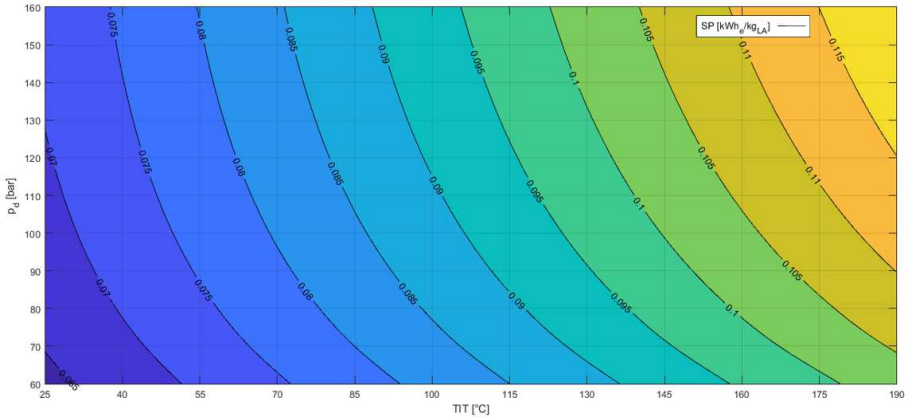

Figure 3.8.: Effect of discharge pressure and Turbine Inlet Temperature on the specific electric power output

In this third map is possible to obtain, for a fixed amount of liquid air (1 ton/hour), a higher electric power from the discharge side with high TIT and high discharge pressures. This effect could be described using the following equation from the theory of gas turbines technology:

$$SP = \frac{P_{net,d}}{m_{LA}} = n_e \cdot cp_{ave,air} \cdot TIT \cdot \left(1 - \frac{1}{\theta_{exp}^{\eta_{poly,exp}}} \right) \tag{3.14}$$

Where $\eta_{poly,exp}$ reffers to the polytropic efficiency of the expanders that can be calculated from the isentropic efficiency using eq. 3.4.

The value of θ_{exp} can be calculated from eq. 3.2 and including the expansion ratio β_{exp} that can be written as:

$$\beta_e = \left(\frac{p_d}{p_{ambient}}\right)^{1/n_e} \tag{3.15}$$

3.2.4. Round trip efficiency evaluation

The last map presented in Figure 3.9 includes the combination of the key performance indicators parameters presented above. In particular, this map can be used to evaluate the round trip efficiency of the system related to the Specific Consumption (SC) and the specific electric power output (SP) that can be defined with the use of the previous maps. Figure 3.9 shows that the relation between the parameters is linear and can e expressed as follow:

$$\eta_{RT} = \frac{SP}{SC} \tag{3.16}$$

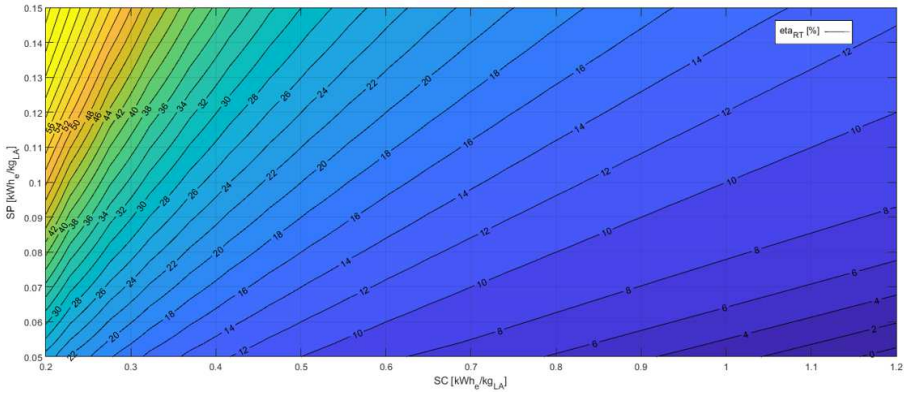

Figure 3.9.: Round trip efficiency as a function of net Electric power output and liquefaction specific consumption

3.3. Use of the performance maps

This section reports two practical examples to show the use and the applications of the four performance maps proposed in this work.

3.3.1. Example A: High-pressure liquefaction system and medium efficiency of HGCS and HGWS

This example has been done to evaluate the performance a LAES system with a high-pressure liquefaction cycle (80 bar) a medium high pressure of discharge (100 bar) and a medium efficiency of waste heat and cold thermal energy recovery (50%).

Step 1: Evaluation of the specific consumption The first step is to use the map reported in Figure 3.4 to evaluate the specific consumption of the LAES liquefaction cycle and the optimal recirculation fraction to be adopted. From the map is possible to cross two straight lines from the points corresponding the charge pressure of 80 bar and an HGCS of 50%, and find a specific consumption of around 0.34 $[kWh_e/kg_{LA}]$ for an optimal recirculation fraction of 0.36.

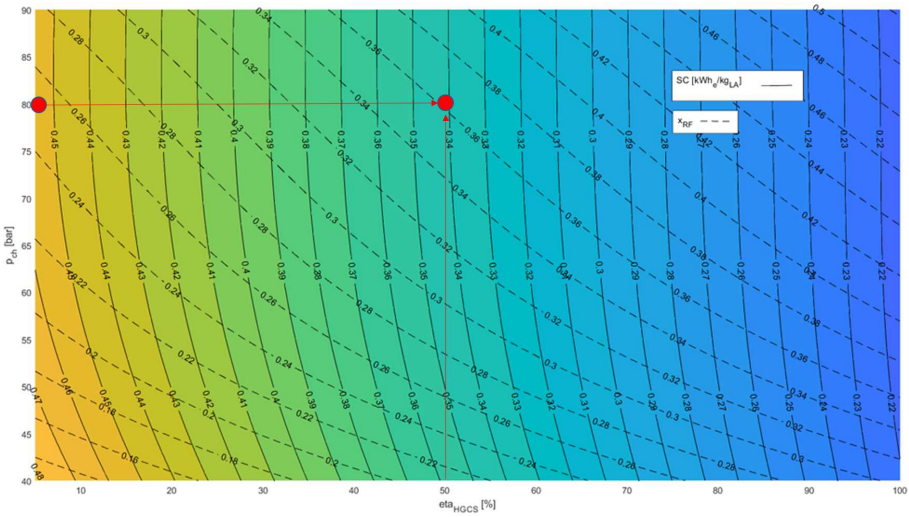

Figure 3.10.: Example A: evaluation of the specific consumption

Step 2: Evaluation of the TIT The charge pressure of the liquefaction cycle of the LAES and the Efficiency of HGWS defines the inlet turbine temperature in the discharge section. This allows in the next step to find the net electric power output of the LAES. In this example is possible to find from the second map a TIT of around 98 °C that is showed in Figure3.11.

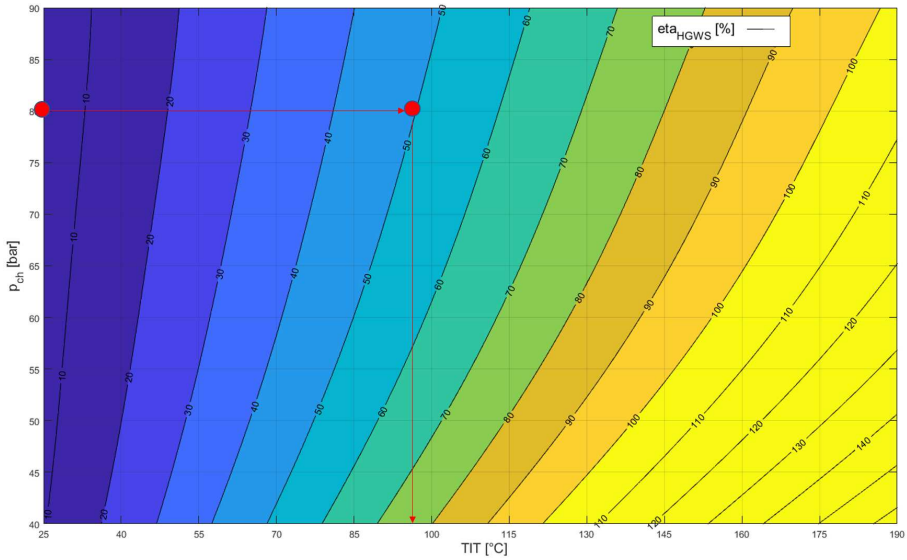

Figure 3.11.: Example A: evaluation of the TIT

Step 3: Estimation of the specific electric power The third map presented and showed in Figure3.8 allows finding the specific electric power output of the LAES according to the TIT founded to the previous step and the pressure of discharge. Drawing two straight line as showed in Figure3.12 is possible to find a specific electric power output of 0.087 $[kWh_e/kg_{LA}]$.

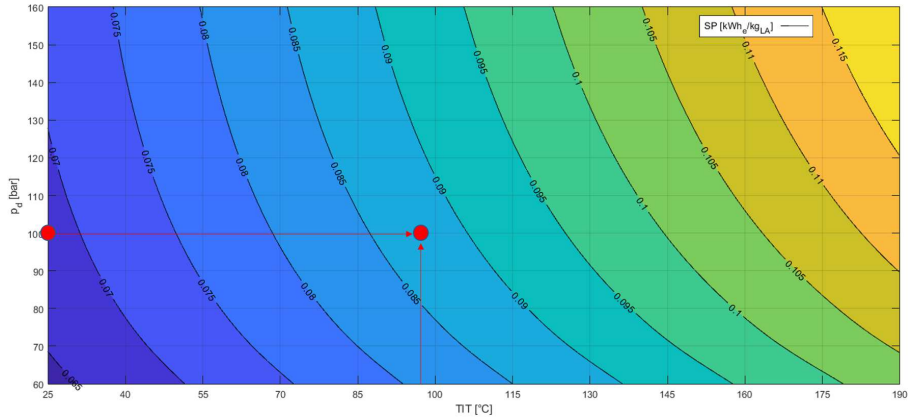

Figure 3.12.: Example A: of the specific electric power

Step 4: Calculation of the round trip efficiency The last step is to define, from the previous parameters obtained from the other maps, the round trip efficiency of the entire LAES system. In this example Figure 3.13 reports for a specific electric power output of 0.087 $[kWh_e/kg_{LA}]$ and a specific consumption of around 0.34 $[kWh/kg_{LA}]$ a roundtrip efficiency of around 25%

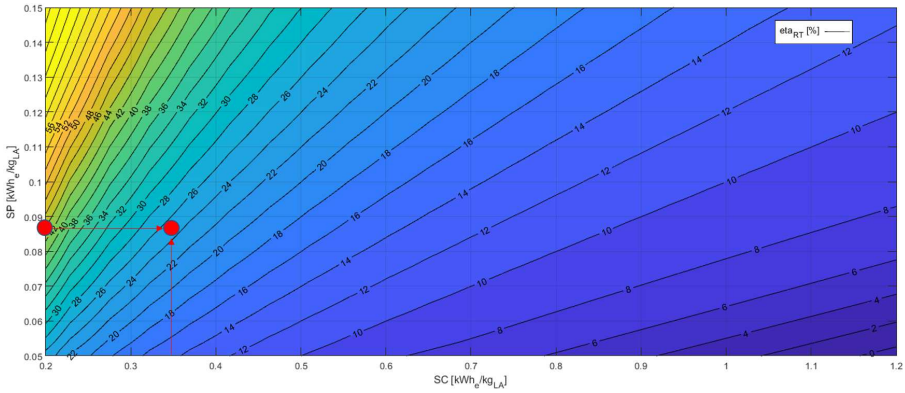

Figure 3.13.: Example A: Calculation of the round trip efficiency

Comments The final roundtrip efficiency of 25% in the case of example A results half of the value of a large-scale LAES plant (50-60%). In this case, the performance map proposed can help the designer to evaluate which operative parameters to take into account in order to improve the performance of the system. Considering the last map (Figure 3.9) the roundtrip efficiency of the LAES could be improved either decreasing the SC and/or increasing the net electric power output of the system. From the first map, the main parameter that allows improving the specific consumption is the efficiency of the waste heat cold recycle (HGCS), while net electric power output can be increased acting of different parameters, mainly the TIT and the discharge pressure of the LAES. In this case, the designer has to choose the operative parameters which are the most convenient to operate based on the economic evaluation (better the efficiency of the components, higher the cost) and technological limits such as the dimension of the plant and availability of the components.

3.3.2. Example B: Low-pressure liquefaction system and medium-high efficiency of HGCS and HGWS

This example considers LAES system with a medium pressure liquefaction cycle (60 bar) a medium high pressure of discharge (100 bar) and a medium efficiency of waste heat and cold thermal energy recovery (80%). The procedure is the same already shown in the previous example (case A).

The first map of Figure3.14 shows that with an higher efficiency of the HGCS the specific consumption has decreased to 0.275 $[kWh/kg_{LA}]$. An interesting result is showed in the second map where even if in this case a low charging pressure is considered, the TIT is increased compared to the previous case, that results in a higher net electric power output as shown in the third map. A decrease of the specific consumption and an increase of the electric power output concerns in a higher roundtrip efficiency of 36% reported in Figure3.14 . In this case, the designer has to choose the operative parameters which are the most convenient to operate based on the economic evaluation (better the efficiency of the components, higher the cost) and technical limits such as the dimension of the plant and availability of the components selected.

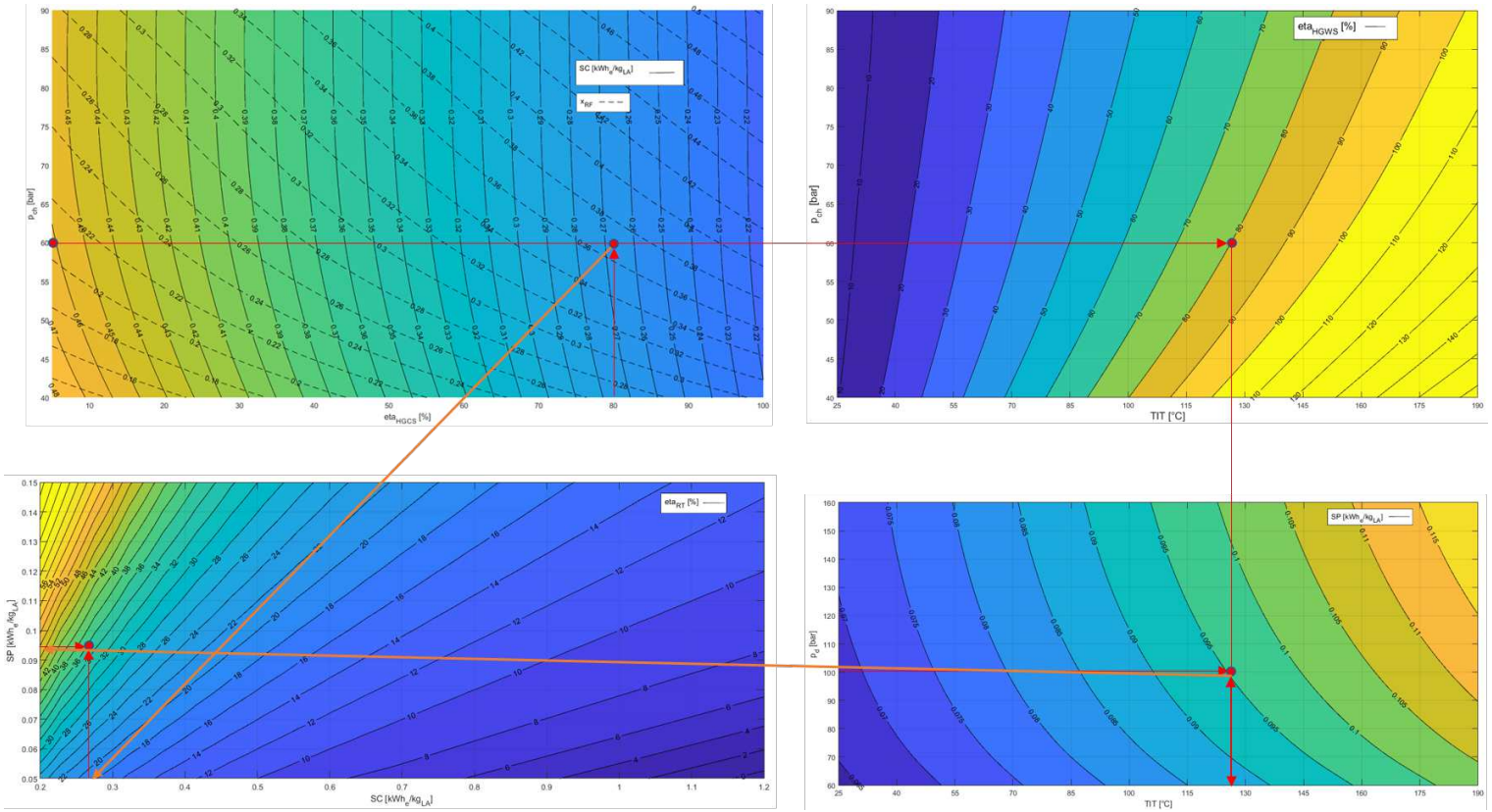

Figure 3.14.: Example B: Calculation of the key performance indicators from the main operative parameters

3.4. Discussion and main Findings

In this chapter, a full configuration of the microgrid scale LAES has been presented. The charge section of the system considers the configuration presented in chapter 2. The steady-state LAES model presented includes the discharge section and the waste heat and cold thermal energy recovery. A parametric analysis has been carried out by simulations using a LAES model developed with Aspen HYSYS v.8.8. The results are obtained varying the main operative parameters originated a large number of that that has been elaborated to carried out four main microgrid scale LAES performance maps. This innovative approach could be a useful tool to assist the design of a microgrid scale LAES. The main advantage of the maps is the simple graphical approach that allows the designer to have a first estimation of the LAES performance avoiding the use of simulation software. At the end of this chapter two application example of the performance, maps have been presented. The analysis of the first map shows that efficiency HGCS has the highest impact on the specific consumption over the charge pressures. Indeed an efficient HGCS allows designing a system that can operate at lower pressures without affecting the specific consumption. The same effect can be noticed in the discharge section of the LAES represented in the second performance map, where with higher HGWS is possible to reach higher TIT with lower HGWS efficiency. Therefore, the performance maps highlight the importance of a proper design of the waste heat recovery system that results crucial for the system efficiency. The pressure of discharge can boost the specific power output of the system, with a negligible impact on the waste cold power available. The performance of the system can be evaluated in the last fourth performance map. Following the steps reported in the examples, the graphical approach results in an immediate way to estimate the microgrid scale LAES performance and evaluate the impact of the main operative parameters during the system design. The methodology can be extended scaled up for the large-scale system and be applied as a systematic tool for different LAES configurations (full electric and cogenerative/trigenerative).

Chapter 4.

Thermal characterization of Phase Change Materials for LAES High Grade Cold Storage: Introduction, Material and Methods

4.1. Introduction and background

The performance maps presented in chapter 3 highlight the importance of integrating into the microgrid scale LAES the recovery of the waste heat and waste cold thermal energy. In particular, the reuse of the cold energy released by the liquid air before the expansion in the discharge cycle allows to improve the performance of the charge side of the LAES decreasing the specific consumption of the liquefaction cycle and increase the overall roundtrip efficiency of the system. The waste cold thermal energy recovery system, showed in Figure 4.1, is made up with the following components:

- Heat Exchanger - integrated with the liquid air evaporator
- Heat Transfer Fluid (HTF)
- High Grade Cold Thermal Energy Storage (HGCS)

The design of each component of the waste cold recovery system has its own role to contribute to the final quality and efficiency of the entire system. Considering the study conducted of Morgan et al.[47] on the Highview power pilot plant, the value of 8% round-trip efficiency of the LAES is attributed to the low quality of waste cold recovery, where only the 51% of the waste cold available is reused to decrease the specific consumption of the liquefaction cycle. Amongst all the components, the High Grade Cold Storage (HGCS) is the most critical part to increase the efficiency of a LAES system. A numerical study conducted by Sciacovelli et al.[48] shows the performance of standalone LAES

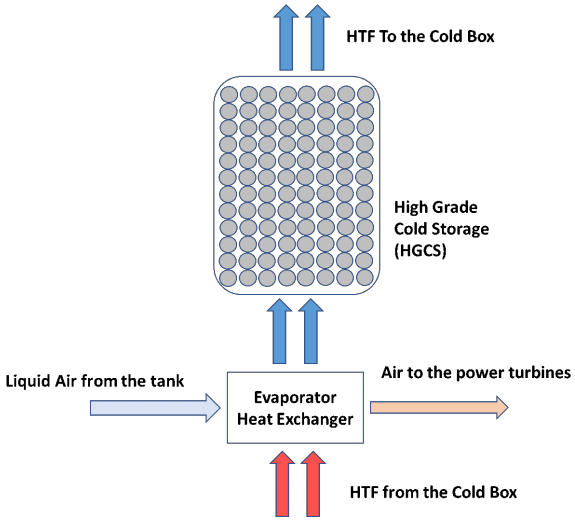

Figure 4.1.: Schematic of the components of LAES high grade cold recycle

through a dynamic modeling of the HGCS based on a packed bed with quartzite rocks as the storage material. Although the nominal round trip efficiency of the LAES system is around 50%, the dynamic effect of the HGCS allows a degradation of the thermal front in the tank that causes an increase of the storage temperature decreasing the LAES round-trip efficiency of 25%. Indeed, also the study conducted by Peng et al.[49] on the effect of waste heat and waste cold recovery on a LAES, affirm that the temperature of the cold flow recycled, should be the lowest as possible in order to obtain the best performances of the system. Therefore, a proper design of the HGCS represents the main challenge obtain a high efficiency of the system and maintain the performance at the optimal value.

4.1.1. HGCS and Cold Thermal Energy Storage

High Grade Cold Storage (HGCS) can be considered as a subcategory of Cold Thermal Energy Storage (CTES). In those systems, the cold thermal energy is stored in a storage medium to be used in a later time. The storage process involves three main stages:

- Charge process, where the thermal energy of a medium is transferred in the storage material;
- Storage process where the thermal energy is conserved;
- Discharge process where the thermal energy is released;

CTES has its own role to improve the efficiency of different energy systems that involve cold thermal energy. One of the most common applications of the CTES is the peak load shifting of cold energy, mainly applied to air-conditioning and refrigeration systems where the night-time cold thermal energy produced can be stored and used to cover the cooling peak demand during the daytime [50]. In this case, the integration of a CTES with an air conditioning system reduces the cooling capacity and the size of the refrigeration plant, allowing the system to operate at the maximum efficiency and decreases the operational cost. Those applications usually involve CTES based on chilled water, ice or eutectic salt with a temperature above 0°C. However, CTES can be used to store high grade cold thermal energy and applied to a system that requires a thermal energy vector with sub-zero temperature. In this case, CTES can be referred to High Grade Cold Storage (HGCS). Li et al. [51] proposes a list of CTES for sub-zero applications based on the temperature range showed in Figure4.2.

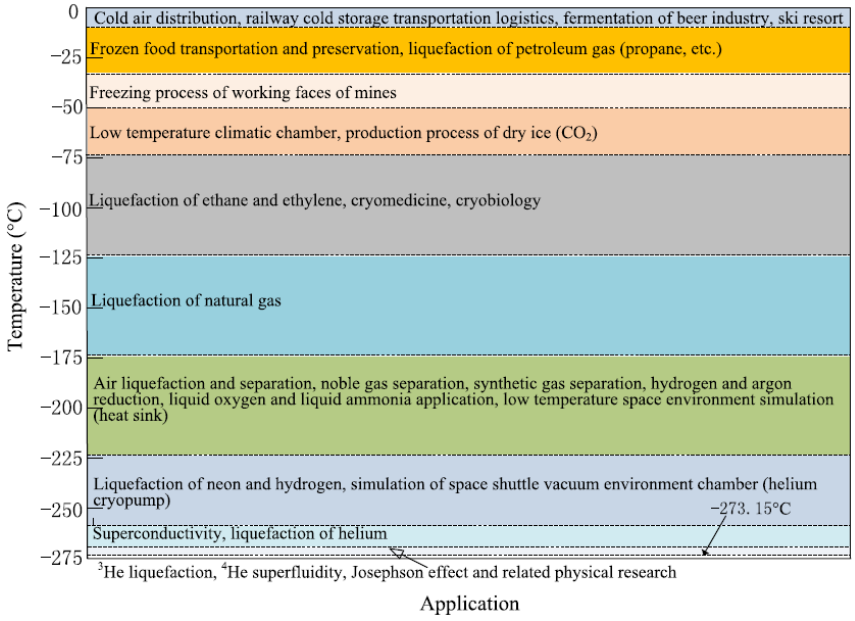

Figure 4.2.: Figure CTES for sub-zero applications

Based on the storage mechanism, CTES be classified into three main categories:

- Sensible Heat Energy Storage
- Latent Heat Thermal Energy storage
- Thermochemical Energy storage

In the sensible heat storage, the temperature of the storage material is changing during the charging/discharging process and the thermal energy stored is based on the specific heat capacity of the storage material itself. In this case, the heat stored can be represented as:

$$E = m \cdot \int_{T_1}^{T_2} c_p \cdot dT \tag{4.1}$$

where E is the energy stored (kJ), m and c_p are respectively is the mass of storage material $[kg]$ and the specific heat $[kJ/kgK]$. T_1 T_2 are the initial and the final temperatures $[K]$ of the storage material. Sensible heat can use both a solid media storage or liquid media storage[50].

Latent heat thermal energy storage the temperature of the storage material remains nearly at a constant value while the phase of the material is changing. Indeed, those systems rely on the use of Phase change materials (PCM). The phase change can be either solid-liquid phase or liquid-vapor phase. However, the large difference of volume change between liquid and vapor phase generates mechanical stress on the PCM results in many difficulties, therefore the most used latent heat energy storages involve the solid-liquid phase change of the material. Compared to the sensible heat energy storage, is not possible to relate the energy stored only with the specific heat of the material (since it refers to a single phase) and the temperature change. Indeed, the thermal energy stored includes the enthalpy difference between the solid and the liquid phase:

$$E = m\Big(\cdot \int_{T_1}^{T_{PC}} c_{p,solid} \cdot dT + \Delta H_{ls} + \int_{T_{PC}}^{T_2} c_{p,liquid}\Big) \tag{4.2}$$

The temperature where the phase change takes place is a characteristic of the material and is called phase change temperature T_{PC} and the enthalpy difference $\Delta H_{ls}[kJ/kg]$ related to the phase change is a characteristic called latent heat of fusion L.

The last category is the Thermo-chemical energy storage. In this case, a chemical reaction is involved in the charging/storage stage and thermal energy is then released in the discharge phase by a reverse reaction. At low temperature Thermochemical energy storage are presented as *sorption cold storage*, where the most common technologies are: absorption and adsorption. Although the thermochemical materials are characterized by a high energy density and almost zero heat losses during the storage process [52], the major disadvantages are represented by the low thermal conductivity and the poor recyclability. Furthermore, they result difficult to apply to sub-zero applications and the actual high cost strongly limits the applicability of this technologies. Therefore, in this work, thermochemical energy storages are not taken in account and systems that involves sensible and latent heat are considered in the next sections.

4.1.2. Layout design of HGCS

On the design of HGCS (and Cold Thermal Energy Storage in general) there are mainly three options to transfer the cold thermal energy to the sink (or recovery it from the source):

- Transfer the cold energy directly the storage surface
- Transfer the cold energy by a heat transfer fluid
- Transfer the cold energy using directly the storage medium

In the first case, the storage exchange thermal energy by a direct contact with a solid, a fluid (by forced o natural convection) therefore the heat transfer rate is strictly dependent from the heat transfer coefficient and the heat transfer surface. Those systems are usually used for temperature control due to the low charge and discharge powers. In this case, the heat transfer area is increased by adding internal heat exchanging surface in the storage. The simplest way is the bulk configuration where the tank is directly designed with a heat exchanger configuration but, to increase the heat transfer area and increase the storage performance, a modular approach is often used (packed bed configuration). With regards to the Phase change materials (PCM) the most common way to include them in a containment. During the design of the encapsulation, the main objective is to maximize the energy density and the heat transfer charging and discharging. Heat transfer in packed beds, that includes random and structured packings, were extensively investigated by many researchers. However spherical shape is the most used in the packed bed configuration. The third possibility to transfer the stored energy is to use the HTF directly as a storage material. In the case of LAES, Li et al.[28] proposes a solution where

the cold energy rejected from the liquid air is stored directly in two different HTF (propane and methanol) stored in a two-tank configuration. PCM can be included in the HTF by means of microencapsulation. If the particles are small enough they can be part of the heat transfer fluid named slurry. In this case, the PCM is usually contained in small spherical or rod-shaped particles with a diameter of 1nm -1000nm made of a continuous film of polymeric material. The small diameter allows increasing the surface heat transfer area due to the large surface /volume ratio reducing the phase separation and improving the cycling stability. If the particles are small enough they can be part of the heat transfer fluid named slurry. The manufacturing process of microcapsules is more complex compared with the microencapsulation and can be done by means of two processes: physical or chemical. When the HTF is also involved as a storage medium, the heat transfer performance is improved with the use of suspended nanoparticles to enhance thermal conductivity and the efficiency of the heat transfer fluid.

4.1.3. Use of phase change materials in the microgrid scale LAES High Grade Cold Storage

On the design of the High Grade Cold Storage (HGCS) for a microgrid scale LAES, the following parameters should be taken into account:

- Proper storage temperature
- High Energy Density and Reduced Dimensions
- High Charge and Discharge Efficiency
- Good Cycle stability
- Low cost

The proper storage temperature range depends on the selection of the storage material that is important to exploit the maximum of waste cold available from the discharge section of the LAES. In a microgrid context, is always convenient to reduce the space of the entire grid controls, and storage systems. Therefore, the dimensions of each component (including the power generation system) should be taken into account during the design. Considering a LAES applicated as a small-scale energy storage it would be advantageous to reduce the dimensions of each component, including the HGCS. Therefore, a storage with high energy density is particularly important to reduce the dimension of the entire system. The high charge and discharge efficiencies depends both on the properties of the storage material and the geometry of the components energy storage itself. Cycle stability is important to avoid the degradation of

the storage system with the time that can affect the general performance of the LAES. Low cost is then important to guarantee an economic feasibility of the LAES. A High Grade Cold Storage can store cold thermal energy in all the three methods described above. However, the current solutions for LAES systems available are all based on a sensible heat storage system. The Highview pilot plant based at the University of Birmingham studied from different researchers[48][47], uses quartzite rocks a packed bed configuration involving, in the cold energy storage process, only sensible heat. In the literature Huttermann et al.[53] studied different storage materials potential application for a sensible heat storage applied to a LAES HGCS. The results from the authors propose polypropylene and high-density polyethylene as good materials for packed bed energy storage involving sensible heat, relating the efficiency of the system to the volumetric heat capacity. Although sensible heat energy storage represents the simplest way to store high grade cold thermal energy, it has a low energy density requiring large volumes to store small amounts of energy. Latent heat energy storage allows to store a larger amount of energy using the same amount of storage volume, that could be particularly suitable in a small-scale system as the microgrid scale LAES proposed in this work. Latent heat energy storage integrated to sub-zero applications offers a large variety of low temperature PCM. However, in the best of the knowledge, there is no PCM with a phase change temperature close to the air liquefaction temperature. Therefore, the only use of PCM as storage medium doesn't take advantage of the benefit of the latent heat storage since the huge temperature difference between the cold air (-196°C) and the phase change temperature of the PCM entail that, in most of the storage process, sensible heat is involved. The idea of this work is then a hybrid solution that integrates one or more part of latent heat storage materials (PCM) in the actual solution adopted for HGCS in LAES based on a sensible heat packed bed energy storage. Figure 4.3 shows a schematic of the idea of the hybrid HGCS proposed in this work.

The aim of the integration of Phase Change Materials in an HGCS is mainly to have:

- Reduced Dimensions of the HGCS (Higher energy Density)
- Stabilize Thermal fluctuations during charge and discharge

In this case, the storage has a multi-layered solid-PCM configuration. A similar concept was also proposed in the literature by Galione et al. [54] and Zanganeh et al. [55] with a thermocline that combines both solid and PCM materials for high temperature applications. The solution proposed by Zanganeh uses a layer of phase change material in a packed bed rocks heat storage to stabilize the temperature of the heat transfer fluid during the discharge.

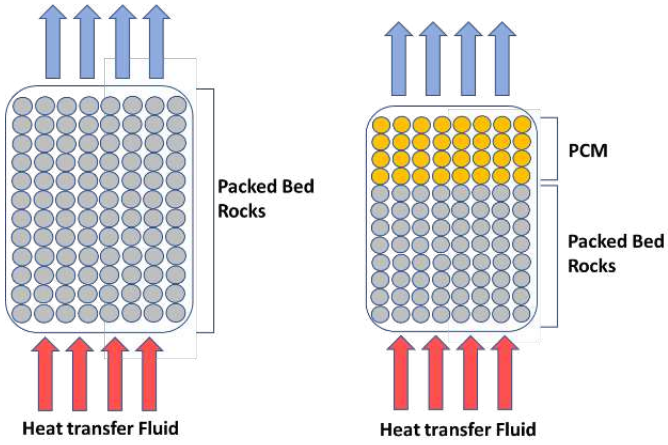

Figure 4.3.: sensible heat HGCS and hybrid HGCS

Galione compared, by numerical simulations, different solutions for a multi-layered packed bed for concentrated solar power applications. The results show that the multi-layered solution prevents the degradations of the thermal front compared with a pure thermocline, improving the storage efficiency. Furthermore, the comparison of a multi-layered solution that integrated both sensible and PCM materials results more efficient of a cascaded PCM.

4.1.4. Overview of Low Temperature PCM

The PCM used for thermal energy storage application can be classified by means of different criteria. A first classification can be done by temperature range where the liquid-solid phase transaction occurs. In this case is possible to divide the PCM in:

- High temperature PCM with a phase change temperature above 90°C
- Mid-temperature PCM (phase change temperature between 15-90 °C)
- Low temperature PCM temperature (phase change temperature below 15°C).

Figure 4.4 shows the various category PCM compared with the latent heat and melting temperature.

This work focuses on the study of low temperature PCM with a phase change temperature below 0°C (sub-zero temperature). PCM for sub-zero applications can be further classified by the nature of the components material (Figure 4.5) where can be divided into two main categories: organic and inorganicPCM

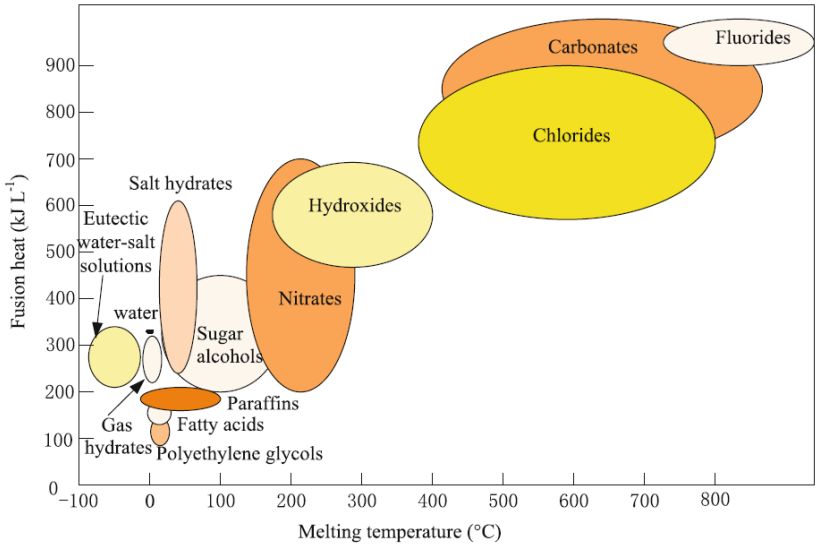

Figure 4.4.: PCM materials compared with their melting temperatures

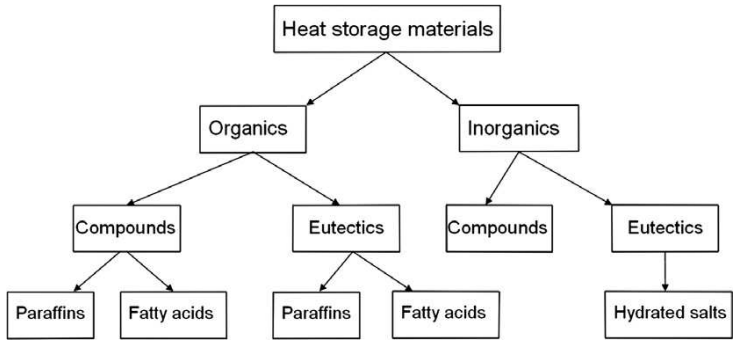

Figure 4.5.: Classification of low temperature PCM

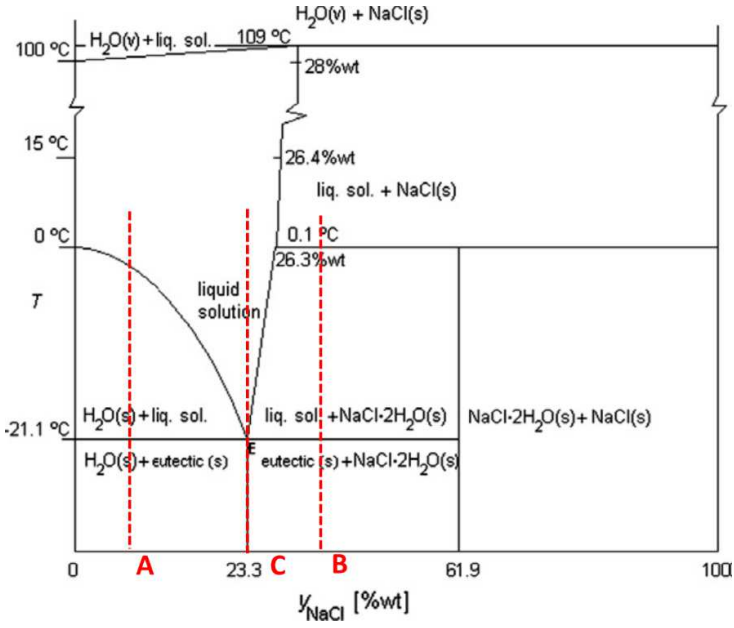

Figure 4.6.: Eutectic diagram for eutectic salts

In low temperature application, salts are used to lower the freezing point of the water, but the behavior of the solidification of the mixture it depends on the concentration of the salt in the water. Indeed, for the eutectic salt mixture, the complete melting and solidification without separation of the solution only appear at a particular value of the concentration of the solution called eutectic mixture. For a better explanation, it is necessary to refer to the phase diagram showed in Figure4.6 that refers to a mixture of sodium chloride and water.

In the case A (hypoeutectic region), when the mixture is cooled down ice particles separate from the mixture and the composition of the remaining liquid increases the percentage of salt until it reaches the eutectic composition (point E). On the other hand, for hypereutectic mixture (case B) crystal of salts separates from the solution and the percentage of the salt in the liquid decreases until it reaches the eutectic solution. In this case only when the mixture is eutectic (point E) the solution solidifies simultaneously with the same composition. Eutectic salt-water mixtures are characterized by a high heat of fusion and energy density, but on the other hand, they are subjected to high subcooling degree and suffer from phase separation that can affect the energy storage performance. Furthermore, during the design of HGCS using salts as PCM, the problem of corrosion should be considered to don't affect the cyclic stability. However, many techniques can be adapted to deal with those problems. For example, phase separation can be mitigated adding external

materials that bond the solution particle (such as a polymer) or increase the viscosity. Supercooling is usually managed by adding nucleating agents that help the nucleation of the solid particles. Another category of materials that can be used as a PCM is the non-eutectic materials most commonly represented by *alcohol solutions* and *paraffins* (or paraffin waxes). Alcohol solutions are used to lower the temperature of water and find an extensively in the form of ice slurry to be used as heat transfer fluid. This particular form consists of both a liquid state fraction and a solid-state fraction. The main advantage of slurries compared to a liquid state HTF is the latent heat stored in the ice particles that have a higher energy density compared to the liquid. Paraffin waxes have a good cyclic stability and shows a good latent heat with a small supercooling. Furthermore, they are compatible with most of the encapsulation material and are no corrosive. On the other hand, they suffer from low thermal conductivity and they are toxic and flammable. On improving the performance of non-eutectic solutions, external material such a metallic material or graphite are usually added to the PCM to increase the thermal conductivity. The design of the encapsulation and heat exchanger is another way to improve the material performance increasing the heat transfer surface area with the use of fins of finned tube heat exchanger.

4.1.5. Design of hybrid HGCS

TESLAB@NTU project

The hybrid HGCS with PCM integrated is part of a project done in collaboration with TESLAB@NTU based in the Nanyang Technological University of Singapore. The design consist of main steps that can be assumed as follow:

- PCM selection and Formulation
- Thermal Response and Thermal characterization of PCM
- Modelling and Develop an HGCS prototype

PCM Selection and formulation The main challenges regarding the design of systems involving latent heat storage are on the research and the study of improving the performance of the PCM, that should be selected with different criteria. The main requirements to be considered on the selection a PCM (both for high and low temperature) are the phase change temperature, that should be selected based on the application, and the relatively large latent heat of fusion.

However, all the main characteristics that a good PCM should have are [56]:

- Proper phase change temperature
- Large latent heat of fusion
- Cycling and chemical stability – this allows using the material many times without a consistent degradation of the performance of the storage system.
- Compatibility with other materials and low corrosivity – liquid PCM needs to be encapsulated to prevent leakage then the compatibility and the low risk of corrosion with the encapsulation material are fundamental.
- Low supercooling– when a PCM goes under phase change, the solidification may start at a temperature lower than the phase change temperature and the PCM is still involved on the sensible heat. This effect is called supercooling. A low supercooling is desirable since during this phase is necessary to reach a lower temperature to trigger the crystallization of the PCM. This lead to consider a large temperature difference between the charge and the discharge decreasing the efficiency of the system.
- High thermal conductivity – this material properties determines the power of charging and discharging the system
- Small volume change and low vapor pressure – to reduce the thermal and mechanical stress of the encapsulation
- Low cost and easy manufacturing – this is necessary to let the CTES competitive and feasible compared with other storage systems

Thermal Response and Thermal characterization of PCM During the selection of the PCM, it is fundamental to understand the thermal behavior of the PCM characterized by the heat transfer occurring during the processes of solidification and melting. The thermal characterization of PCM can be investigated with two approaches: experimental and numerical. The experimental approach, although its results are more reliable, has some relevant limit limitations. Indeed, this method requires longer time and higher costs, due to the purchase of the experimental rig and the need for set-up and calibration before to obtain reasonable data. Furthermore, at a large scale, the experimental approach can't be always applicable due to the need for a proper structure and environment to hold the test rig. On the other hand, numerical methods are more direct and simple to use offering the possibility to replicate different boundary conditions just varying the input parameters. Amongst all the numerical methods the 1-D approach is the simplest and the fastest way to

represents the heat transfer inside the PCM. Furthermore, a simple numerical code can be easily integrated into other numerical models that results useful in the design and a preliminary analysis of HGCS. Although the 1-D numerical methods are fast and simple to use, the reliability of the results needs a previous validation that should be supported by the experimental data.

Numerical Modelling and Developing of an HGCS prototype When the behavior of the PCM is well-known through the measurement of the material properties and the thermal characterization, is important to evaluate their integration on the HGCS during the charge and discharge of the energy storage. Numerical simulations are widely used in the design of packed bed in order to predict the performance of the storage. In the literature packed bed using spherical capsules are investigated both numerically and experimentally, but in the best of the knowledge, there are only experimental results available for cryogenic temperatures based on packed bed involving sensible heat. Therefore, it is important to develop a first lab-scale prototype with PCM materials to have a proper validation of the numerical model that can be used to assist the optimal design of a real-scale HGCS. The development of a validated numerical model is also useful to be integrated into other numerical models and evaluate the dynamic effect of the storage in the LAES or other energy systems where the HGCS can be applied.

4.1.6. Aim of this work

Figure 4.7 Shows the Gantt chart the activities of the hybrid HGCS design at TESLAB@NTU.

This work focuses on the task of the HGCS design regarding the **thermal response and thermal characterization of PCM**. In particular, the next sections present a methodology used to measure the thermal response and predict the thermal behavior of low temperature phase change materials that can be applied to assist the design of an optimized container sizing for HGCS. For this purpose, an experimental rig has been designed to test the thermal response and the results obtained have been used to validate a 1-D numerical model based on the effective capacity method and solved by MATLAB software. Due to their well-known properties, the methodology has been first validated using pure water as PCM materials. Then the methodology has been tested and further validated to on a sub-zero material based on aqueous ethylene glycol solution. The experimental data and the numerical results obtained from the 1-D numerical model are presented in chapter5.

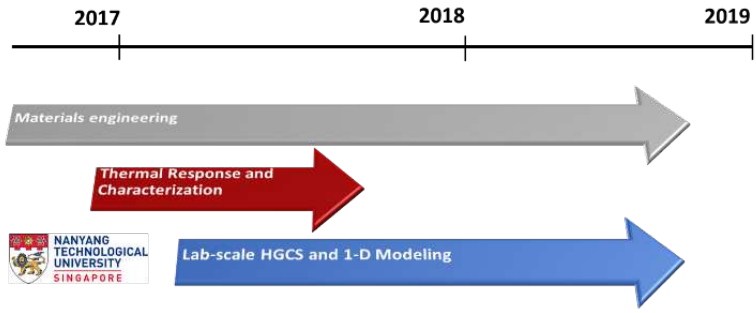

Figure 4.7.: Gannt diagram of TESLAB@NTU Activity

4.2. Materials and Methods

4.2.1. Experimental Rig

The experimental rig presented this work has been designed to obtain the solidification of the phase change material at a subzero temperature and the melting at ambient temperature. Furthermore, the experimental rig has to be able to measure the thermal behavior of the PCM along with the radial distances. Figure 4.8 shows the scheme of the experimental rig used in this work. The set-up consists of a PCM container to be placed alternately between a cold ethanol bath (solidification) and a hot water bath (melting) maintained at a constant temperature. The temperatures of the PCM in different positions of the container are recorded with four k-type thermocouples (0.3 mm) connected to a National Instrument data acquisition system (NI cDAQ 9133 with temperature module NI 9213) at the time interval of 0.5 s.

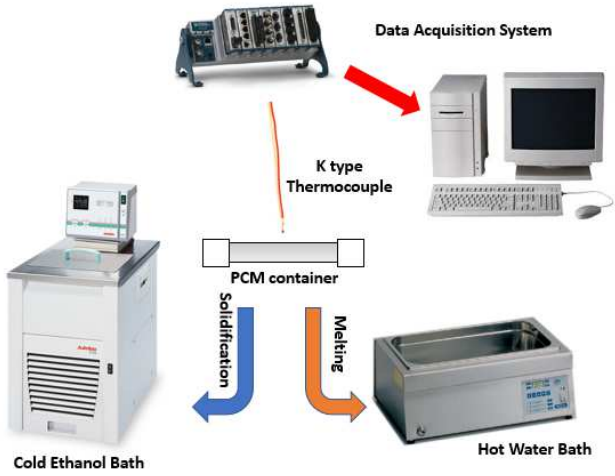

Figure 4.8.: Schematic of the Experimental Rig

PCM container

In order to obtain a successful validation of the 1-D numerical model, the PCM container has been designed to obtain a similar thermal behavior of the PCM involving a one-dimensional heat transfer process. In particular, the design specifics of the container are adopted to:

- Enhance the conduction on the lateral surface of the container
- Limit the conduction and the nucleation effects of the thermocouple
- Avoid internal pressurization caused by the expansion of PCM

The stainless-steel container (grade 316L), showed in Figure4.9 has been designed with a cylindrical shape and an internal diameter of 10mm with a wall thickness of 1mm. Stainless-steel has a high thermal conductivity of 13 $[W/mK]$ that reduces the thermal resistance of the wall. Stainless-steel is one of the most reliable materials for ultra-low temperatures. The heat conduction in the radial direction of the container has been enhanced insulating the end of the container by adding an external part made of PTFE (thermal conductivity 0.25 $[W/mK]$). When the container is closed with the two PTFE caps, the eternal air is trapped inside the container pressurizing the liquid above the atmospheric pressure that would change the PCM properties and create undesirable mechanical stress that could damage the container during the volumetric expansion due to the solidification of the PCM. To avoid this effect, a small screw is used to exhaust the volume of air when the container is closed,

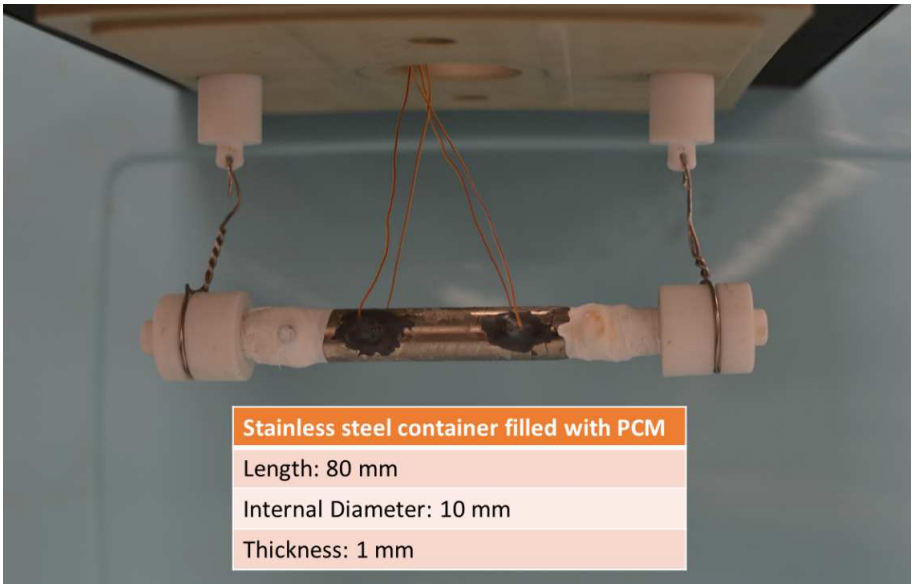

Figure 4.9.: PCM container and main dimensions

ensuring that the liquid PCM is at atmospheric pressure. The temperature of the PCM is measured with a 0.3 mm type K able to maintain a good accuracy with sub-zero temperatures. The small dimension reduces the effect of the thermal conductivity and nucleation that would be present during the phase of melting and solidification. The positions of the thermocouples inside the container are showed in Figure 4.10.

The thermocouple is funneled and supported through a plastic guide placed in the container through a small hole and secured with an epoxy resin suitable for sub-zero and cryogenic temperature.

4.2.2. Material selection and Properties characterization

PCM Selection

The methodology presented in this work has been validated with two steps:

- Calibrate and validate the set-up and 1-D model with an established PCM
- Test the methodology with alternative sub-zero PCMs (not available in the literature)

Therefore, different PCMs have been selected to establish the thermal characterization methodology. In this work, the results of two materials have been

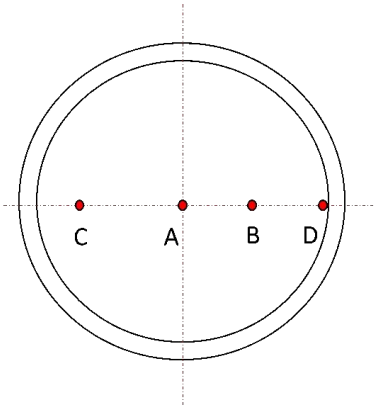

Thermocouple position	Distance from the internal wall
A	5 mm
B	3 mm
C	1 mm
D	0 mm

Figure 4.10.: Thermocouple position in the PCM container

presented. The first material selected for the calibration of the methodology is deionized water. Indeed, the thermal behavior of the phase change of water/ice has been already extensively studied in the literature. Ismail et al. [57] use the experimental results of the solidification of pure water to conduct a numerical study on the ice formation inside a spherical shell where the results are compared with the experimental data furnished by the authors. El Ghnam et al.[58] conducted an experimental study on the heat transfer on the melting and solidification of water in spherical capsules used for CTES for air conditioning application comparing different encapsulation materials and boundary conditions. The well known thermal behavior reported in the literature and the easy availability of the thermal properties, suggest deionized water as a good material that can be used to test the reliability of the experimental results and first validation of the methodology. The other PCM used for the for validation of the thermal characterization method proposed in this work is selected based on the following technical requirements:

- Good cycling and chemical stability
- Compatibility with the container
- Low sub cooling
- Low cost

Table4.1 resumes the main characteristics of the main PCM families described in the previous section. Although a lot of materials are included in the group of eutectic-salt/ water (salt aqueous), they have the disadvantage to be corrosive (not compatible with the stainless-steel container designed) and high subcooling. Paraffins and alkanoes, are less corrosive and has a medium latent heat of fusion, but they are flammable, and they have a high cost. Although they represent a good compromise, is preferable in this work to calibrate the experimental rig and validate the methodology, with a safer and cheaper and safer PCM before use and test expensive materials. On the other hand, alcohol aqueous solutions have different advantages that should be considered for an HGCS application. Aqueous alcohols are classified as a non-eutectic water PCM solution and are characterized by low phase separation and high compatibility to metals which are commonly used at cryogenic temperatures. Furthermore, they are low cost. For this reason, considering the requirements aqueous ethylene glycol (EG) has been selected as a second PCM. The good potential of aqueous EG has been reported by Kumano et al.[59] that compares the latent heat of ice of fusion of different alcohol solutions. Furthermore, non-eutectic alcohol solution has been also investigated by Sze et al.[60] where different aqueous ethylene glycol (EG) and ethanol solutions, are characterized by DSC measurements and bulk measurement at various concentration. In this work, a concentration of 30% of ethylene glycol (EG30) by weight in deionized water has been selected to limit the effect of the low crystallization and the low latent heat that characterize the aqueous solution with a high percentage of ethylene glycol.

Table 4.1.: Main characteristics of subzero PCM categories

PCM	Phase change temperature range	Latent heat of fusion	Solubility	Thermal conductivity	Corrosion	Cost
Alcohol aqueous	-114 °C to < 0 °C	Low	High	Low	Mild	Low
Salt aqueous	-86 °C to -1.6 °C	High	Only at eutectic points	Mid	High	Low
Organic (paraffins, alkanones)	-55.4 °C -0.5 °C	Medium	-	Low	Mild	High

Measurement of heat Capacity and Latent Heat

Differential scanning calorimetry (DSC, TA Instruments Q200) with refrigerated coolant system was used to measure the phase transition temperatures and heat capacities of PCMs. A dynamic heat rate at 1 °C/min was used and the enthalpy and heat flow values were taken at the melt phase of the PCMs. High-purity nitrogen (>99.995%) was used as the inert purge gas at a purge flow rate of 50 mL/min. The DSC has been calibrated with indium (temperature) and sapphire (heat flow) standards. All PCM samples and sapphire standard have been weighed using microbalance (Mettler-Toledo XP2U, 0.0001mg). Volatile PCMs were measured after being sealed in the T-zero aluminum hermetic pans. The calibration factors for specific heat capacity values were determined before each experimental run with PCMs, according to ASTM E1269-11 standard test method. Specimen were held at the starting temperatures for 5 minutes before and after the heating cycle.

Measurement of the thermal conductivity

Laser flash analyzer (LFA, TA Instruments DXF200) with a liquid nitrogen cooling system was used to measure the thermal diffusivities of the PCMs. The LFA has been calibrated with a standard test method (ASTM E1461) for thermal diffusivity by the flash method. This transient technique features short measurement times suitable for liquid samples. The system employs a solid-state detector in contact mode for improved sensitivity measurements at sub-ambient temperatures. The liquid samples were encapsulated in a specially designed non-pressurized, circular liquid cell with a sample size of 25.4 mm (diameter) and 0.104 mm (thickness). The sample's volume was fixed at 0.8 ml. Graphite paint was sprayed on the bottom layer of the cell to improve absorption of energy provided by a xenon-pulse laser source. High-purity nitrogen (>99.995%) was used as the inert purge gas. The maximum pulse width was used for low-conductivity samples and was set at 600 µs. The heating rates between temperature intervals were set at 5 oC/min and at least five temperatures were taken over -50 °C to 25 °C. From thermal diffusivity $\alpha[m^2/s]$, the thermal conductivity $k[W/mK]$ of the EG30 can be calculated as

$$k = \alpha \cdot c_p \tag{4.3}$$

The values of the specific heat capacity $c_p[kJ/kgK]$ are considered from the results obtained with DSC measurements. In this case the density of EG30 has been assumed constant (ρ =1027 kg/m^3]) and calculated as:

$$\rho_{EG30} = \frac{m_{water} \cdot \rho_{water} + m_{EG} \cdot \rho_{EG}}{m_{tot}} \tag{4.4}$$

4.2.3. Experimental Setup

Assembly of the container

The experimental setup starts the preparation of the container and the filling with the PCM showed in Figure 4.11. At first the each of four thermocouples (A) has funneled and fixed in a small plastic guide (B) at a fixed length according to the test positions showed in Figure 4.10, then each thermocouple is placed in the container as showed in Figure4.11a, and fixed with the epoxy resin (C). The container can be used when the epoxy resin is completely hardened and fully bonded. This drying process needs a minimum 16 hours, but it can be speeded up using a ventilated oven at low temperature (40 °C). When the container is ready,4.5 ml of liquid PCM are filled in, and the container is close by means of the internal cap (D). The volume of air that is pushed into the container during the sealing with the cap, is removed by an air exhaust screw. Then the container is further sealed with a sealing tape in order to prevent any leakage. An external cap is then used to support the container on the cap of the thermal bath. In order to reduce the thermal stress and avoid breaking or damage, during the experiments, a space gap between the top of the internal cap (D) and the internal of the external cap (C) has been considered to allow the internal cap to move during the expansion of the PCM that takes place during the solidification. In the end, the four thermocouples are logged a National Instrument data acquisition system (NI cDAQ 9133 with temperature module NI 9213) and the data are recorded at a time interval of 0.5 seconds and elaborated with LabVIEW.

The thermal bath Temperatures for the solidification (charging) and melting (discharging) are reported in Table 4.2.

Table 4.2.: Temperatures of cold and warm thermal bath used for the tests

	Thermal Bath Temperature [°C]	
	Cold Bath	Warm Bath
DI Water	-10	24
EG30	-40	24

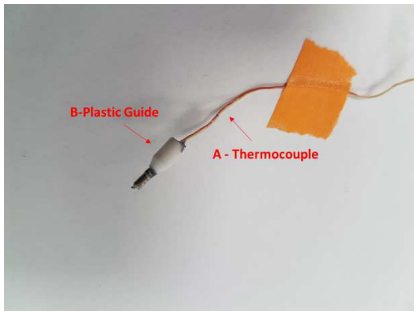

(a)

(b)

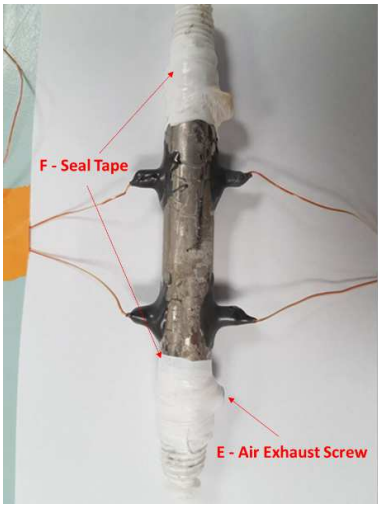

(c)

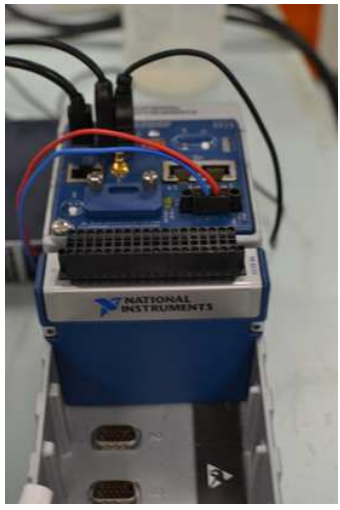

(d)

Figure 4.11.: Assembly of the container

Charging

During the charging process (Figure 4.12), the PCM temperature inside the container is first stabilized at 24°C in the hot water thermal bath and then placed in a Julabo ultra-low refrigerated circulator (FP89-HL) with a lower temperature limit of -90°C at the charging temperature. Ethanol was used as heat transfer fluid, that allows reaching subzero temperatures without freezing. The PCM remains in the Cold Ethanol Bath until the temperature in the center of the container has been stabilized at the charging temperature. The container is then rapidly moved in the hot water thermal bath for the discharging process.

Discharging Process

After the PCM has been stabilized at the charging process, the container is then rapidly moved in the warm water thermal bath for the discharging process (Figure 4.13), where the PCM is placed a static warm thermal bath (P-selectr unitronic OR) with pure water at the temperature of 24°C. When the temperature in the center of the container has been stabilized at the hot water bath temperature the PCM is considered completely discharged.

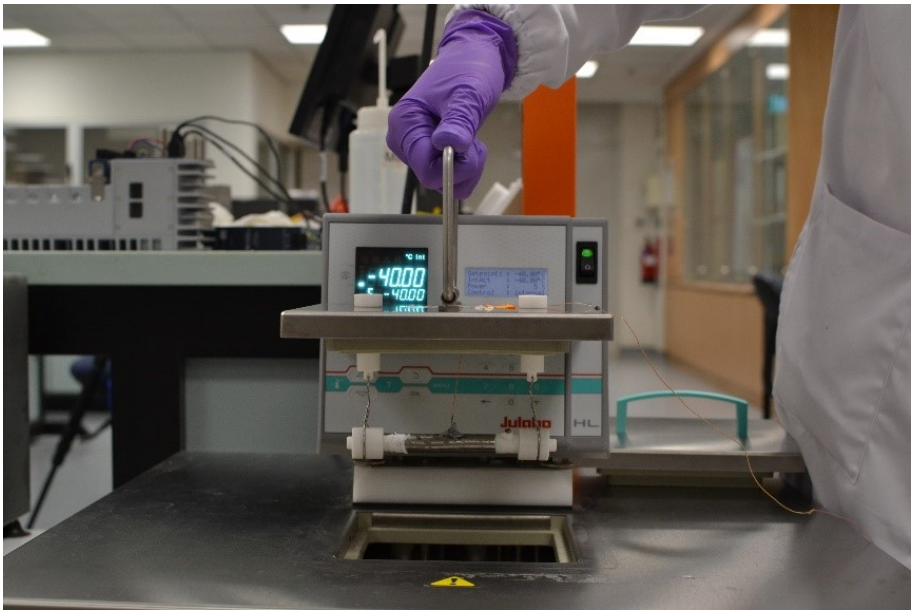

Figure 4.12.: Charging of the PCM in the cold thermal bath

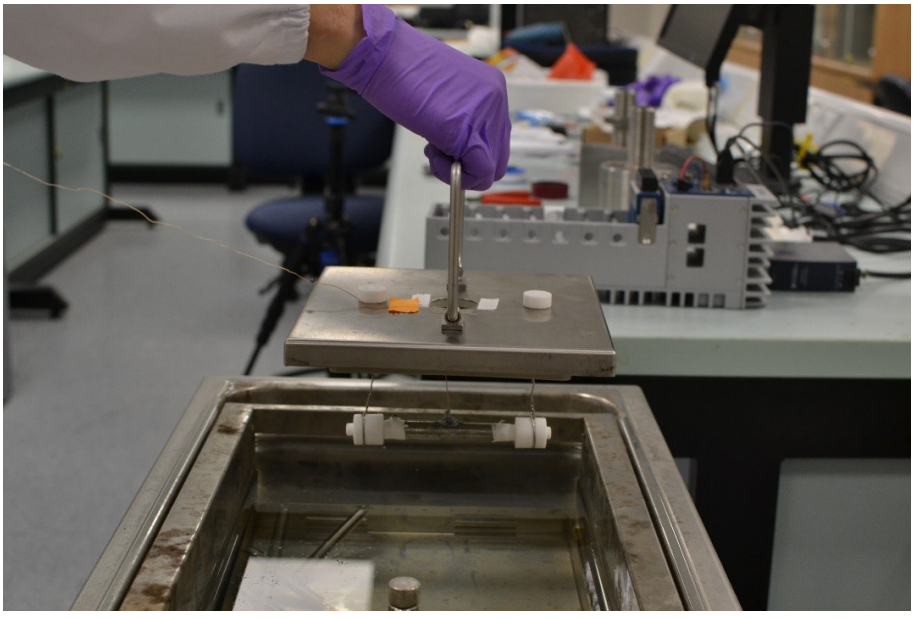

Figure 4.13.: Discharging of the PCM in the cold thermal bath

4.3. 1-D Numerical Model

4.3.1. Introduction to phase change numerical characterization

The understand and the prediction of the heat transfer inside the phase change materials results difficult due to the change of thermophysical properties of the material due to the temperature variation. Furthermore, numerical modeling requires a previous understanding of the mechanism of heat transfer involved during the phase change. Indeed, the heat transfer mechanism during the solidification and melting of the material can be considered in terms of conduction and convection. The first studies on the phase change problem conducted by Lame and Claperyon in 1831 consider only conduction as a main heat transfer process, but other researchers affirm that the convection should be not neglected when phase change problems are studied. Essentially, both convection and conduction can be involved at the same time but the understating of which heat transfer mechanism is predominant still represent the major difficulty to understand. The mathematical representation of heat transfer involving phase change is included in the category of moving-boundary problem (or Stefan Problem) since the interface between of the solid and liquid is moving with the time. The simplest solution considers that only one phase is involved in the phase change and the rate of melting can be related to a dimensionless number called the Stephan number that represents the ratio of the sensible heat of the liquid phase and the latent heat. The Stefan problem can be also represented in a two-phase problem where the heat flux through the solid-liquid interface can be written as [61]:

$$\rho_{PC} L \Big(\frac{ds(t)}{dt}\Big) = k_s \Big(\frac{\delta T_s}{\delta t}\Big) - k_l \Big(\frac{\delta T_l}{\delta t}\Big) \tag{4.5}$$

Where L is the latent heat of fusion, $\rho_{l,s}$ is the density of the solid-liquid interface, $s(t)$ is the interface position in the time t. The term k_s, k_l and T_s, T_l are the thermal conductivities and the temperatures of the solid and the liquid respectively. Considering the non-linearity of the interface location, analytical solutions of the problem are limited to a few numbers of cases that involve specified geometries and boundary conditions.

Numerical model based on pure conduction

Based on the pure conduction heat transfer mechanism, the numerical models used to understand and predict the heat transfer occurring during the phase change have been extensively reviewed in the literature and can be divided in:

- Fixed Grid Method
- Adaptive Grid method
- Hybrid method

In the *fixed grid* the conditions of the phase change interface are not treated explicitly, and the governing equation is the same for both solid and liquid phase. In this case, the space is divided into fixed grids and the quality of the discretization is crucial to obtain a good model performance. In the *adaptive grid* method are used to obtain a model with a higher grid density in the in the solid-liquid interfaces. Therefore, the grid adapts at each timestep to track the melt front. The adaptive grid approach includes two main methods: the h-method and the moving mesh method. Hybrid method uses a combination of both methods. Amongst the method described above, the fixed grid method uses standard solution procedure of the general energy balance equation and is the easiest to implement, versatile and adaptable. Therefore, only fixed grid methods are considered and described in this section, and the most widely used are:

- Enthalpy method
- Heat Capacity Method

Enthalpy method In the enthalpy method, the variation of the temperature in the phase change transition is express in terms of variation of enthalpy[62]. In this case, the Stefan Problem is simplifying introducing a governing equation that is the same for both the solid and the liquid phase. This method is applied for the isothermal phase change process and the equation representing the energy balance is express in terms of the volumetric enthalpy and the variation of temperature. Therefore, is necessary to know the function that relates temperature and enthalpy during the phase change. This method is mostly applied for isothermal phase change where, in this case, the energy balance can be written in terms of volumetric enthalpy as:

$$\frac{\delta H}{\delta t} = \nabla[k(\nabla T)] \tag{4.6}$$

Where the total volumetric enthalpy δH can be considered as a sum of sensible and latent heat as:

$$H(T) = h(T) + \rho_{PC} f(T) L \tag{4.7}$$

$$h = \int_{T_{PC}}^{T} \rho c_p dT \tag{4.8}$$

The liquid fraction $f(T)$ in the case of isothermal phase change can be assumed a value between 0 and 1.

$$f = \begin{cases} 0 & T < T_{PC} \quad \text{solid} \\ (0,1) & T = T_{PC} \quad \text{phase change (mushy)} \\ 1 & T > T_{PC} \quad \text{liquid} \end{cases}$$

Integrating the equations 4.6 and 4.7 , the energy balance equation considering a 1-D heat transfer can be written, as:

$$\frac{\delta h}{\delta t} = \frac{\delta}{\delta x}\left(\alpha \frac{\delta h}{\delta x}\right) - \rho_{PC} L \frac{\delta f}{\delta t} \tag{4.9}$$

Although the enthalpy method is versatile and easy to apply, it can be subjected to temperature oscillation that represents the major disadvantage.

Effective Heat Capacity Method In the heat capacity method, the latent heat is considered in terms of an equivalent (effective) heat capacity during the phase change transition. The effective heat capacity during the phase change is the sum of the average specific heat capacity of the solid and the liquid phase of the material and a term proportional to the latent heat of the material (energy stored during the phase change) divided for the phase temperature range, that can be written as[63]:

$$c_{eff} = \frac{L}{T_2 - T_1} + c_{p,s} \tag{4.10}$$

Where the term $(T_2 - T_1)$ represent the phase change temperature range and $c_{p,s}$ is the specific heat capacity of the solid phase. Introducing the heat capacity method, the energy balance equation, for one dimensional problem can be written as:

$$\rho c_{eff} \frac{\delta T}{\delta t} = k \frac{\delta^2 T}{\delta x^2} \tag{4.11}$$

$$c_{eff} = \begin{cases} c_{p,s} & T < T_1 \quad \text{solid} \\ \frac{L}{T_2 - T_1} + c_{p,s} & T_1 \leq T \leq T_2 \quad \text{phase change (mushy)} \\ c_{p,l} & T > T_2 \quad \text{liquid} \end{cases} \tag{4.12}$$

The phase change range temperature included in the definition of effective heat capacity allows this method to be applied to non-isothermal phase change, therefore it requires a small timestep when a narrow phase change temperature range is considered, increasing the calculation time. To solve the energy balance equation described above they can be solved discretizing the problem applying a finite-difference (or finite volume) or a finite element technique. Finite element techniques are able to handle complex problems and boundary conditions, but on the other hand, the solving algorithm results complicated. Nowadays, the use of finite difference method on solving heat transfer problem is simplified with the use of auxiliary software such as Ansys Fluent[64] and COMSOL[65]. On the other hand, finite difference methods are easier to implement and offer the possibility to obtain good accuracy when simple geometries and boundary conditions are considered. In the literature, many authors propose the application of fixed grid methods solved using a finite difference method. Lo Brano et.[66] al used a finite difference to solve a heat transfer numerical model based on the enthalpy method to represent the temperature profile of a PV-PCM system. Zhao et al.[67] studied the heat transfer of zinc encapsulated in nickel and eutectic salt mixtures in a spherical capsule using a finite difference approach to predict the time for charging and discharging. Lamberg et al.[68] compared both enthalpy method and the effective heat capacity method to study the heat transfer in PCM heat storage. The results, compared with experimental data shows that both methods have good accuracy and the heat capacity method has a better estimation of the temperature profile. Costa used the enthalpy method to study the thermal performance of a latent heat thermal energy storage. The temperature was evaluated with both one dimensional and 2-D approach considering both convection and conduction. Results were compared with other numerical models in the literature.

Inclusion of Convection in numerical models

The enthalpy and effective capacity method described above are based on a pure conduction model, but recent literature works confirm that for a good prediction of the phase change, the natural convection has a major contribution on the melting phase that should be considered on the modeling. Tan et al conducted an experimental and computational study of the melting of a phase change material inside a sphere. The results show that the conductive heat

transfer dominates in the first period of melting, but as the melting region increases the bouncy driven convection force becomes relevant. In the work conducted by Lamberg et al.[68], the results show the using the model that considers pure conduction as a heat transfer mechanism, it poorly represents the phenomena during the melting phase. The most common approach to include the convection is by using an approximate solution. In this case, the convection can be included in terms of an effective thermal conductivity k_{eff}. This is often related to the thermal conductivity k_{liquid} as a function of the Rayleigh number Ra and the thickness of the liquid portion during the phase change. Amin et al.[69] proposes an empirical correlation for the effective thermal conductivity based on CFD simulation and experimental results. Liao et al.[70] simulated the melting of NaNO3 inside a spherical capsule. In this work, a convective model and a pure conduction model are compared and validated using experimental data. Furthermore, the conduction model includes a novel relation for the effective thermal conductivity proposed by the authors.

This method allows to include the effect of the natural convection using the enthalpy method or the effective capacity method described above. Many authors in the literature propose different correlations to calculate the value of the thermal conductivity for different materials.

4.3.2. Simulation assumptions

Due to the simplicity of the method and the possibility to solve non-isothermal phase change, the heat capacity method is used to solve the governing heat transfer equation that represents the phase change. The objective of this work is to validate a fast and versatile numerical method that can easily represent the heat transfer occurring during the charging and discharging process of the PCM. For this reason, the phase change problem has been simplified as a 1-D heat transfer process. Furthermore, the 1-D numerical model can be easily integrated to simplify the phase change problem in other numerical models such as the complete model of the HGCS. Considering the cylindrical geometry of the container. In 1-D form, the energy equation can be written in cylindrical coordinates as:

$$\rho c_{eff}\left(\frac{\delta T}{\delta t}\right) = k\frac{1}{r}\frac{\delta}{\delta r}\left(r\frac{\delta T}{\delta r}\right) \tag{4.13}$$

Where the effective heat capacity is defined from eq.4.12.

Boundary conditions for the model

For the 1-D numerical model simulation the following initial and boundary conditions are assumed and resumed as follow:

$$\begin{cases} k\frac{\delta T}{\delta r} = 0 & r_i = 0 \\ T = T_{bath} & 0 \leq r_i \leq r_1 \quad (t = 0) \\ -\frac{\delta T}{\delta r} = Q & r_i = r_1 \end{cases}$$

Where, referring to Figure 4.14, r_1 represents the internal radius of the container (5mm) and r_2 is the external radius (6mm). $Q[kW/m]$ represents the heat transfer from the boundary to the material and is considered as the contribution of the convection heat transfer coefficient and the thermal resistance due to the wall of the container represented by the thermal conductivity k_{cont} (13 W/mK):

$$Q = \frac{T(r_i, t) - T_{bath}}{\frac{1}{h_{conv}} + r_2 \frac{ln(r_2/r_1)}{k_{cont}}} \tag{4.14}$$

When all the boundary conditions are defined, the energy based equation (eq.4.13) described above has been discretized using a finite difference method with a fully implicit scheme solved by MATLAB software.

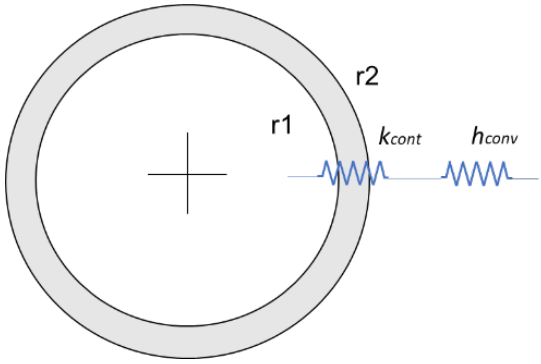

Figure 4.14.: Thermal resistance of the container

4.3.3. Calibration of the 1-D Model

The current methodology proposed in this work has been validated comparing the experimental results obtained with the solidification (charge) and melting (discharge) of deionized water with the numerical 1-D model results. The validation has been done in two steps:

1. Calibration of the numerical model
2. Validation with experimental results (section)

The calibration of the numerical model has been done setting the boundary conditions that optimize the match between the experimental curves and the numerical results. In particular, the main parameters that affect the time of charge and discharge is the heat transfer convection coefficient that controls the heat transfer between the surface and the PCM. For simplicity the calibration of the model has been done in one point, that corresponds to the center of the container (position A in Figure 4.10)). For that purpose, a single thermocouple container showed in Figure 4.15, has been used. The specification of the single thermocouple container is the same as the one presented in the previous chapter. The only difference concern in the number of thermocouples. Indeed, the container showed in Figure4.15 has only one thermocouple placed in position A (center of the container) measuring the temperature of the PCM in one point. This allows limiting the possibility of heat conduction and nucleation due to the presence of four thermocouple in the PCM.

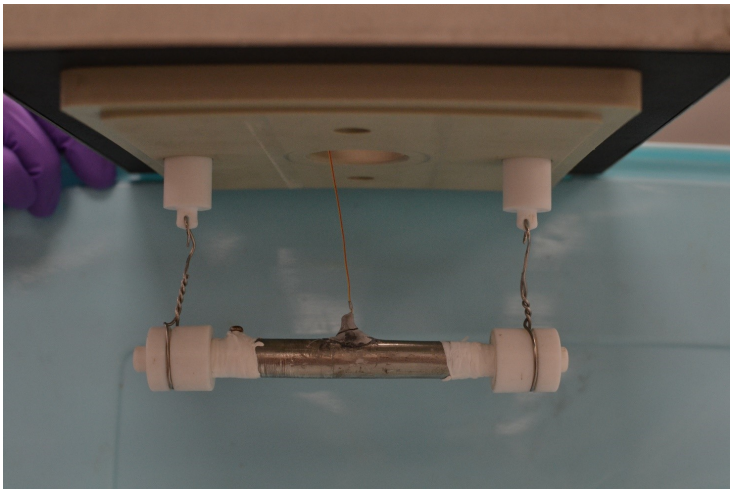

Figure 4.15.: PCM container with a single thermocouple for the methodology validation

Solidification

In the case of solidification when the PCM is placed in the cold bath, it is subjected to a fluid motion due the refrigerated circulator that lead to assume the boundary condition for the model as a forced convection. Also in this case, the Nusselt number can be related with some simple empirical correlations, for a cylindrical geometry, with the Reynolds Re and the Prandtl Pr as[71]:

$$Nu_{forced} = \frac{h_{forced}D}{k} = MRe^N = M\Big(\frac{VD}{\upsilon}\Big)^N Pr^{1/3} \tag{4.15}$$

Where D is the container diameter, V is the velocity and υ is dynamic viscosity. M and N are two constants which depends on the value of the Reynolds number (for $4000 < Re < 40000 M = 0.193, N = 0.618$). Since, it is difficult to estimate the velocity V of the flow in the cold bath, different assumptions of the Nusselt number has been made in order to find an appropriate value that better represent the phenomena. The properties have to be calculated for the external fluid at the film temperature $((T(r_2, t = 0) - T_{bath})/2)$ reported in Table4.3.

Melting

When PCM is placed in a static water warm bath for the melting process, the convection heat transfer coefficient can be calculated considering free convection outside the container, assuming pure water as transfer fluid. In this case the Nusselt number can be related as function of the Rayleigh number assuming an empirical correlation [71]:

$$Nu_{free} = \frac{h_{free}D}{k} = ARe^B = A\Big(\frac{g\Gamma(T(r_2, t = 0) - T_{bath})D^3}{\upsilon\alpha}\Big)^B \tag{4.16}$$

Where, g is the gravitational acceleration, Γ is the coeffcient of thermal expansion, A and B are two constants that has been estimated to fit the experimental data. The thermal bath properties have to be calculated for the external fluid at the film temperature $((T(r_2, t = 0) - T_{bath})/2)$. However, when the film temperature results negative, the film temperature refers to the absolute value calculated.

Table 4.3.: Film temperature warm and cold bath properties used for the heat transfer convection coefficient calculation

Properties[72]	Warm Bath (water at 7/8°C)	Cold Bath (ethanol at 7°C)	Cold Bath (ethanol at -8°C)
$k[W/mK[$	0.57	0.169	0.1736
$v[cm2/s]$	0.0151	0.0194	0.0267
$\alpha(m2/s)$	0.136 $*10^{-6}$	-	-
Pr	-	21.65	27.3
$\Gamma[1/K]$ [73]	0.000045	-	-

Chapter 5.

Thermal characterization of Phase Change Materials for LAES High Grade Cold Storage: Results

This chapter reports the results of the thermal characterization obtained with the methodology described in the previous chapter. The first section 5.1 of the chapter shows the experimental results obtained with the experimental rig previously described. In particular, the result of the characterization through Different Scanning Calorimeter DSC and Laser flash Analyzer LFA of the aqueous ethylene glycol at 30% (EG30) are first reported. Then the thermal response of DI water and EG30 during the solidification and the melting inside the PCM container is shown. The calibration of the 1-D numerical model with the experimental results obtained with the melting and the solidification of DI water is reported in section 5.2. To test and validate the methodology, the next section 5.3 shows the results of the application of the calibrated numerical model on the EG30. Discussion and main findings are reported in the last section 5.4.

5.1. Experimental Results

5.1.1. Aqueous ethylene glycol (30%): Material Characterization

Thermal Properties

Figure 5.1 show the freezing curve of aqueous ethylene glycol (30%). The results show that for the material selected a heat flow peak is reached at a temperature of -16°C.

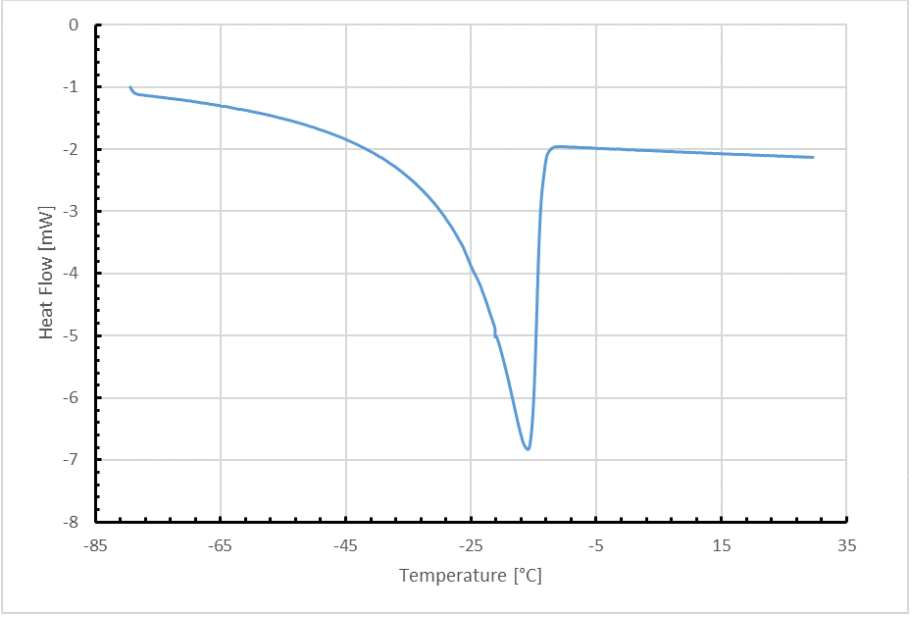

Figure 5.1.: Experimental results of DSC measurements for aqueous ethylene glycol (30%)

Thermal Conductivity

Fig shows the thermal conductivity calculated from the LFA results of the thermal diffusivity at different temperatures obtained from the melting of aqueous ethylene glycol (30%). It is worth to notice the gap between the thermal conductivity of solid and the liquid corresponds to the peak melt temperature determined from DSC (Figure5.1). The results show that the diffusivity slightly decreases when the temperature of the liquid is decreased ad significantly increase for the solid phase after the -20°C.

The results of the thermal conductivity calculated from the eq.4.3 are resumed in Table 5.1.

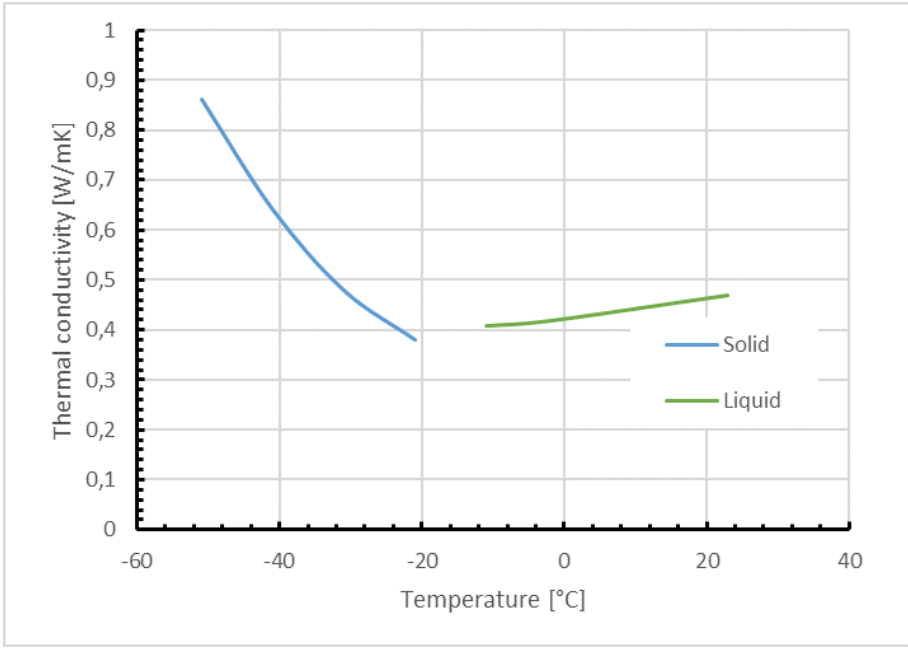

Figure 5.2.: Thermal conductivity of aqueous ethylene glycol (30%) calculated from the LFA results

Table 5.1.: Thermal conductivity of aqueous ethylene glycol (30%)

Temperature [°C]	$k[W/mK]$
-51	0.870974
-41	0.647391
-31	0.483875
-21	0.383763
-11	0.412344
-2	0.422826
23	0.474987

5.1.2. Thermal Response of Deionized Water

Charge - solidification Figure5.3 shows the experimental results of two test (Test 1 and Test 2) with the solidification of deionized water in a different position of the container. Comparing Figure 5.3a and Figure 5.3b there are some slight differences between the two tests. In position A the experimental curves of Test 2 (Figure 5.3b), has a slightly longer time of charge (around 10 sec) and a higher supercooling. On the other hand, the curves in other positions B, C and D, showed in figures has the same time of charge and a similar trend for both the tests. The only difference can be noted on the supercooling degrees between the curves. However due to the complexity of the crystallization process is not easy to ensure a complete repeatability of the tests. Furthermore, the small dimension of the container and the narrow position of the four thermocouples increase the sensibility of the boundary conditions that can affect the repeatability. Referring to the position reported in Figure5.3, the position A (placed in the middle of the container) has obviously the longer phase change duration and time of charge compared to the other positions. In all the cases is possible to notice that, when the container is placed in the cold bath, the temperature rapidly decreases with a velocity inversely proportional to the distance from the container wall. Before starting the phase change, the water reaches a temperature lower than the phase change temperature (supercooling) then the nucleation is activated and the temperature of the PCM remains constant until the solidification is ended. Generally, the supercooling degree during the solidification depends on the different factor that can be resumed:

- Quality of nucleation (Heterogeneous or Homogeneous)
- Rate of cooling
- Roughness of a metallic surface

Indeed, the higher supercooling degree can be noticed in position D close to the wall of the container where the rate of cooling is higher compared to the other positions. In the last part of the solidification curve, the temperature of the ice decreases until it reaches the cold bath temperature. In this case, the time involved to reach the cold bath temperature in position A corresponds to the time of charge of the bulk.

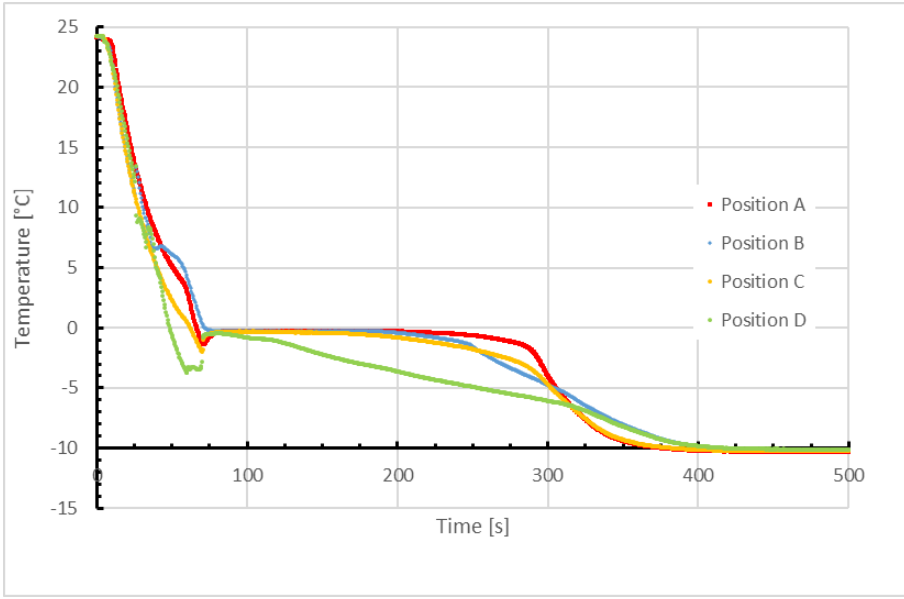

(a) *Test 1*

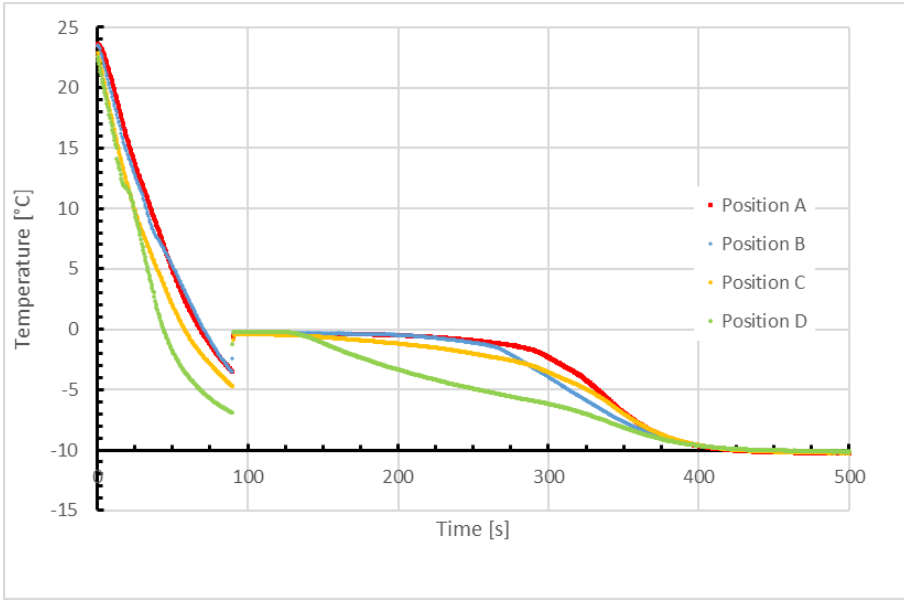

(b) *Test 2*

Figure 5.3.: Charge - solidification of pure DI water in different in position A,B,C,D

Discharge - melting Figure5.4 shows for the same PCM container and the same positions of Figure4.10, the experimental results of the melting obtained immediately after the solidification of pure deionized water. The curves showed in Figure5.4 for Test 1 and Test 2 are similar, with the same time of discharge for all the container positions. Indeed, the melting of solid material l is simpler and is easier to obtain a repeatability of the tests compared to the solidification. In general, the experimental curves of Test 1 and Test 2 confirm the reliability of the experiment and both the tests are compared with the numerical simulation conducted with the 1-D numerical model presented above. Also, in this case, the longer phase change in in the position A. In the position next to the wall the phase change results hard to catch due to the higher heat transfer. However, the phase change area can be denoted on the change of curvature around the phase change temperature. When the ice is completely melted, the temperature of the water rises until it reaches the warm bath temperature defining the discharge time of the bulk.

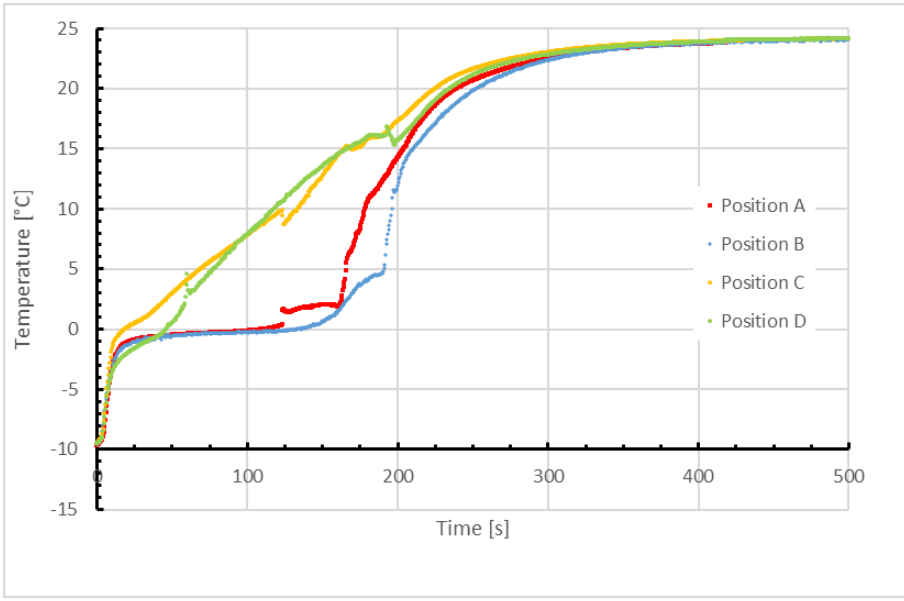

(a) *Test 1*

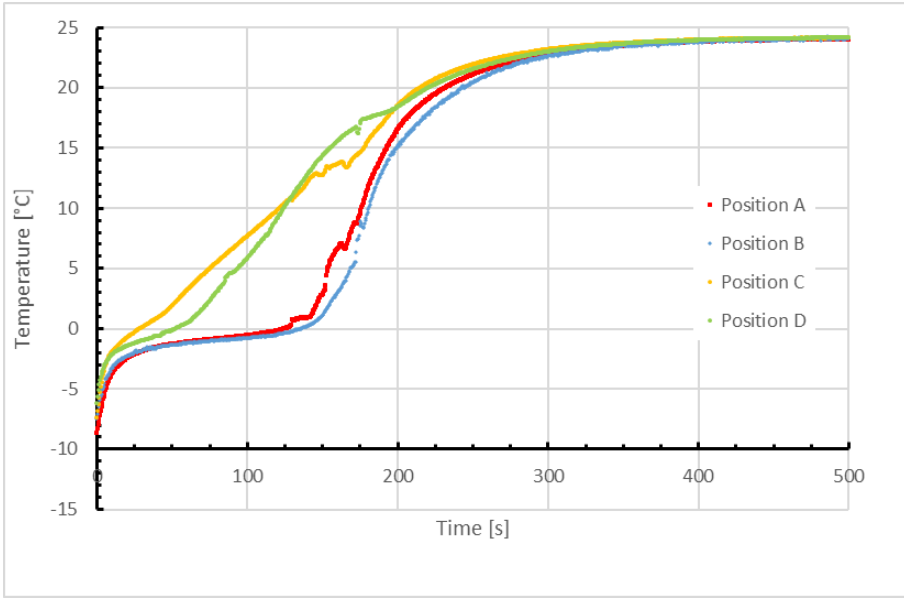

(b) *Test 2*

Figure 5.4.: Discharge - melting of pure DI water in different in position A, B, C, D

5.1.3. Thermal Response of Aqueous ethylene glycol 30% in DI water (EG30)

Charge - solidification Figure5.5 shows the experimental curves obtained from the solidification of the EG30 in different container positions. In this case is possible to notice that the behavior of the PCM is similar in both the tests. A slight difference can be noticed in Position A and Position D showed in Figure5.5 where the supercooling degree is slightly higher in the case of Test 1. However, the repeatability of the test is considered validated. The results show a short phase change phase that is longer and clear just in the center of the container (position A) and almost absent in the wall of the container. This is due to two main reasons:

- Low latent heat of the PCM
- High Rate of Cooling

The DSC results presented in Figure 5.1. shows a latent heat of fusion of around 93 KJ/kg, almost three times less than the pure water. The high rate of cooling is due to the temperature difference between the cold thermal bath (-40°C) and the warm thermal bath (24°C). From the experimental curves is possible to notice that during the phase change the plateau occurs at a lower temperature than the phase change temperature founded from the DSC measurements. These phenomena are common when PCM is characterized by a low rate of crystal growth [74] that results to have a dominant influence on the thermal behavior. Then the lower melting temperature highlighted by position A is reached when that the latent heat of the PCM equals the heat transfer in the material. However, the evidence of the phase change in position A, B and C is considered sufficient to proceed with the validation of the methodology. On the other hand, the supercooling of the PCM is evident in both the tests only in position D close to the container wall where the rate of cooling is higher. However, in position C, the high rate of cooling due to the close wall position, entail an immediate solidification where the phase change and the supercooling are not possible to catch with the current experimental rig.

Discharge - melting The experimental curves obtained from Test 1 and Test 2 regarding the melting of the EG30, are showed in Figure5.6. The curves obtained are similar for both the test confirming the reliability of the experimental data. In this case the phase change can be only observed in the position A with the change of the melting curve of the around -16°C. The boundary conditions due to the current experimental set-up, doesn't allow to obtain a clear plateau during the melting. In this case the validity of the model is verified evaluating the general behaviour of the melting curves.

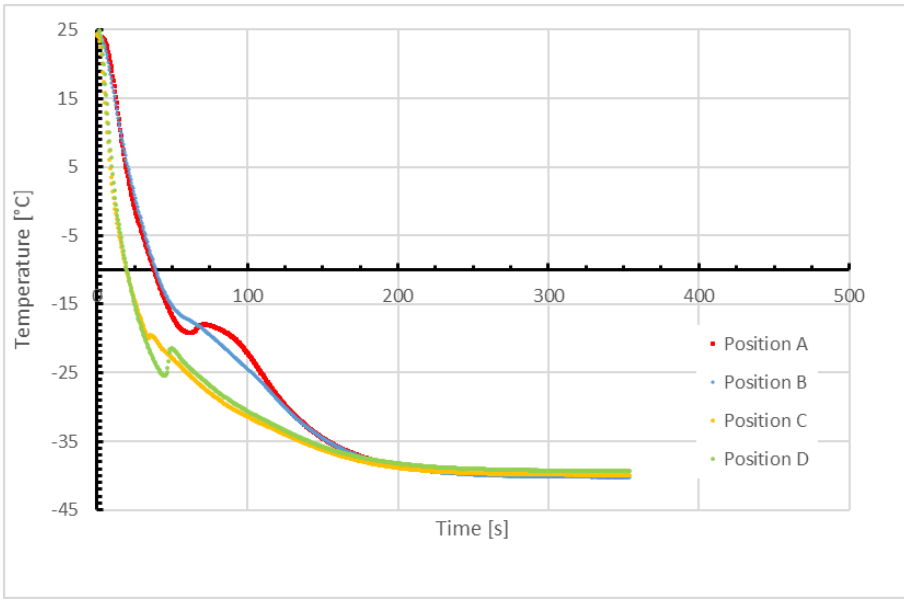

(a) *Test 1*

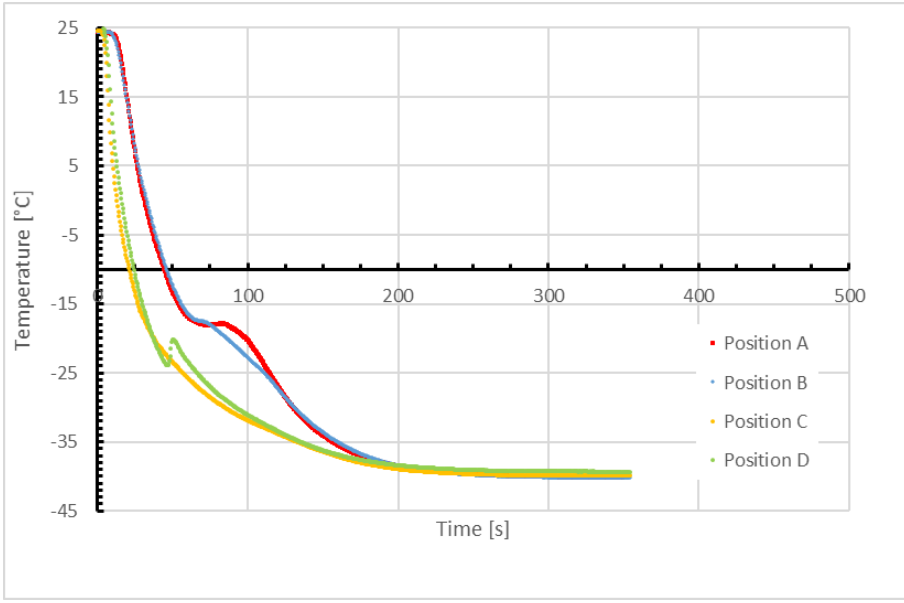

(b) *Test 2*

Figure 5.5.: Charge - solidification of EG30 in different in position A,B,C,D

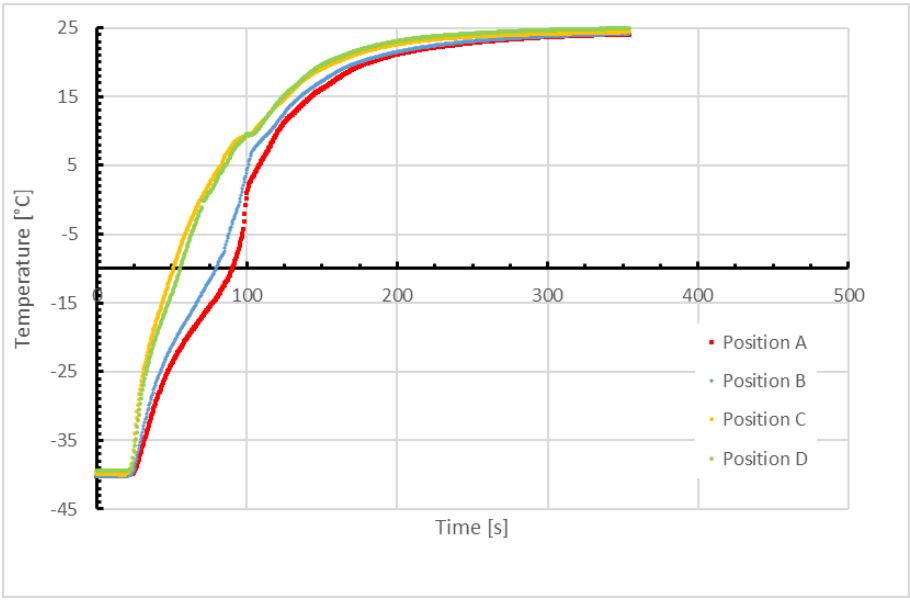

(a) *Test 1*

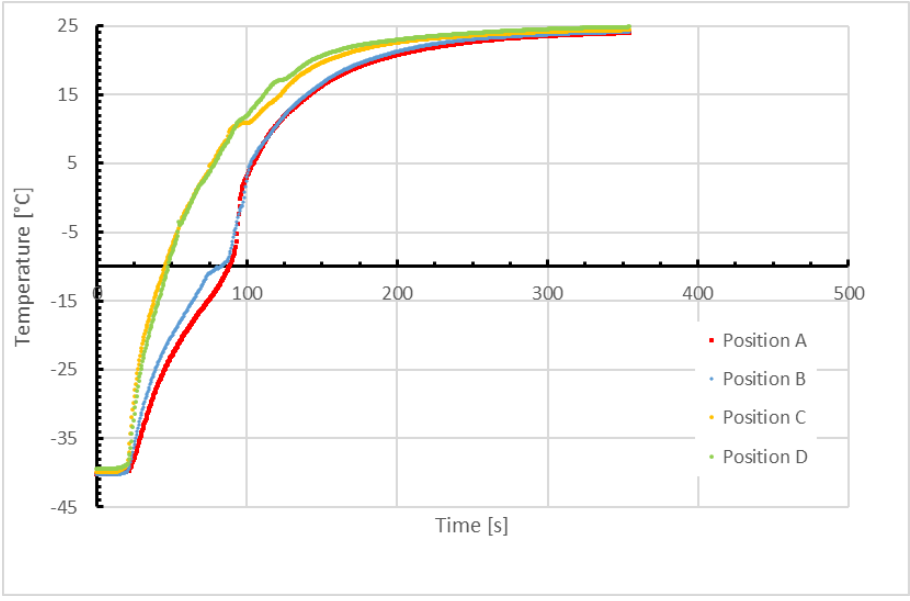

(b) *Test 2*

Figure 5.6.: Discharge - melting of EG30 in different in position A,B,C,D

5.2. Calibration of the 1-D Model

This section reports the results of the calibration of the 1-D numerical model with the methodology described in section 4.3.3. In particular, the numerical results are obtained optimizing the boundary conditions to fit the experimental results of the melting and the solidification of pure DI water placed in the single thermocouple container showed in Figure 4.15 and described in the previous chapter.

Table5.2 reports the properties of deionized water that serves as the inputs for the numerical model to solve eq.4.13. In order to have an accurate approximation, the properties of the material during the phase change (PC) are assumed to change according to the liquid fraction f_l [75]. The natural convection, that results as a dominant heat transfer mechanism in the melting process, has been taken into account introducing an effective thermal conductivity k_{eff} for the liquid phase. For deionized water, the effective thermal conductivity ($k_{eff} = 0.98[W/mK]$) has been taken from the literature where the liquid thermal conductivity has been increased of 75% [76].

Table 5.2.: DI water properties used for the 1-D numerical model

PCM Properties	Liquid $>T_2$	Phase Change	Solid $< T_1$
$\rho[kg/m3]$	1000	$\rho_{PC} = (1 - f_l)\rho_s + f_l\rho_l$	917.4
$c[kJ/KgK]$	4.20	$c_{PC} = (1 - f_l)c_s + f_l c_l$	2.11
$k[W/mK]$	0.558 (k_{eff}= 0.98)	$k_{PC} = (1 - f_l)k_s + f_l k_l$	2.108
$L[kJ/kg]$	-	334	-
f_l	0	$\frac{(T-T_1)}{(T_2-T_1)}$	1
$T_{PC}(T1, T2)[K]$	273.3	-	270

Solidification

Figure5.7 shows the experimental results with different numerical simulations where different flow velocities are considered. From the experimental curve (dotted red), it is observed that pure water supercools (2s) before the start of the phase change from liquid to solid state, that is not replicated by the 1-D model. The numerical results show that assuming a flow velocity of 2,5m/s for the calculation of the heat transfer convection coefficient, it is possible to obtain a good match with the experimental results (blue curve) regarding the first part involving sensible heat (1s-3s excluding the supercooling effect) and the second part involving the phase change (3s-4s). The difference between experimental and numerical results is relevant in the last part of solidification (4s-5s) leading to an underestimation of the time where the PCM reaches the bath temperature (time of charge). Indeed, assuming in the numerical model a flow velocity of 0,8 m/s (yellow line), the time of charge better matches the one showed by the experimental results. In this case, a reason attributed to the sudden change of temperature in the final part of solidification (4s-5s), has also been discussed by Bourdillon [77], and can be noticed in Figure5.8 where the numerical results at the wall in different positions of the container are showed. Figure5.8 shows that when the central part (purple line) is under phase change, the temperature of the other points (orange and blue line) are decreasing inducing at end of phase change a sudden temperature fall in the center of the container part of the work.

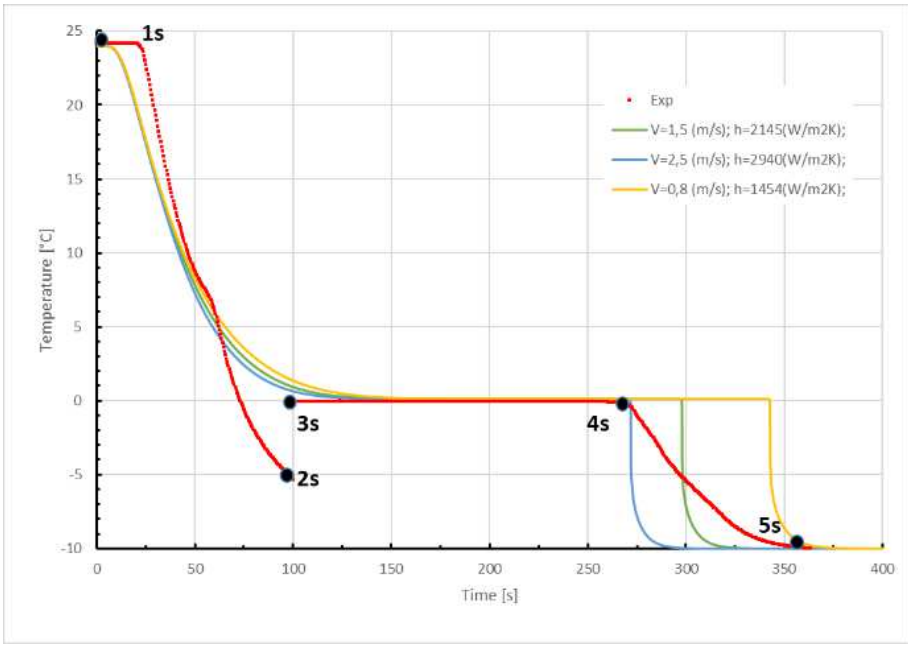

Figure 5.7.: Experimental and numerical results of solidification of DI water

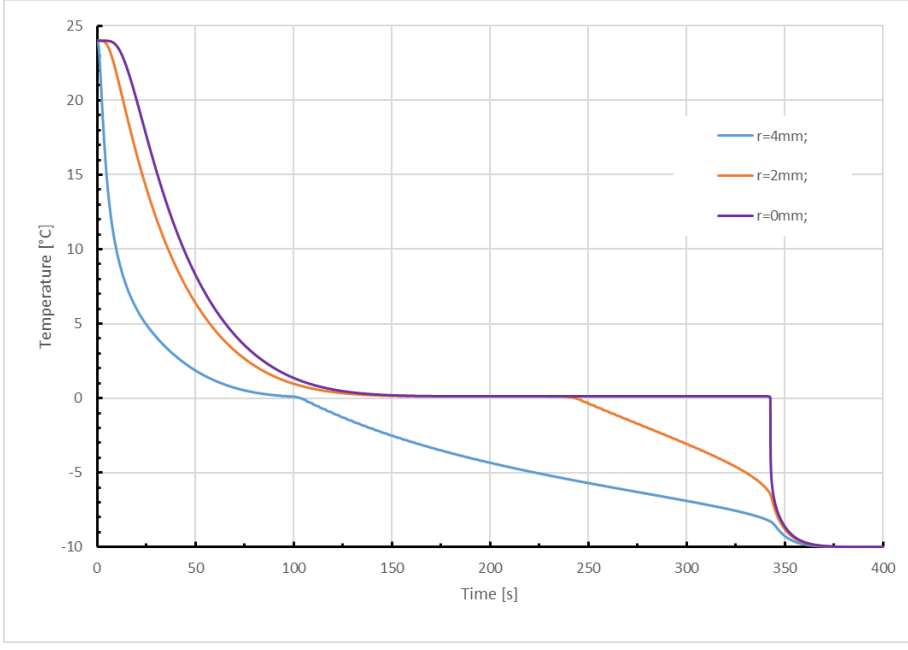

Figure 5.8.: Numerical simulations of DI water in different positions

Melting

Figure5.9reports the experimental results of the melting and the numerical simulation obtained with the 1-D model. A free convection coefficient of 290$[W/m^2K]$ has been estimated from eq.4.16 optimizing the value of the two constants A and B (A=0.32, B=0.25). The melting process (shows that the part of the experimental curve involving the sensible heat (1m-2m;3m-4m) and the phase change (2m-3m) has a similar trend comparing the numerical results (blue curve) with a good match in the final time of discharge (3m).

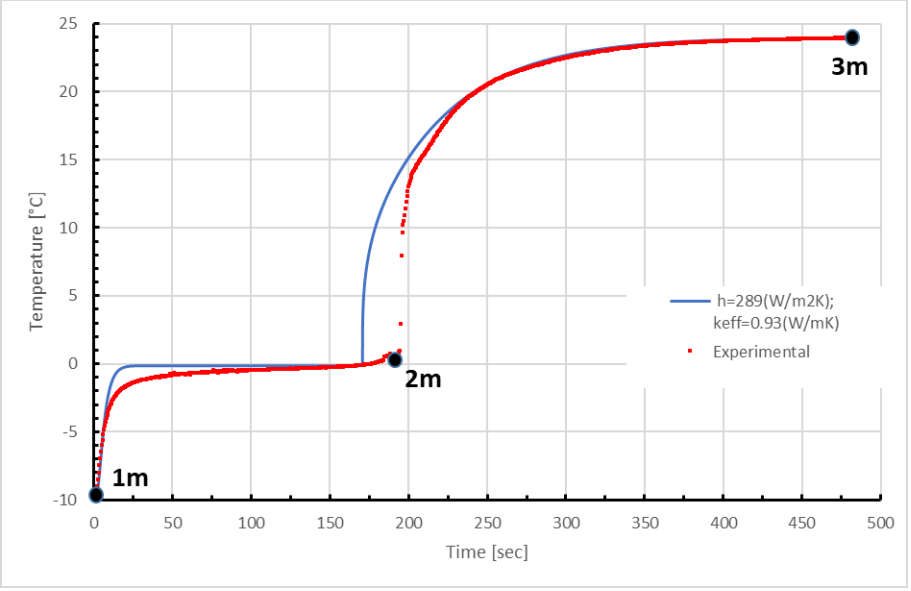

Figure 5.9.: Experimental and numerical results of melting of DI water

5.3. Validation and test of the methodology

5.3.1. Validation with pure DI water

The 1-D numerical model with the boundary conditions calibrated for the current set-up has been validated comparing the numerical results and the experimental data in the different position of the container shown in Figure4.10. In this case, the comparison has been done considering both charging and discharging of the same PCM (deionized water) for two different tests (Test 1 and Test 2).

Results

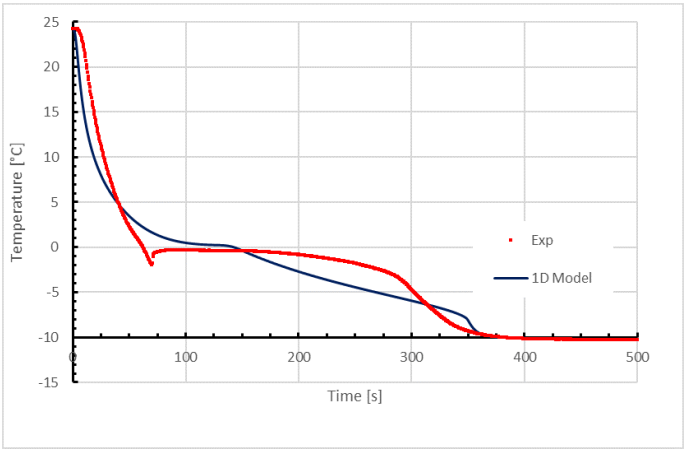

(a) *Test 1*

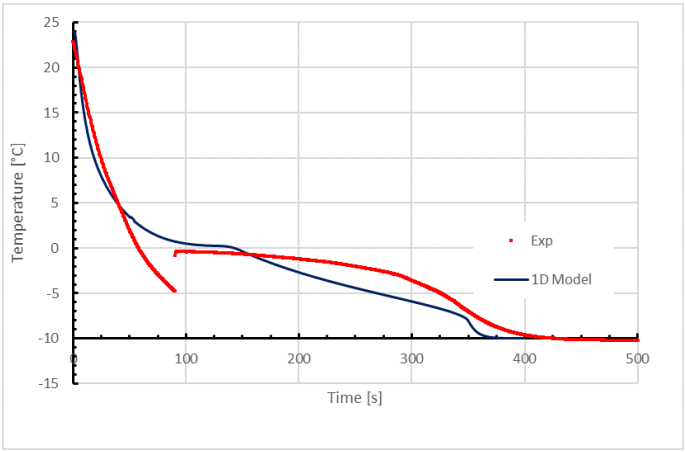

(b) *Test 2*

Figure 5.10.: Experimental and numerical results for the charging-solidification of DI water in position A

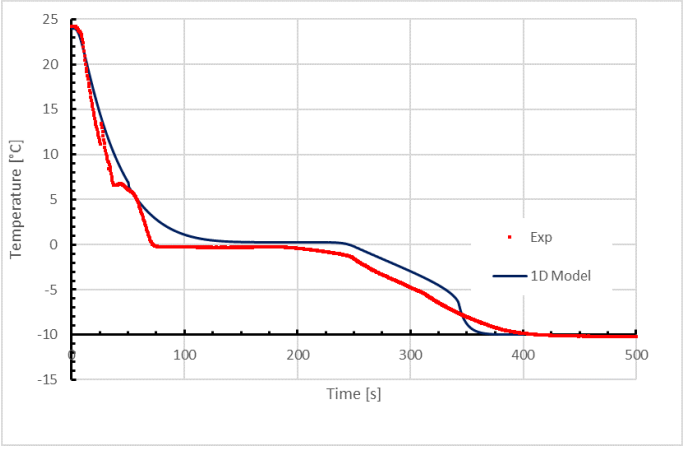

(a) *Test 1*

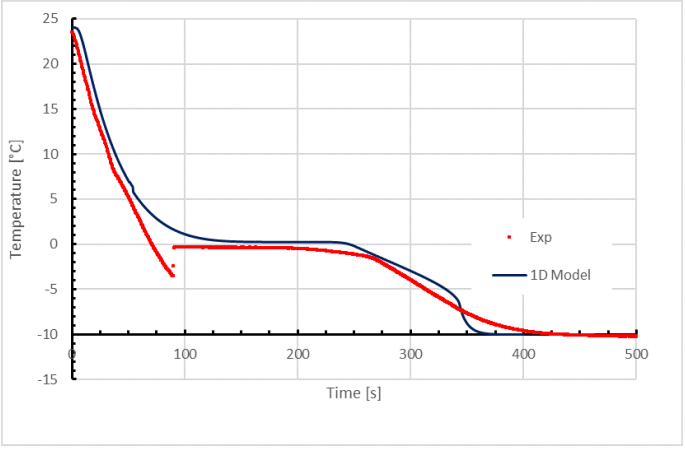

(b) *Test 2*

Figure 5.11.: Experimental and numerical results for the charging-solidification of DI water in position B

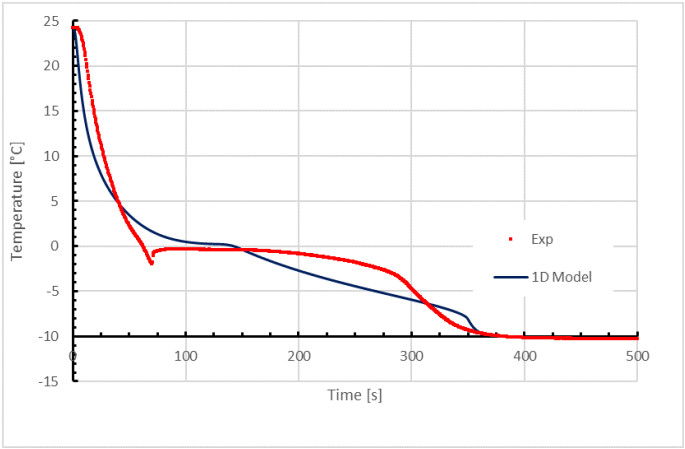

(a) *Test 1*

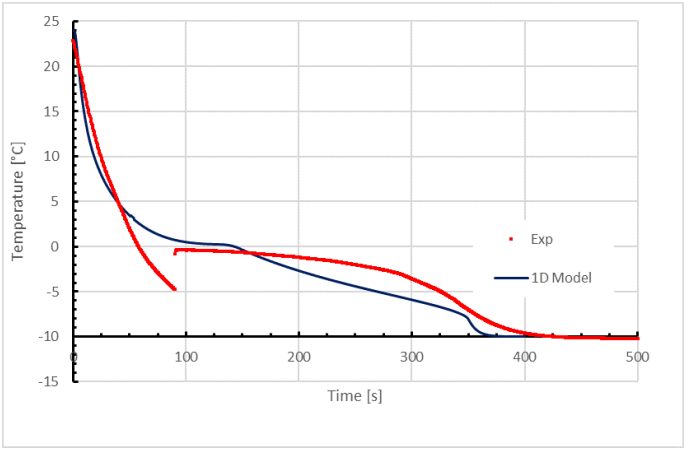

(b) *Test 2*

Figure 5.12.: Experimental and numerical results for the charging-solidification of DI water in position C

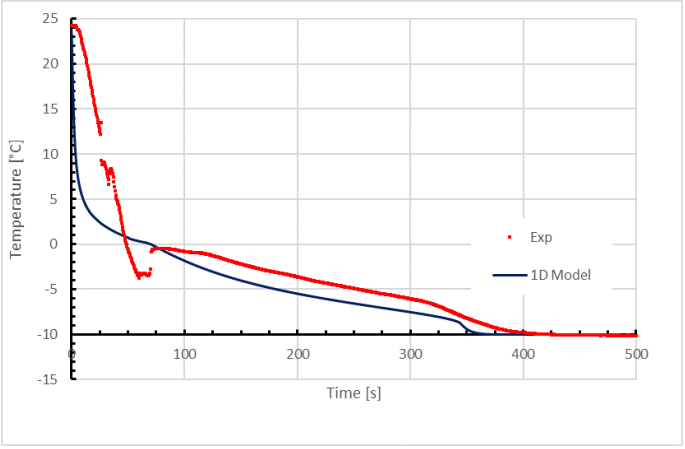

(a) *Test 1*

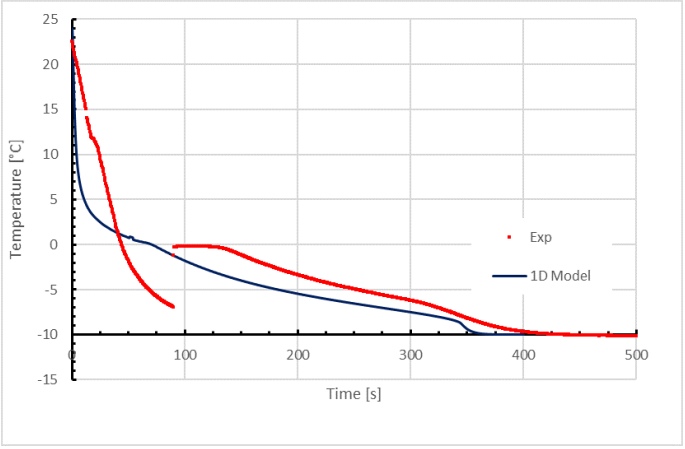

(b) *Test 2*

Figure 5.13.: Experimental and numerical results for the charging-solidification of DI water in position D

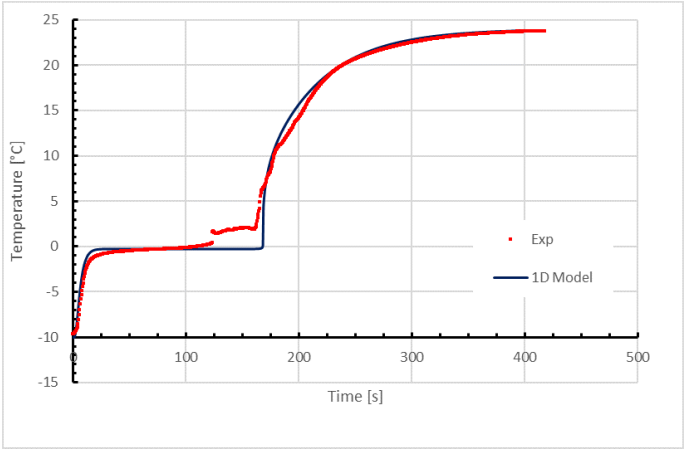

(a) *Test 1*

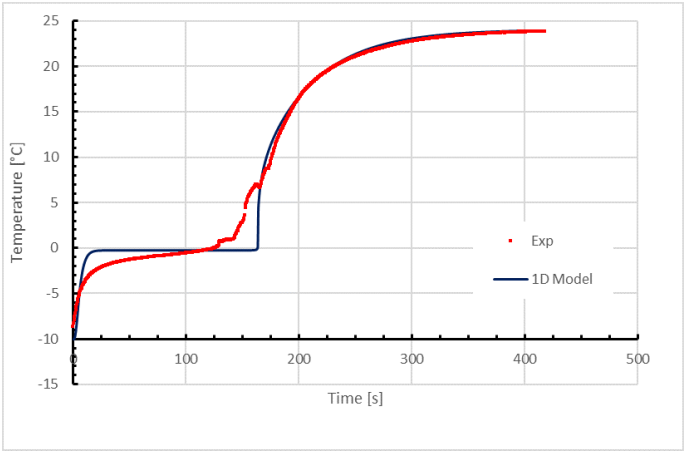

(b) *Test 2*

Figure 5.14.: Experimental and numerical results for the discharging-melting of DI water in position A

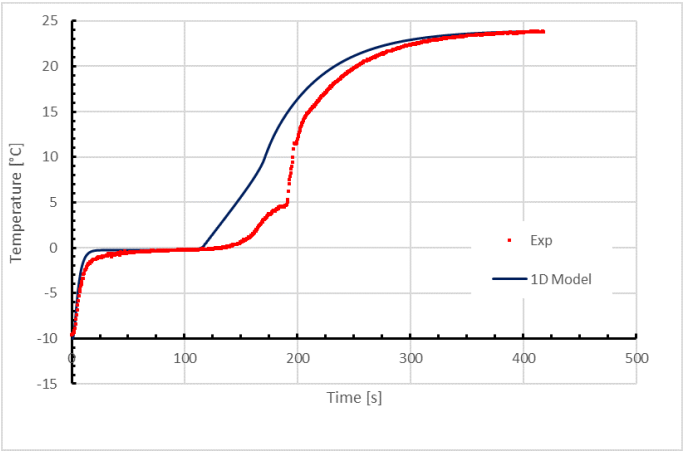

(a) *Test 1*

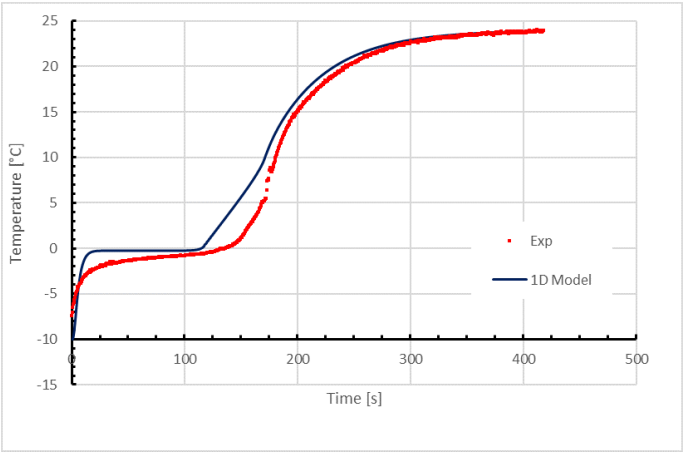

(b) *Test 2*

Figure 5.15.: Experimental and numerical results for the discharging-melting of DI water in position B

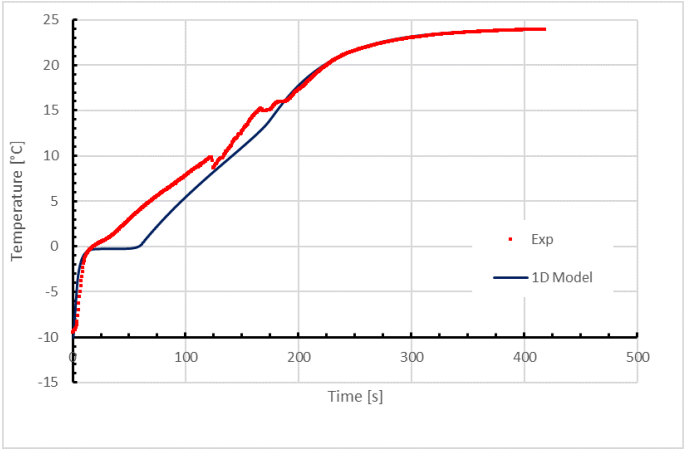

(a) *Test 1*

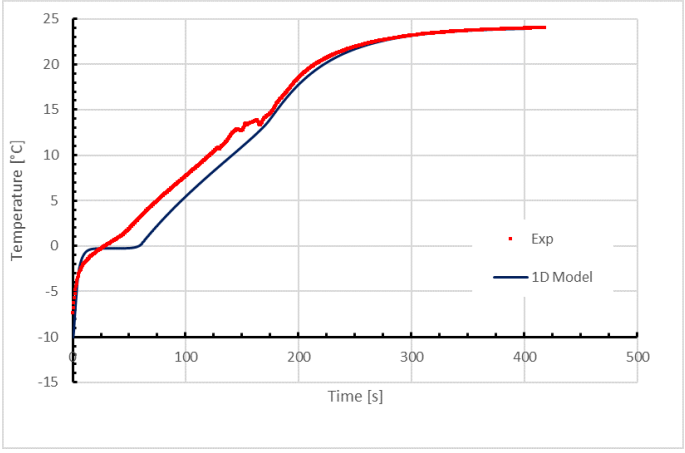

(b) *Test 2*

Figure 5.16.: Experimental and numerical results for the discharging-melting of DI water in position C

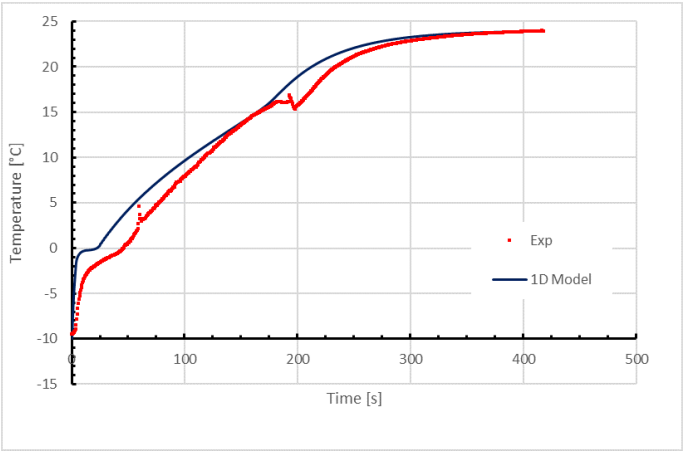

(a) *Test 1*

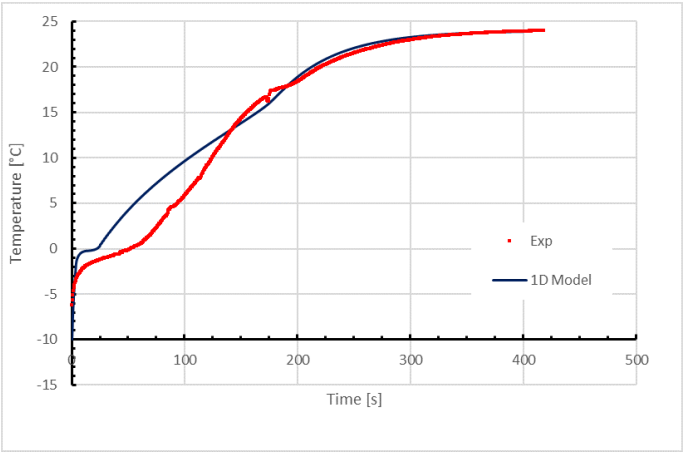

(b) *Test 2*

Figure 5.17.: Experimental and numerical results for the discharging-melting of DI water in position D

Table 5.3.: RMSE value of the 1-D model for discharging-melting of pure DI water

	RMSE	
Position	Test 1	Test 2
Solidification		
A	3.35	2.84
B	1.51	1.61
C	2.16	2.08
D	4.31	3.58
Melting		
A	1.11	1.69
B	3.09	1.82
C	1.68	1.44
D	1.91	2.18

Analysis of results

The two experiments, conducted with the same boundary conditions, results in similar experimental curves that can confirm the repeatability of the experiment. The solidification of the center of the container is showed in Figure 5.10 a where the results are the same reported in the calibration of the model in the section above. The only difference that can be noted in Figure 5.10 is that in Test 2 the time of charge estimated by the model is slightly shorter. Position B showed in Figure 5.11 shows a good match with the experimental data for both the test where the numerical curve and the experimental curve has a similar trend for all the phases of solidification. The solidification of DI water in position C (Figure5.12) shows a good agreement in the first part of solidification involving sensible heat but at the end of the phase change, the numerical curve has a sharper slope compared to the experimental curve ending with a similar time of charge. Position D showed in Figure 5.13, has the largest difference between the numerical results and experimental curve for both the test regarding the first part of the solidification curve with an earlier phase change. The last part of the charging showed by the numerical model is similar to the experimental data with the same slope and a lower temperature (2°C less than the experiments). The comparison of the melting curves with the numerical model results in a better match compared with the solidification of deionized water. In this case, the absence of supercooling and the container placed in a static bath offers better conditions that can be replied with a simplified 1-D model. In particular, the numerical results in position A and B (Figure 5.14 and Figure 5.15) reproduce in a similar way the experimental curves of the discharging of the PCM. A good match is also shown in the curves closer to the wall where the comparison for both the tests are shown in Figure 5.16 and Figure 5.17. Table5.3 reports the error evaluated by the RMSE value. In general, the higher error is in solidification of position D where the numerical model has a different behavior regarding the first part involving the senile heat. with a maximum RMSE in Test 1. Comparing the charging and discharging the RMSE value is lower in the case of melting where the curves have a better match compared to the experimental data. Although the conditions of supercooling cannot be replied with the numerical model, the numerical model can provide a good estimation of the thermal behavior in both the charging and discharging of the PCM and in this first step of the methodology can be considered validated.

5.3.2. Test on Aqueous EG

The 1-D numerical model calibrated and validated with DI water has been further tested with aqueous ethylene glycol with a 30% of the concentration in DI water. The thermal properties of the PCM that serve as the input for the 1-D model refer to the measurement presented in section and are resumed in Table 5.4. The effect of the convection during the melting has been taken into account introducing an effective thermal conductivity k_{eff} where it's value has been calculated increasing the value of the liquid thermal conductivity of 75% as assumed for the DI water. The boundary conditions assumed for the simulation are based on the calibration done with DI water. In particular, the heat transfer convection coefficient for the melting, calculated with eq.4.16, is based on the two parameters A and B calibrated in the previous section and the heat transfer convection coefficient for the solidification (eq. 4.15) is based on the velocity of 0.8 m/s. For the calculation of the Ra and Re numbers, the properties of the thermal bath, reported in Table5.4, refers to the temperatures reported in Table4.3.

Table 5.4.: properties for Aqueous Ethylene Glycol (30%) used for the 1-D numerical model

PCM Properties	Liquid $>T_2$	Phase Change	Solid $< T_1$
$\rho[kg/m3]$	1027	$\rho_{PC} = (1 - f_l)\rho_s + f_l\rho_l$	1027
$c[kJ/KgK]$	3.815	$c_{PC} = (1 - f_l)c_s + f_l c_l$	3.23
$k[W/mK]$	0.475 ($keff$= 0.831)	$k_{PC} = (1 - f_l)k_s + f_l k_l$	0.647
$L[kJ/kg]$	-	93.3	-
f_l	0	$\frac{(T-T_1)}{(T_2-T_1)}$	1
$T_{PC}(T1, T2)[K]$	257.8	-	258.8

Results

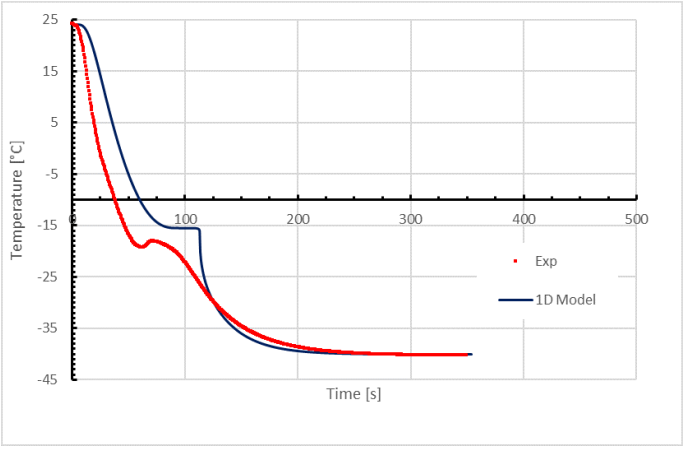

(a) *Test 1*

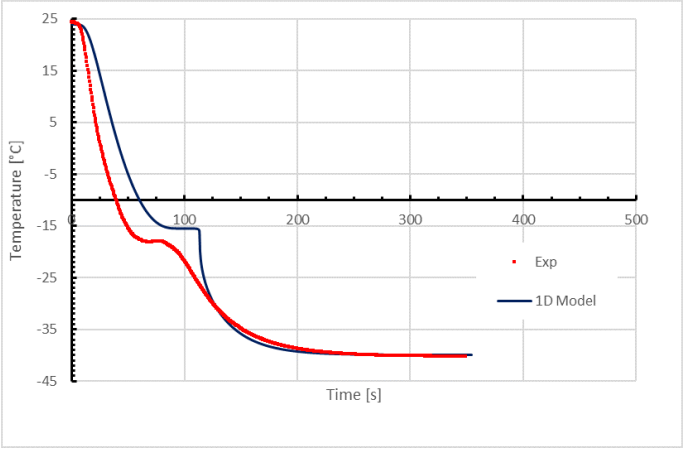

(b) *Test 2*

Figure 5.18.: Experimental and numerical results for the charging-solidification of EG30 in position A

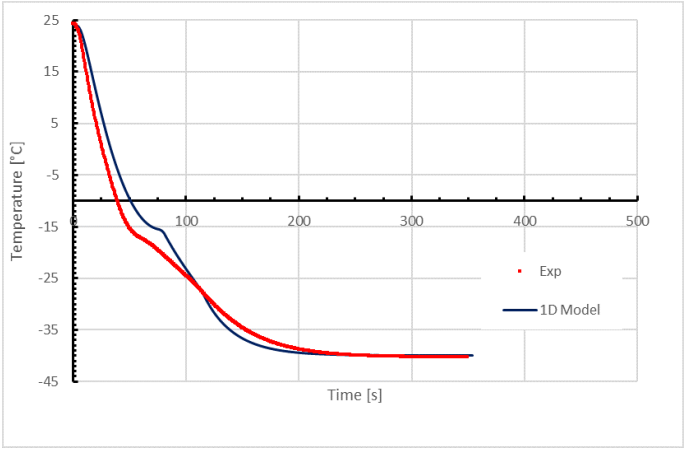

(a) *Test 1*

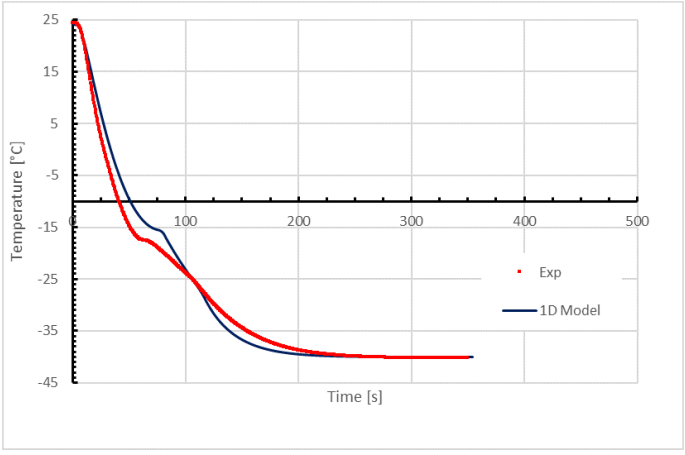

(b) *Test 2*

Figure 5.19.: Experimental and numerical results for the charging-solidification of EG30 in position B

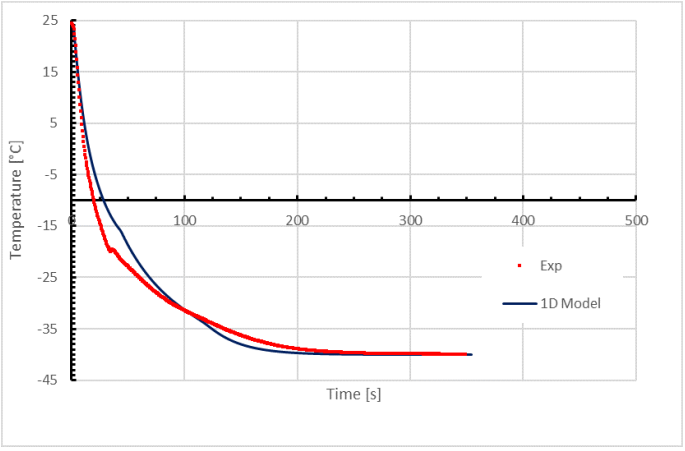

(a) *Test 1*

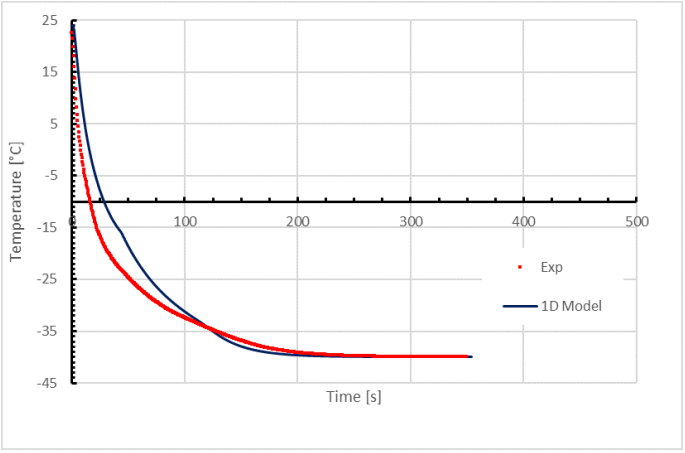

(b) *Test 2*

Figure 5.20.: Experimental and numerical results for the charging-solidification of EG30 in position C

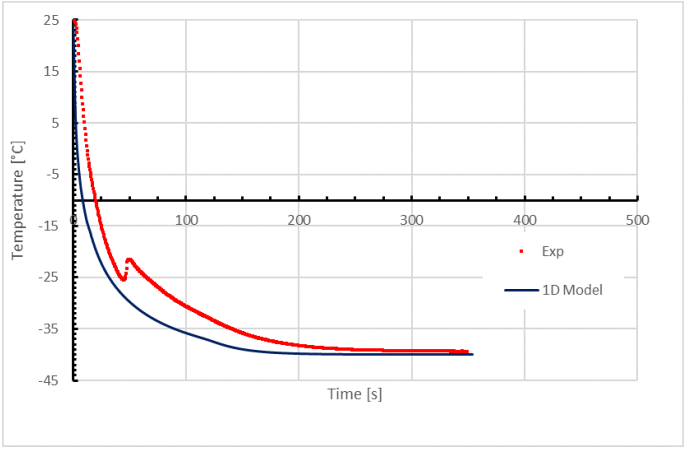

(a) *Test 1*

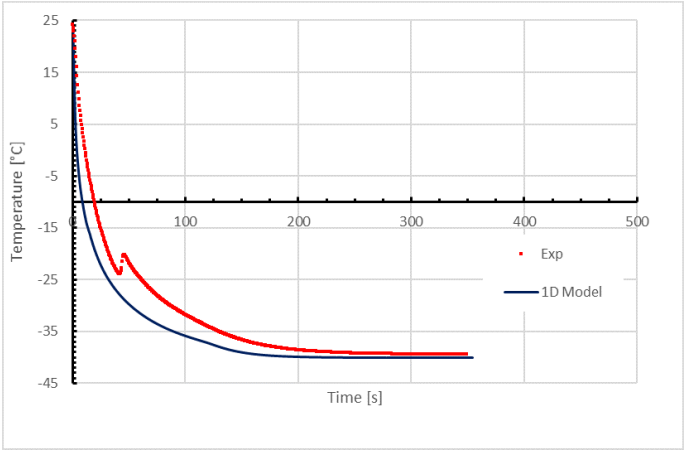

(b) *Test 2*

Figure 5.21.: Experimental and numerical results for the charging-solidification of EG30 in position D

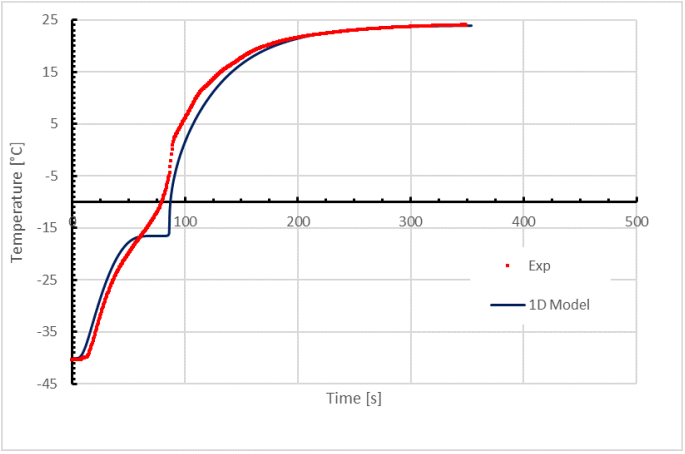

(a) *Test 1*

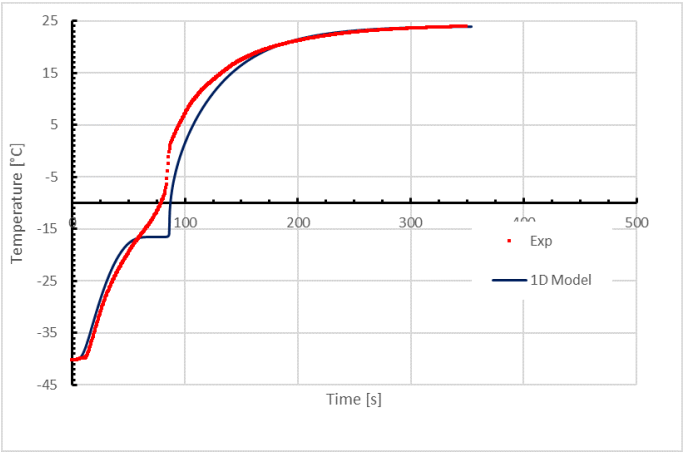

(b) *Test 2*

Figure 5.22.: Experimental and numerical results for the discharging-melting of EG30 in position A

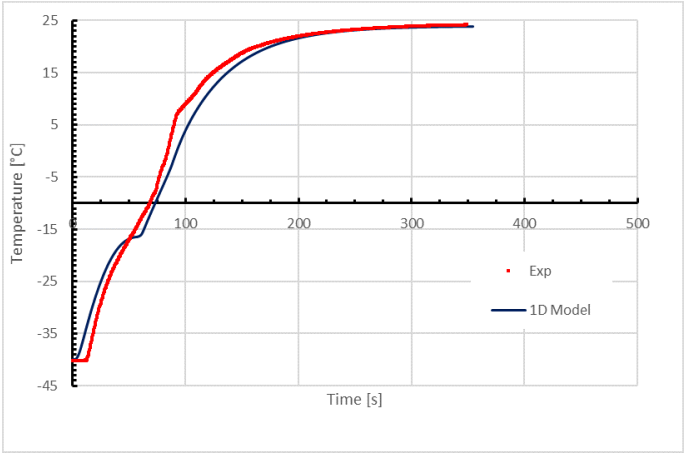

(a) *Test 1*

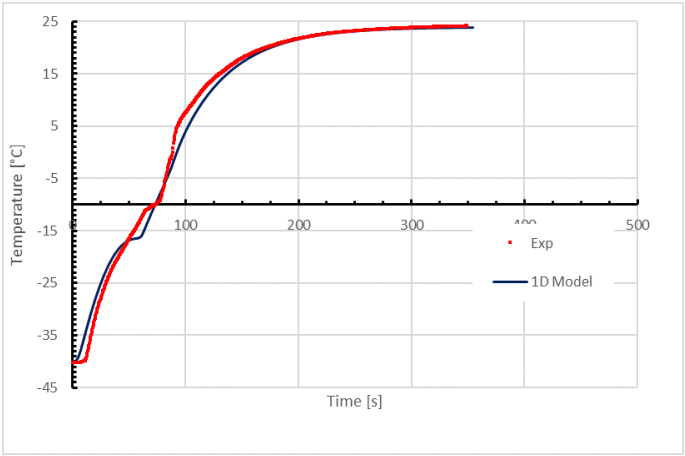

(b) *Test 2*

Figure 5.23.: Experimental and numerical results for the discharging-melting of EG30 in position B

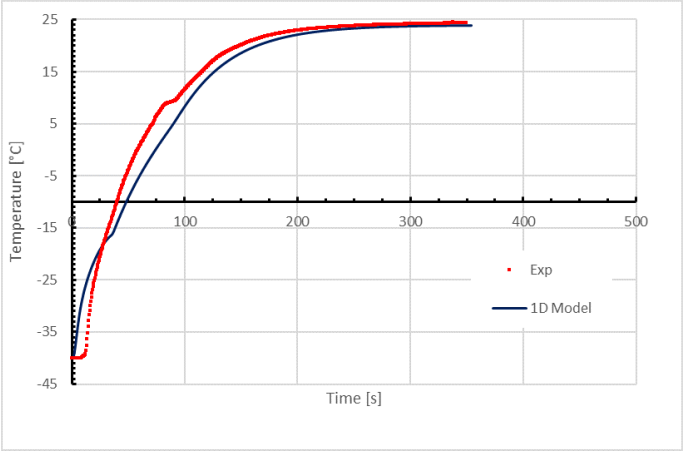

(a) *Test 1*

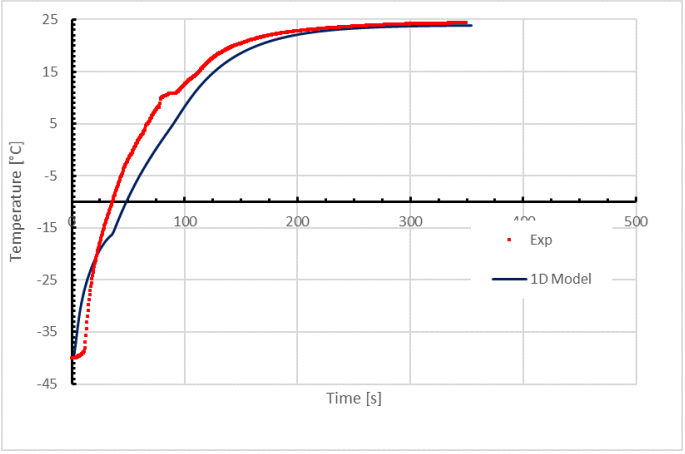

(b) *Test 2*

Figure 5.24.: Experimental and numerical results for the discharging-melting of EG30 in position C

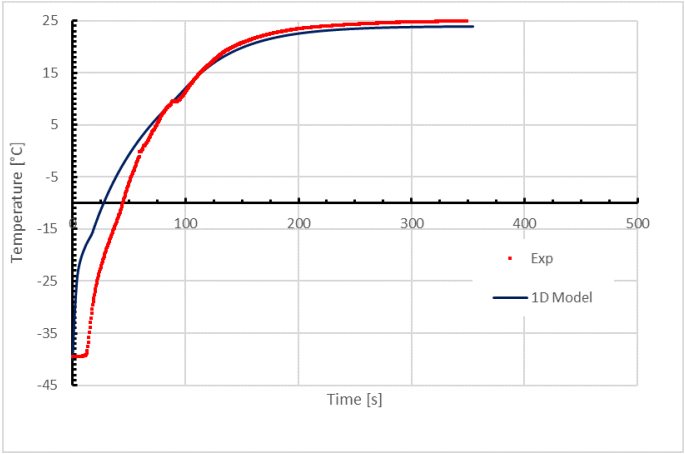

(a) *Test 1*

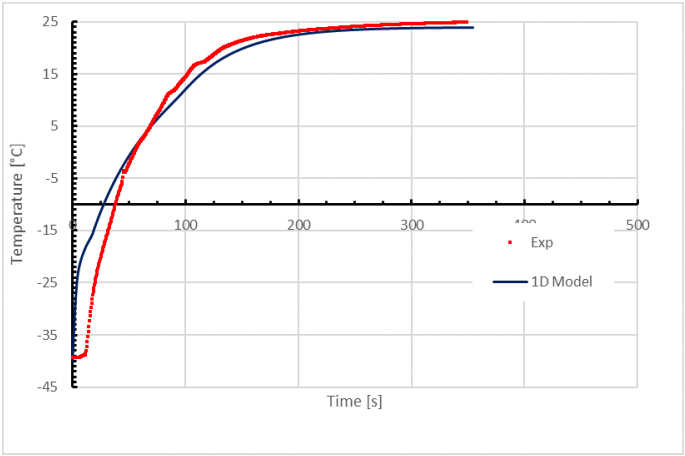

(b) *Test 2*

Figure 5.25.: Experimental and numerical results for the discharging-melting of EG30 in position D

Table 5.5.: RMSE value of the 1-D model for discharging-melting of EG30

	RMSE	
Position	Test 1	Test 2
Solidification		
A	5.37	4.71
B	2.54	2.09
C	2.29	3.48
D	5.30	4.45
Melting		
A	2.48	2.77
B	2.34	1.59
C	3.17	3.64
D	4.97	4.31

Analysis of results

As for pure DI water, also, in this case, the numerical model has been compared with two different test with aqueous EG30 with the same boundary conditions. With regards, the comparison with the experimental results, Figure 5.18 shows the solidification of the PCM in the position A corresponding to the center of the container. The results show that the curve of numerical model cools down slower than the experimental results. Furthermore, the phase change occurs at a higher temperature than the experimental one but, at the end of phase change, the simulation curve is able to match the final time of charge with a similar behavior of the experimental one. The first reason of discrepancy can be attributed to tolerance of the thermocouple position that can slightly change the results. Indeed, in the case of Test 2, the solidification curve is much closer to the simulations. Regarding the phase change temperature, in the model has been assumed a phase change temperature of -16°C as showed from the DSC results, but, as discussed above, the slow crystallization of the PCM allows to a lower phase change temperature that can be common with a 'kinetic controlled' phase change [74]. Regarding the position closer to the container wall, the higher difference between the experimental results and the simulation is showed in position D showed in Figure 5.21, while the position C (Figure5.20) shows a good agreement between the experimental results and numerical simulations with both the test. With regards to the melting, also, in this case, the numerical simulations obtained with the 1-D model results in a better match with the experimental results. In general, the simulation curves on the central positions A and B showed in Figure5.22 and Figure5.23 respectively shows a good match with the experimental results. The only difference can be denoted by the plateau showed by the numerical model that cannot be appreciated in the experimental data due to the small size of the container and the consequently high rate of heat transfer. However, the time of charge and the shapes of the curves are similar to the real behavior of the PCM. A slight difference between model and experiments can be noted in position D showed in Figure5.25, and can be considered as a further confirmation of the thermocouple position due to the small tolerance related to the container dimensions. Indeed, a better match between the two curves is showed figure where the results are compared in position C 5.24. The error between the numerical model and the experimental data has been calculated with the RMSE values reported in Table5.5. The biggest discrepancy is showed in position A of Test 1 (Figure5.18) due to the supercooling showed from the experimental curve before the phase change of the PCM. Furthermore, a high RMSE value can be noticed in all the curves in position D. This and can be considered a critical position for the thermocouple position due to the small tolerance related to the container dimensions. Indeed the curve in position D that has a

similar behavior with the position C. The results of the RMSE shows that EG30 has a larger error between numerical model and experimental data compared to DI water. Indeed, the slower crystallization and the lower latent heat of fusion of the EG30 results in a more difficult prediction of the PCM behavior. Furthermore in a mixture is more difficult to characterize the material during the phase change due to the change of composition that may affect the melt temperature. In general, the numerical results obtained with a simple 1-D model shows a good agreement with the experimental curves resulting in a useful tool for the first prediction of a low temperature PCM thermal behavior.

5.4. Discussion and main findings

The design of the High Grade Cold Storage represents an important task to improve the performance of the waste cold recovery and increase the efficiency of a microgrid scale LAES. The actual solutions of LAES HGCS are based on a sensible heat energy storage with a packed bed configuration. The integration of phase change material can help to improve the energy density and stabilize the thermal fluctuations during the storage process. The design of an HGCS involving both sensible and latent heat includes different steps as PCM selection and formulation, thermal characterization of PCM and the model and the test of a pilot scale HGCS. This chapter presents a methodology for the thermal characterization of low temperature phase change materials that can be integrated into an HGCS for microgrid scale LAES applications. An experimental rig has been developed to test and measure the thermal behavior of low temperature PCM. In particular, a PCM container has been designed to replicate a similar behavior of one-dimensional heat transfer. The experimental data obtained in different positions of the container have been used to validate a simple 1-D numerical model based on heat capacity method and solved by MATLAB software. Due to the well-known properties, the methodology has been validated with the results obtained from two different test that involves the charging and discharging of DI water as PCM. The experimental data have been used to calibrate the boundary conditions of the 1-D numerical model and validate the results from the 1-D model. The comparison between the experiment and the simulation and experiments shows a good agreement. The error, calculated by means of the RMSE value is higher in the simulation of the solidification due to the supercooling of the water before the phase change that does not take into account in the model. Furthermore, the point corresponding on the container wall is the critical point to replicate with numerical simulations. The methodology validated with DI water has been further tested using a different PCM. Due to the low corrosivity and low cost, aqueous alcohol has been used as a PCM for the test. In particular, an aqueous solution of DI water

and 30% ethylene glycol (EG30) has been used. Differential scanning calorimeter and laser flash analyzer have been used to measure the thermal properties of the aqueous EG showing a phase change temperature of -16°C. The experimental curves obtained from the solidification and the melting of the PCM inside the container are then compared with the results from the numerical model. The results show a good agreement with the experimental data. The RMSE value is higher for the solidification due to the slow crystallization of the PCM that results in a phase change temperature lower than the one showed from the DSC results. With a final remark, the methodology presented in this work can be applied to evaluate and characterize low temperature PCM (until -90°C). Furthermore, the 1-D method represents a valid and simple method to approximate and predict the thermal behavior of low temperature PCM and can a useful tool to compare the charging and discharging profiles of different materials that are necessary for the choice of a proper PCM. Furthermore, the simplicity of the code allows the numerical model to be integrated into a more complex numerical model, that result interesting for the complete modeling of HGCS.

Chapter 6.

Conclusions and suggestions for future works

In this chapter, the summary of the conclusions of this thesis is reported. In the second section suggestions for future works are given.

6.1. Summary of main conclusions

Preliminary study on a microgrid scale LAES air liquefaction plant When scaling down the LAES, the high specific consumption of the liquefaction cycle mainly affects the final value of the roundtrip efficiency of the system. Chapter 2 aims to investigate the liquefaction plant configuration that minimizes the specific consumption of a microgrid scale LAES. In particular different liquefaction cycles, suitable for the small-scale LAES, are analyzed and compared by mean of simulation software and an optimal configuration that minimizes the specific consumption is proposed. The cycles are modeled with the software Aspen HYSYS and simulations are conducted by changing the operating conditions such as pressure and recirculation fraction. The liquefaction plant considered for a microgrid scale is supposed to produce 10 tons/day hypothesizing a LAES charging process of 12 hours. The main results of the chapter can be resumed as:

- Claude and Kapitza cycles have the lowest specific consumption and; with the two-stage compression, it is possible to increase the performance by 25%. However, the third low temperature heat exchanger of the Claude cycle results to be inefficient and the Kapitza cycle results to be a better option.

- The heat exchangers result to have the highest impact on the cycle performance. The pressurization of the phase separator/liquid air tank is shown to positively affect the performance, reducing the specific consumption by 21% with a phase separator pressure higher than 4 bar.

Moreover, the combined effect of both pressurized phase separator and increased operating pressure can reduce the specific consumption below 500 kWh/t.

- the exergy analysis shows that the thermal power wasted by intercooling is detrimental to exergy efficiency of the cycle and that also the cryoturbine results to be a critical component.

- A conservative final optimal configuration of an air liquefier can be considered a two-stage compression Kapitza cycle with an operating pressure in the range of 38-45 bar and a phase separator pressure of 6-8 bar. This range of operating conditions achieves a specific consumption range of 520-560 kWh/t that is an interesting figure for LAES application in microgrids.

- The integration of a 105.5 kW single-effect water-Lithium Bromide absorption chiller with the microgrid scale liquefier, gives a reduction of the specific consumption of around 10% (537 kWh/t to 478 kWh/t) and an increase of exergy efficiency of around 11.5%.

Parametric performance maps for microgrid scale LAES Chapter 3 presents a complete configuration of microgrid LAES adding to the liquefaction plant presented in Chapter2, the discharge section and the waste heat and cold thermal energy recovery. The microgrid LAES presented has been modeled by means of the simulation software Aspen HYSYS and a sensitivity analysis has been carried out to investigate the effect of the main operative parameter on the system performances in a wide range of operating conditions, where the main findings can be resumed as:

- a novel approach has been proposed with the introduction of performance maps that can be particularly useful to assist the preliminary design of a microgrid scale LAES. The main advantage of the maps is the simple and immediate method that can be applied by engineers and researcher to estimate the LAES performance and optimize the design in terms of term of specific consumption, specific electric power output and round-trip efficiency.

- The first map allows estimating the specific consumption of the microgrid scale LAES that corresponds to the value obtained with the optimal recirculation fraction reported in the map. The two main operative parameters considered in this chart are the charging pressure of the LAES and the efficiency of the High Grade Cold Storage. The High Grade Cold Storage provides, by means of a heat transfer fluid, the cold flow that is

used to assist the liquefaction cycle. The map shows that for a high value of the HGCS efficiency, the charge pressure has not a relevant effect on the specific consumption. Therefore, the design of the cold storage is crucial to minimize the specific consumption and optimize the performance of the entire system.

- The second map reports the TIT (Turbine Inlet Temperature) of the discharge cycle according to the charging pressure and the efficiency of the HGWS. The map clearly shows that increasing the pressure of the liquefaction cycle is it possible to obtain higher TIT with a lower HGWS efficiency.

- The effect of the TIT on the specific electric power output (SP) produced from the discharge side of the LAES is showed the third map for different discharge pressures of the cryogenic pump. In this third map is possible to obtain, for a fixed amount of liquid air (1 t/h), a higher electric power from the discharge side with high TIT and high discharge pressures.

- The round-trip efficiency of the microgrid can be evaluated in the last fourth performance map that includes the value of the specific consumption and the specific power output.

- Two application example are reported to show the use of the four performance maps. In particular, the graphical approach is an immediate way to estimate the microgrid scale LAES performance and evaluate the impact of the main operative parameters during the system design.

- The methodology can be extended scaled up for large-scale systems and be applied as a systematic tool for different LAES operating conditions configurations (full electric and cogenerative/trigenerative).

Microgrid scale LAES High Grade Cold Storage: Thermal characterization of Phase Change Materials The waste cold recovery cycle is fundamental to improve the performance the microgrid LAES. In particular, a proper design of HGCS allows to decrease the specific consumption of the liquefaction cycle and increasing the overall roundtrip efficiency of the system. The High Grade Cold Storage (HGCS) allows storing the high grade cold thermal energy in a storage medium that can be used in the liquefaction plant in a later time. On the design of the High Grade Cold Storage (HGCS) for a microgrid scale LAES, the following parameters should be taken into account:

- Proper storage temperature

- High Energy Density and Reduced Dimensions

- High Charge and Discharge Efficiency
- Good Cycle stability
- Low cost

A High Grade Cold Storage can store cold thermal energy by means of sensible heat, latent heat (Thermochemical energy storages are not currently available to store high grade cold). The current solutions of HGCS are based on a sensible heat storage system requiring large volumes to store small amounts of energy. The Highview pilot plant based in Birmingham studied from different researchers, uses quartzite rocks a packed bed configuration involving, in the cold energy storage process, only sensible heat. However, in a microgrid context is always convenient to reduce the space of the entire grid, control, and storage systems. Therefore, a storage with high energy density is particularly important to reduce the dimension of the entire system. The idea of this work is then to integrate one or more part of latent heat storage materials (PCM) in the actual solution adopted for HGCS resulting in a hybrid HGCS solution. The main objective is to reduce the dimensions of the HGCS increasing the energy density.

The design of a hybrid HGCS is part of a project based at TESLAB@NTU in the Nanyang Technological University of Singapore. The design consist of three main steps that can be assumed as follow:

- PCM selection and Formulation
- Thermal Response and Thermal characterization of PCM
- Modelling and Develop an HGCS prototype

This work focuses on the thermal response and thermal characterization of PCM. In particular, a methodology has been developed to measure the thermal response and predict the thermal behavior of low temperature phase change materials that can be applied to assist the design of a hybrid HGCS. The main conclusions of chapter 4 can be summarized as follow:

- An experimental rig has been designed to measure the thermal response of subzero PCM. The set-up consists of a PCM container to be placed alternately between a cold ethanol bath (solidification) and a hot water bath (melting) maintained at a constant temperature. The temperatures of the PCM in different positions of the container are recorded with four k-type thermocouples. The PCM container has been designed to obtain a similar thermal behavior of the PCM involving a one-dimensional heat

transfer process. In order to obtain a successful validation of the 1-D numerical model, the PCM container has been designed to obtain a similar thermal behavior of the PCM involving a one-dimensional heat transfer process.

- The experimental rig presented in this work can be applied to and characterize low temperature PCM until -90°C.
- In this work, the results of two materials has been presented to establish the thermal characterization methodology. Deionized water has been first selected due to the well known thermal behavior that can be used to test the reliability of the experimental results and first validation of the methodology. As a second material, an alcohol aqueous solution has been selected due to the low corrosivity, good cycle stability, and low cost. In particular, a solution with a concentration of 30% of ethylene glycol (EG30) by weight in deionized water has been selected as PCM.
- Differential scanning calorimetry with refrigerated coolant system was used to measure the phase transition temperatures and heat capacities of the EG30 and the thermal diffusivities was measured by means of Laser flash analyzer. The results of DSC show that for the material selected a heat flow peak is reached at a temperature of -16°C with a latent heat of 93.3 KJ/kg. An average thermal conductivity of 0.48 W/m2K and 0.42 W/m2K are founded for the solid phase and the liquid phase respectively.
- The reliability of the results has been verified with two different tests evaluating the solidification and the melting in different positions of the container.
  - In the charging/solidification process of DI water, a higher supercooling degree can be noticed in the close to the wall of the container where the rate of cooling is higher compared to the other positions. In the central position, the experimental curves of Test 2 have a slightly longer time of charge (around 10 sec) and a higher supercooling. The other curves in other positions have the same time of charge and a similar trend for both the tests. However due to the complexity of the crystallization process is not easy to ensure a complete repeatability of the tests. Furthermore, the small dimension of the container and the narrow position of the four thermocouples increase the sensibility of the boundary conditions that can affect the repeatability.
  - in the case of discharge-melting of DI water, the curves showed for Test 1 and Test 2 are similar, with the same time of discharge for all the container positions.

  - In the charge-solidification and discharge-melting of EG30 the behavior of the PCM is similar in both the tests. The results show a short phase change phase that is clear just in the center of the container. This is mainly due to the low latent heat of the PCM and the high rate of cooling due to the temperature difference between the cold thermal bath (-40°C) and the warm thermal bath (24°C).
  - During the solidification of EG30 the plateau of the phase change occurs at a lower temperature than the phase change temperature founded from the DSC measurements. These phenomena are common when PCM is characterized by a low rate of crystal growth that results to have a dominant influence on the thermal behavior.

- The 1-D numerical model has been calibrated setting the coefficient included in the calculation of the boundary condition. In particular in the solidification, the PCM it is subjected to a fluid motion due to the refrigerated circulator that leads to assuming the boundary condition for the model as a forced convection. In the melting of the PCM, the convection heat transfer coefficient can be calculated considering free convection outside the container.

- In the test of the 1-D model with pure DI water, the comparison between the experiment and the simulation and experiments shows a good agreement. The error, calculated by means of the RMSE value is higher in the simulation of the solidification due to the supercooling of the water before the phase change that is not taken into account in the model.

- The point corresponding on the container wall is the critical point to replicate with numerical simulations.

- The results of the 1-D model shows a good agreement with the experimental data also in the case of EG30. The RMSE value is higher for the solidification due to the slow crystallization of the PCM that results in a phase change temperature lower than the one showed from the DSC results.

- The 1-D model represents a valid and simple method to approximate and predict the thermal behavior of low temperature PCM and can a useful tool to compare the charging and discharging profiles of different materials that are necessary for the choice of a proper PCM. Furthermore, the simplicity of the code allows the numerical model to be integrated in a more complex numerical model, that result interesting for the complete modeling of HGCS.

6.2. Future works

Although in this work different aspect of a microgrid scale LAES has been investigated, some potential future works are suggested.

Plant optimization

- Discharge optimization - The first part of this work focuses on the optimization of the liquefaction plant to minimize the specific consumption of the microgrid scale LAES. Although in those systems the charge section is the most critical part, the efficiency of the other sections, also affect the final performance of the system. In a microgrid scale LAES, the discharge section can be optimized in order to exploit the maximum energy available from the cryogenics. Some studies have already carried out for large-scale systems, such as the hybrid solutions presented in chapter 1, and in the best of the knowledge, there are no present studies related to a small-scale system.

- Dynamic analysis - The simulations carried out in Chapter 1 and Chapter 2 are based on the assumption of the system modeled in steady state conditions. However, it would be interesting to evaluate the dynamic behavior of the system that is particularly important to optimize the size of the system and evaluate the impact of the start-up phase in the performance when the microgrid LAES is coupled to the grid.

- Alternative waste heat and waste cold recovery solutions - In Chapter 2 a solution to recover the waste heat released during the compression has been proposed introducing a LiBr-water absorption chiller to reduce the specific consumption of the microgrid LAES liquefaction plant. Actually, that could be a large number of ways to recover the waste heat (and waste cold) thermal energy that lead the LAES to be an interesting energy storage to be combined with other energy systems.

- Economic analysis - The evaluation of the cost of the is the main aspect that defines the real feasibility of the system. For small-scale, LAES systems has been estimated a cost per kWh installed much higher than the industrial scale. Actually, the "ripe" state of the technology results in a difficult exact prediction of the real cost. Indeed, the cost of each energy system strictly depends on the state of the technology. Furthermore, the microgrid scale LAES needs to be compared with energy storage that covers the same capacity. Furthermore, an interesting aspect of the LAES that could be economically advantageous can be the possibility to use the storage as a cogeneration and trigeneration system. In this case,

the evaluation of the system and the application to case studies can be an interesting way to further investigate the potential of the system.

Thermal Characterization methodology for High Grade Cold Storage PCM

Methodology improvements In this work, an experimental rig has been presented to measure the thermal response of low temperature PCM. The experimental results obtained with the solidification and melting of pure water has been used to calibrate and validate a simple 1-D model. The model has been then tested on a subzero PCM based on an aqueous glycol solution with a 30% concentration. Although the 1-D model shows a good response and able to approximate the thermal behavior, there are some improvements that can be suggested for future works:

- Inclusion of supercooling - it has been shown that the error between the numerical model and the experimental curves, is greater in the solidification due to the supercooling that occurs before the phase change. The inclusion of the supercooling effect in the 1-D model can be an interesting aspect that can improve the simulation of the PCM thermal behavior and replicate the real response of the material.

- Thermal properties dependent on the temperature - The 1-D model assume that the thermal properties of the material are constant in the liquid and the solid phase. In this case, can be evaluated the difference of model accuracy when the thermal properties dependent from the temperature are taken into account.

- Increase the container dimensions and different bath temperatures - The numerical results highlight the difficulty to catch the phase change plateau during the solidification and the melting of PCM characterized by low latent heat. This aspect can be improved either increasing the container dimensions (radius) or using different bath temperatures. Increasing the container diameter the heat transfer rate at the center is lower increasing the time of charge. In this case, a new container has to be designed and tested to ensure the reliability of the experiment. Considering the second option, acting on the cold bath, the temperature has to be low enough to overcome the supercooling phase of the PCM and the start of the nucleation. Decreasing the warm bath temperature, another refrigerator is necessary to decrease the bath temperature below the ambient temperature.

- Extension of the methodology - The 1-D model validated has been tested with one low temperature PCM. Although the numerical results show a good response, it would be interesting to test the model considering:

- Different Materials
- Different Geometries

Microgrid LAES High Grade Cold Storage

TESLAB@NTU project - The use of the 1-D model can be used to predict the thermal behavior and assist the design of the hybrid HGCS as a part of the project based at TESLAB@NTU. The simple equation discretized in an explicit/implicit form can be easily integrated into the HGCS model to evaluate the behavior of the single PCM module. The different boundary conditions, due to the heat transfer fluid of the storage, has to be validated with a lab-scale prototype planned in the project.

Appendix A.

LAES performance maps

This section provides the four performance maps in full size format and high resolution for the final user.

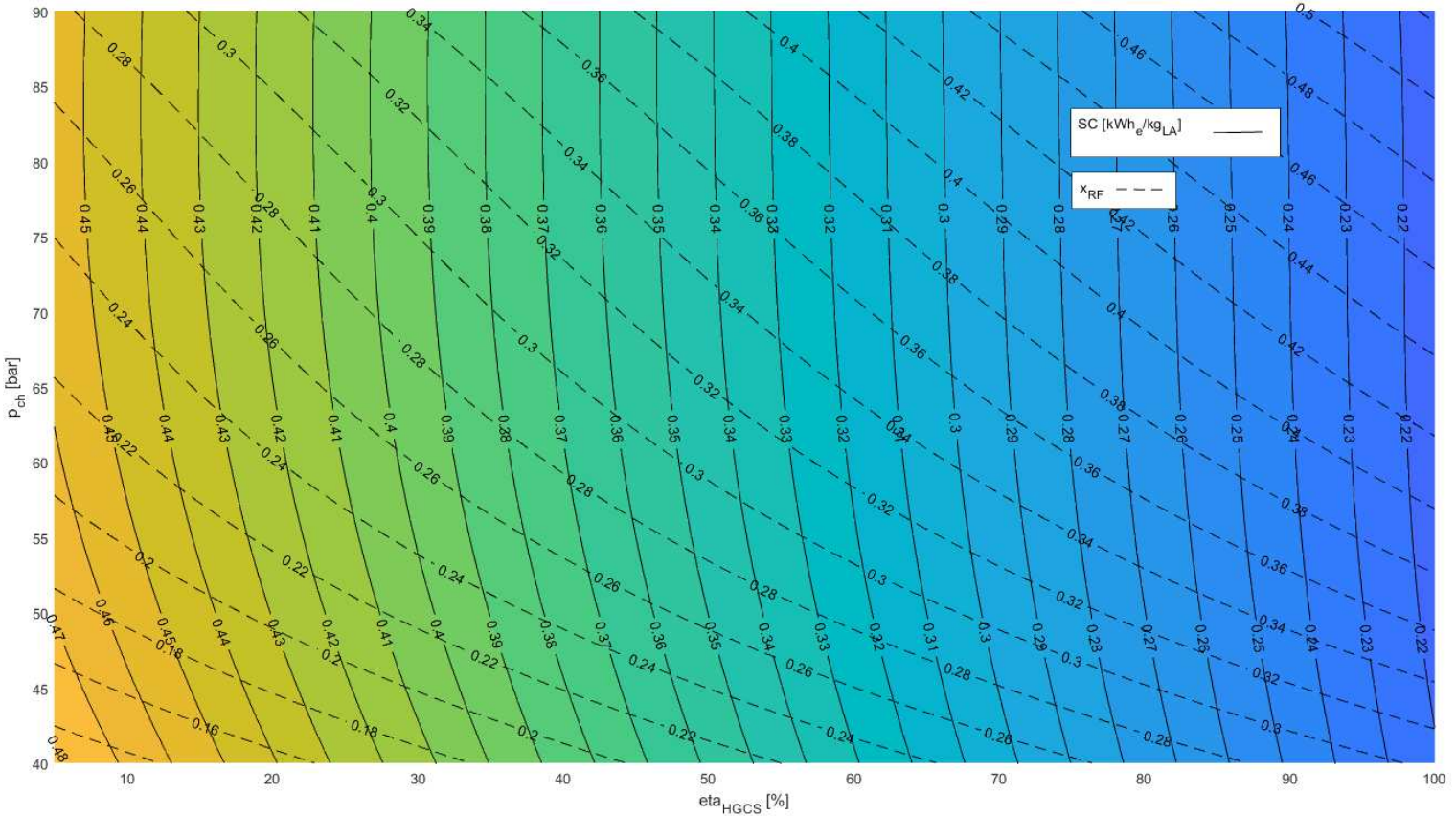

Figure A.1.: Effect of charge pressure and waste cold recovery efficiency on specific consumption for different optimum values of recirculation fraction

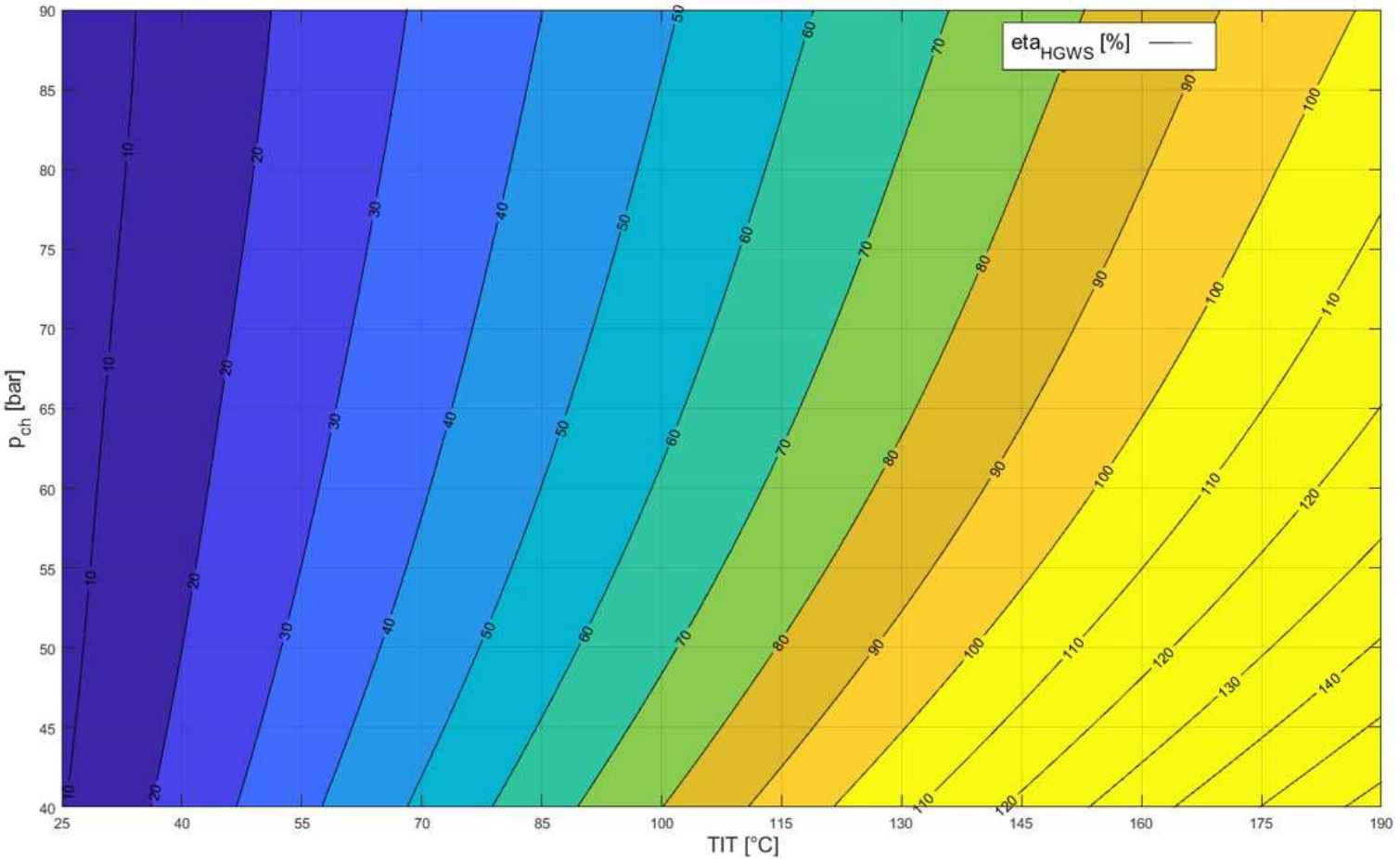

Figure A.2.: Effect of charge pressure and waste heat recovery on the turbine inlet temperature

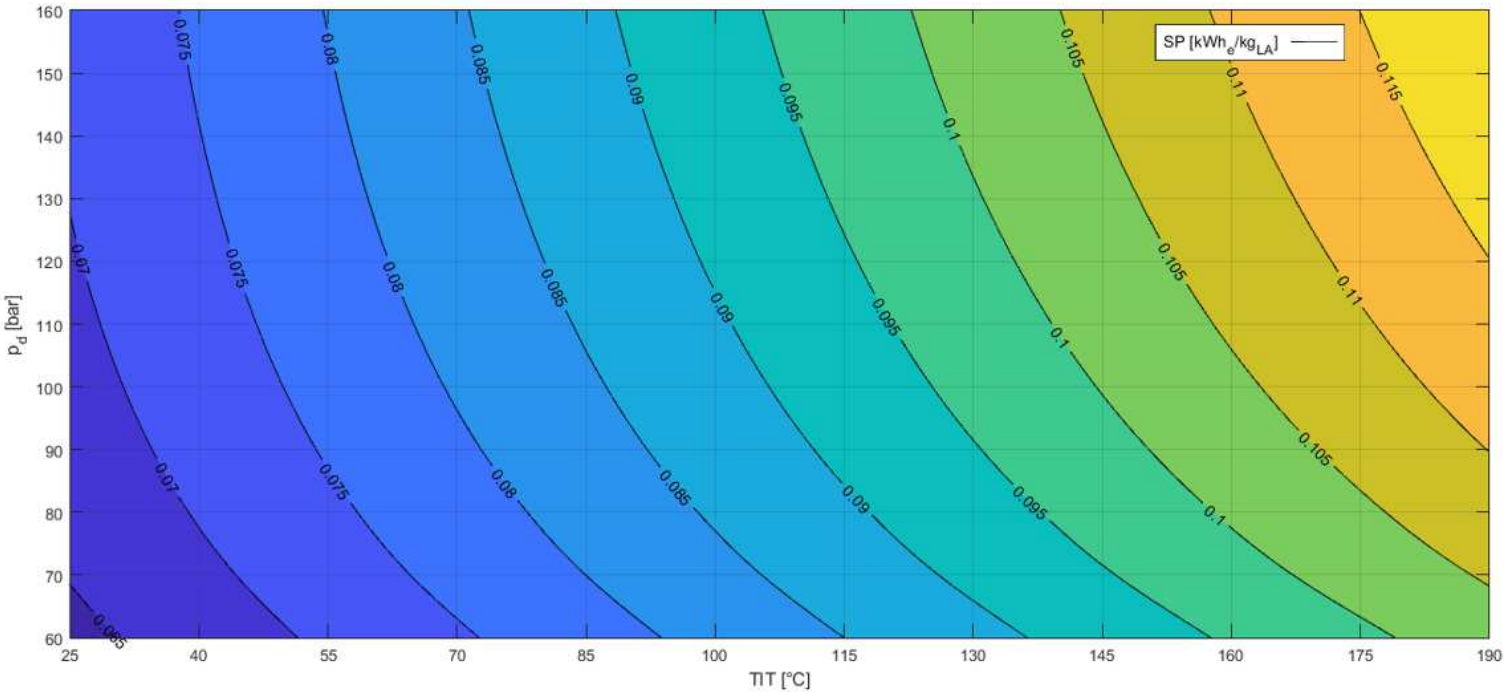

Figure A.3.: Effect of discharge pressure and Turbine Inlet Temperature on the specific electric power output

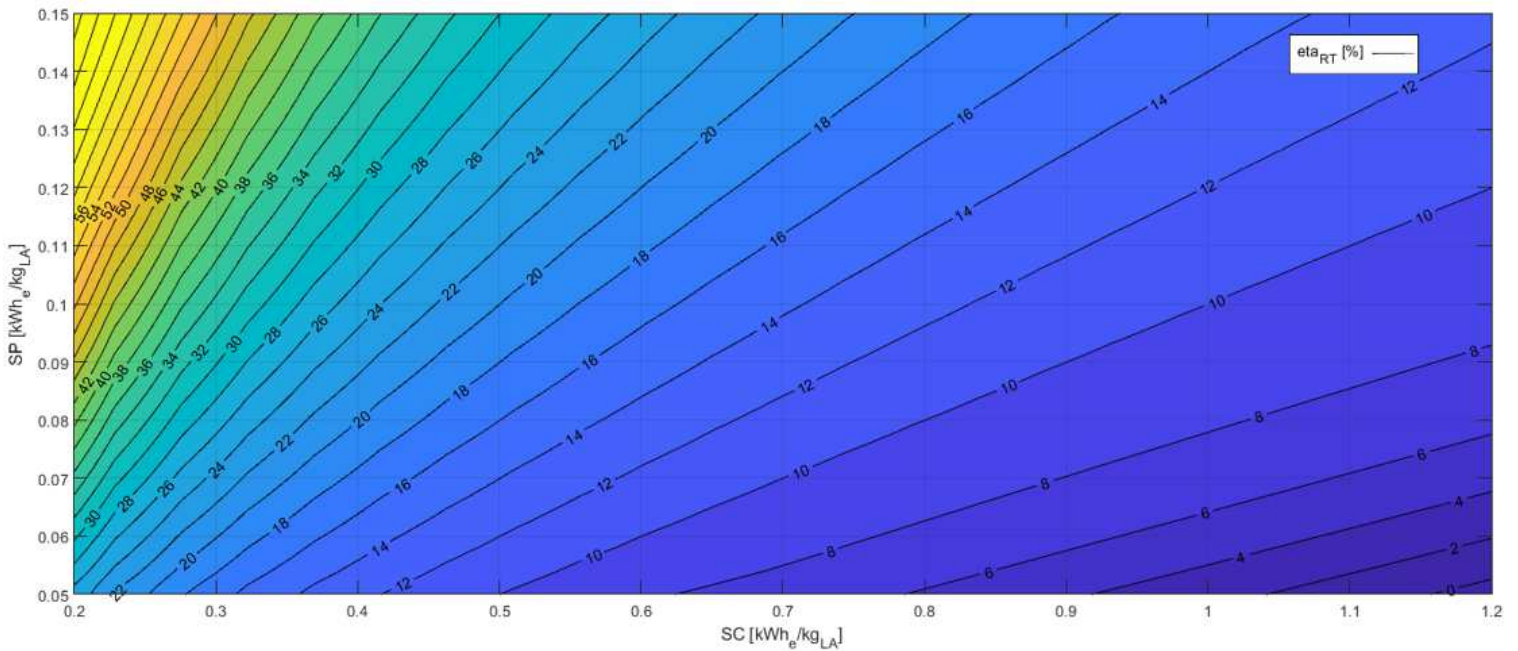

Figure A.4.: Round trip efficiency as a function of net Electric power output and liquefaction specific consumption

Appendix B.

Nomenclature

B.1. Latin Symbols

A, B, M, N	Constants for eq.4.15 and 4.16
a, s', r, e	Constants for eq.2.9
c_p	Specific heat capacity at constant pressure $[kJ/kgK]$
c_p	Specific heat capacity at constant volume $[kJ/kgK]$
c_{eff}	effective heat capacity $[kJ/kgK]$
D	Diameter $[mm]$
E	Energy stored $[kJ]$
Ex	Exergy $[kW]$
ex	Specific exergy $[kJ/Kg]$
eta_{HGCS}	Waste cold recovery efficiency
eta_{HGWS}	Waste heat recovery efficiency
f	Liquid fraction
g	gravitational acceleration $[m/s^2]$
h	Specific enthalpy $[kJ/Kg]$
k	Thermal conductivity $[W/m^2K]$
m	Mass [kg]
$\dot{m}$	Nass flow rate [kg/s]
n_c	Number of compressors

n_e	Number of expanders
P	Power $[kW]$
Pr	Prandtl number
p	pressure $[bar]$
Q	Thermal power $[kW]$
Ra	Rayleigh number
Re	Reynolds number
RMSE	Root mean square error
r	Radius $[mm]$
SC	Specific Consumption $[kWh/torkWh/kg]$
SP	Specific Electric Power output $[kWe/kg]$
s	Specific entropy $[kJ/KgK]$
T	Temperature $[K]$ or $[°C]$
t	Time $[sec]$
v	Specific volume $[m^3/kg]$
W	Work $[kWh]$
w	Specific work $[kWh/kg]$
x_{rf}	Recirculation fraction
$\Delta\Delta t$	Characteristic temperature $[°C]$

B.2. Greek Symbols

α	Thermal diffusivity $[m^2/s]$
β	Pressure ratio
η_{ex}	Exergy efficiency
η_{iso}	Isentropic efficiency

η_{poly}	Polytropic efficiency
η_{RT}	Roundtrip efficiency
Γ	Thermal expansion coefficient $[1/K]$
ρ	Density $[kg/m^3]$
υ	Dynamic viscosity $[cm^2/s]$

B.3. Subscripts

abs	Absoprtion chiller
ac	Absorber-condenser
ave	Average
CB	Cold Box
ch	Charge
$comp$	Compressor
$cont$	Container
$conv$	Convection
$cryoP$	Cryopump
$cryoT$	Cryoturbine
d	Discharge
$evap$	Evaporator
gen	generator
LA	Liquid air
net	Net
PC	Phase change
pre	Precompression
tot	Total

B.4. Acronyms

AFTC	Aftercooler
CAES	Compressed Air Energy storage
DER	Distributed energy resources
DI	Deionized
EEs	Electrical energy storages
EG	Ethylene glycol
EG30	Aqueous ethylene glycol in 30% DI water
HEX	Heat exchanger
HGCS	High grade cold storage
HGWS	High grade warm storage
HTF	Heat transfer fluid
LAES	Liquid air energy storage
ORC	Organic rankine cycle
PCM	Phase change material
PHE	Pumped Hydro Energy storage
REs	Renewable energy sources
SH	Superheaters
TIT	Discharge turbine inlet temperature

Bibliography

[1] EIA, International energy outlook 2017, access: November 2018 (2018).
URL https://www.eia.gov/

[2] IEA, Co2 emissions from fuel combustion, access: November 2018 (2017).
URL https://www.iea.org/

[3] REN21, Renewables 2018 global status report, access: November 2018 (2018).
URL http://www.ren21.net/

[4] G. Strbac, Demand side management: Benefits and challenges, Energy policy 36 (12) (2008) 4419–4426.

[5] H. Chen, T. N. Cong, W. Yang, C. Tan, Y. Li, Y. Ding, Progress in electrical energy storage system: A critical review, Progress in natural science 19 (3) (2009) 291–312.

[6] R. Amirante, E. Cassone, E. Distaso, P. Tamburrano, Overview on recent developments in energy storage: Mechanical, electrochemical and hydrogen technologies, Energy Conversion and Management 132 (2017) 372–387.

[7] G. Grazzini, A. Milazzo, Thermodynamic analysis of caes/tes systems for renewable energy plants, Renewable energy 33 (9) (2008) 1998–2006.

[8] Y. Li, H. Chen, Y. Ding, Fundamentals and applications of cryogen as a thermal energy carrier: A critical assessment, International Journal of Thermal Sciences 49 (6) (2010) 941–949.

[9] H. P. Storage, Highview power storage, Highview Power Storage, London, accessed Nov 13 (2017) 2017.

[10] D. Strahan, Liquid air technologies: a guide to the potential, Centre for Low Carbon Futures, 2013.

[11] G. Venkatarathnam, K. Timmerhaus, Cryogenic mixed refrigerant processes, Vol. 100, Springer, 2008.

[12] E. Smith, Storage of electrical energy using supercritical liquid air, Proceedings of the Institution of Mechanical Engineers 191 (1) (1977) 289–298.

[13] K. Chino, H. Araki, Evaluation of energy storage method using liquid air, Heat Transfer—Asian Research: Co-sponsored by the Society of Chemical Engineers of Japan and the Heat Transfer Division of ASME 29 (5) (2000) 347–357.

[14] H. Araki, M. Nakabaru, K. Chino, Simulation of heat transfer in the cool storage unit of a liquid–air energy storage system, Heat Transfer—Asian Research: Co-sponsored by the Society of Chemical Engineers of Japan and the Heat Transfer Division of ASME 31 (4) (2002) 284–296.

[15] B. Ameel, C. T'Joen, K. De Kerpel, P. De Jaeger, H. Huisseune, M. Van Belleghem, M. De Paepe, Thermodynamic analysis of energy storage with a liquid air rankine cycle, Applied Thermal Engineering 52 (1) (2013) 130–140.

[16] G. L. Guizzi, M. Manno, L. M. Tolomei, R. M. Vitali, Thermodynamic analysis of a liquid air energy storage system, Energy 93 (2015) 1639–1647.

[17] X. Xue, S. Wang, X. Zhang, C. Cui, L. Chen, Y. Zhou, J. Wang, Thermodynamic analysis of a novel liquid air energy storage system, Physics procedia 67 (2015) 733–738.

[18] D. Vandor, System and method for liquid air production, power storage and power release, uS Patent 7,821,158 (Oct. 26 2010).

[19] R. F. Abdo, H. T. Pedro, R. N. Koury, L. Machado, C. F. Coimbra, M. P. Porto, Performance evaluation of various cryogenic energy storage systems, Energy 90 (2015) 1024–1032.

[20] H. Chen, Y. Ding, T. Peters, F. Berger, Method of storing energy and a cryogenic energy storage system, uS Patent App. 15/053,840 (Jun. 23 2016).

[21] P. Krawczyk, Ł. Szabłowski, S. Karellas, E. Kakaras, K. Badyda, Comparative thermodynamic analysis of compressed air and liquid air energy storage systems, Energy 142 (2018) 46–54.

[22] S. Georgiou, N. Shah, C. N. Markides, A thermo-economic analysis and comparison of pumped-thermal and liquid-air electricity storage systems, Applied energy 226 (2018) 1119–1133.

[23] C. Xie, Y. Hong, Y. Ding, Y. Li, J. Radcliffe, An economic feasibility assessment of decoupled energy storage in the uk: With liquid air energy storage as a case study, Applied Energy 225 (2018) 244–257.

[24] T. H. Cetin, M. Kanoglu, N. Yanikomer, Cryogenic energy storage powered by geothermal energy, Geothermics 77 (2019) 34–40.

[25] A. J. Pimm, S. D. Garvey, B. Kantharaj, Economic analysis of a hybrid energy storage system based on liquid air and compressed air, Journal of energy storage 4 (2015) 24–35.

[26] B. Kantharaj, S. Garvey, A. Pimm, Thermodynamic analysis of a hybrid energy storage system based on compressed air and liquid air, Sustainable energy technologies and assessments 11 (2015) 159–164.

[27] P. Farres-Antunez, H. Xue, A. J. White, Thermodynamic analysis and optimisation of a combined liquid air and pumped thermal energy storage cycle, Journal of Energy Storage 18 (2018) 90–102.

[28] Y. Li, H. Cao, S. Wang, Y. Jin, D. Li, X. Wang, Y. Ding, Load shifting of nuclear power plants using cryogenic energy storage technology, Applied Energy 113 (2014) 1710–1716.

[29] J. Kim, Y. Noh, D. Chang, Storage system for distributed-energy generation using liquid air combined with liquefied natural gas, Applied Energy 212 (2018) 1417–1432.

[30] M. Antonelli, S. Barsali, U. Desideri, R. Giglioli, F. Paganucci, G. Pasini, Liquid air energy storage: Potential and challenges of hybrid power plants, Applied energy 194 (2017) 522–529.

[31] X. She, X. Peng, B. Nie, G. Leng, X. Zhang, L. Weng, L. Tong, L. Zheng, L. Wang, Y. Ding, Enhancement of round trip efficiency of liquid air energy storage through effective utilization of heat of compression, Applied Energy 206 (2017) 1632–1642.

[32] X. Peng, X. She, L. Cong, T. Zhang, C. Li, Y. Li, L. Wang, L. Tong, Y. Ding, Thermodynamic study on the effect of cold and heat recovery on performance of liquid air energy storage, Applied Energy 221 (2018) 86–99.

[33] A. Tafone, E. Borri, G. Comodi, M. van den Broek, A. Romagnoli, Liquid air energy storage performance enhancement by means of organic rankine cycle and absorption chiller, Applied energy 228 (2018) 1810–1821.

[34] S. Barsali, A. Ciambellotti, R. Giglioli, F. Paganucci, G. Pasini, Hybrid power plant for energy storage and peak shaving by liquefied oxygen and natural gas, Applied Energy 228 (2018) 33–41.

[35] T. Zhang, L. Chen, X. Zhang, S. Mei, X. Xue, Y. Zhou, Thermodynamic analysis of a novel hybrid liquid air energy storage system based on the utilization of lng cold energy, Energy 155 (2018) 641–650.

[36] G. Comodi, F. Carducci, J. Y. Sze, N. Balamurugan, A. Romagnoli, Storing energy for cooling demand management in tropical climates: A techno-economic comparison between different energy storage technologies, Energy 121 (2017) 676–694.

[37] M. Al-Zareer, I. Dincer, M. A. Rosen, Analysis and assessment of novel liquid air energy storage system with district heating and cooling capabilities, Energy 141 (2017) 792–802.

[38] N. Hatziargyriou, H. Asano, R. Iravani, C. Marnay, Microgrids, IEEE power and energy magazine 5 (4) (2007) 78–94.

[39] K. D. Timmerhaus, T. M. Flynn, Cryogenic process engineering, Springer Science & Business Media, 2013.

[40] M. Wang, R. Khalilpour, A. Abbas, Thermodynamic and economic optimization of lng mixed refrigerant processes, Energy Conversion and Management 88 (2014) 947–961.

[41] A. HYSYS, Version 8.8, Aspen Technology Inc.

[42] Messer group (2016).
URL `https://www.messergroup.com/`

[43] F. Kerry, Industrial gas handbook gas separation, Gas Separation and Purification. Boca Ratón, Florida.

[44] E. H. Hylton, H. E. Kimmel, Exducer turbines, the optimized solution for lng expanders, Ebara International Corporation, Nevada, USA.

[45] A. Kühn, F. Ziegler, Operational results of a 10 kw absorption chiller and adaptation of the characteristic equation, in: Proc. First Int. Conference Solar Air Conditioning, Bad-Staffelstein, Vol. 10, 2005.

[46] C. F. Toolbox, For use with matlab;[user's guide], Natick, MA: MathWorks.

[47] R. Morgan, S. Nelmes, E. Gibson, G. Brett, Liquid air energy storage–analysis and first results from a pilot scale demonstration plant, Applied energy 137 (2015) 845–853.

[48] A. Sciacovelli, A. Vecchi, Y. Ding, Liquid air energy storage (laes) with packed bed cold thermal storage–from component to system level performance through dynamic modelling, Applied Energy 190 (2017) 84–98.

[49] H. Peng, X. Shan, Y. Yang, X. Ling, A study on performance of a liquid air energy storage system with packed bed units, Applied Energy 211 (2018) 126–135.

[50] S. Hasnain, Review on sustainable thermal energy storage technologies, part ii: cool thermal storage, Energy conversion and management 39 (11) (1998) 1139–1153.

[51] G. Li, Y. Hwang, R. Radermacher, H.-H. Chun, Review of cold storage materials for subzero applications, Energy 51 (2013) 1–17.

[52] D. Aydin, S. P. Casey, S. Riffat, The latest advancements on thermochemical heat storage systems, Renewable and Sustainable Energy Reviews 41 (2015) 356–367.

[53] L. Hüttermann, R. Span, Investigation of storage materials for packed bed cold storages in liquid air energy storage (laes) systems, Energy Procedia 143 (2017) 693–698.

[54] P. Galione, C. D. Pérez-Segarra, I. Rodríguez, A. Oliva, J. Rigola, Multilayered solid-pcm thermocline thermal storage concept for csp plants. numerical analysis and perspectives, Applied Energy 142 (2015) 337–351.

[55] G. Zanganeh, M. Commerford, A. Haselbacher, A. Pedretti, A. Steinfeld, Stabilization of the outflow temperature of a packed-bed thermal energy storage by combining rocks with phase change materials, Applied thermal engineering 70 (1) (2014) 316–320.

[56] E. Oró, A. De Gracia, A. Castell, M. Farid, L. Cabeza, Review on phase change materials (pcms) for cold thermal energy storage applications, Applied Energy 99 (2012) 513–533.

[57] K. A. Ismail, J. Henriquez, T. Da Silva, A parametric study on ice formation inside a spherical capsule, International Journal of thermal sciences 42 (9) (2003) 881–887.

[58] R. I. ElGhnam, R. A. Abdelaziz, M. H. Sakr, H. E. Abdelrhman, An experimental study of freezing and melting of water inside spherical capsules used in thermal energy storage systems, Ain Shams Engineering Journal 3 (1) (2012) 33–48.

[59] H. Kumano, T. Asaoka, A. Saito, S. Okawa, Formulation of the latent heat of fusion of ice in aqueous solution, international journal of refrigeration 32 (1) (2009) 175–182.

[60] J. Y. Sze, C. Mu, A. Romagnoli, Y. Li, Non-eutectic phase change materials for cold thermal energy storage, Energy Procedia 143 (2017) 656–661.

[61] M. N. Ã-zisik, M. N. Özısık, M. N. Özışık, Heat conduction, John Wiley & Sons, 1993.

[62] V. Voller, C. Swaminathan, B. G. Thomas, Fixed grid techniques for phase change problems: a review, International Journal for Numerical Methods in Engineering 30 (4) (1990) 875–898.

[63] S. N. Al-Saadi, Z. J. Zhai, Modeling phase change materials embedded in building enclosure: A review, Renewable and Sustainable Energy Reviews 21 (2013) 659–673.

[64] I. Fluent, Fluent 6.3 user's guide, Fluent documentation.

[65] C. Multiphysics, User's guide, Version 4 (2007) 290–298.

[66] V. L. Brano, G. Ciulla, A. Piacentino, F. Cardona, Finite difference thermal model of a latent heat storage system coupled with a photovoltaic device: Description and experimental validation, Renewable Energy 68 (2014) 181–193.

[67] W. Zhao, S. Neti, A. Oztekin, Heat transfer analysis of encapsulated phase change materials, Applied Thermal Engineering 50 (1) (2013) 143–151.

[68] P. Lamberg, R. Lehtiniemi, A.-M. Henell, Numerical and experimental investigation of melting and freezing processes in phase change material storage, International Journal of Thermal Sciences 43 (3) (2004) 277–287.

[69] N. Amin, F. Bruno, M. Belusko, Effective thermal conductivity for melting in pcm encapsulated in a sphere, Applied Energy 122 (2014) 280–287.

[70] Z. Liao, C. Xu, Y. Ren, F. Gao, X. Ju, X. Du, A novel effective thermal conductivity correlation of the pcm melting in spherical pcm encapsulation for the packed bed tes system, Applied Thermal Engineering 135 (2018) 116–122.

[71] T. L. Bergman, F. P. Incropera, D. P. DeWitt, A. S. Lavine, Fundamentals of heat and mass transfer, John Wiley & Sons, 2011.

[72] E. W. Lemmon, M. L. Huber, M. O. McLinden, Nist reference fluid thermodynamic and transport properties—refprop, NIST standard reference database 23 (2002) v7.

[73] J. W. Schmelzer, E. D. Zanotto, V. M. Fokin, Pressure dependence of viscosity, The Journal of chemical physics 122 (7) (2005) 074511.

[74] A. Safari, R. Saidur, F. Sulaiman, Y. Xu, J. Dong, A review on supercooling of phase change materials in thermal energy storage systems, Renewable and Sustainable Energy Reviews 70 (2017) 905–919.

[75] C. Swaminathan, V. Voller, Towards a general numerical scheme for solidification systems, International journal of heat and mass transfer 40 (12) (1997) 2859–2868.

[76] N. Tay, F. Bruno, M. Belusko, Experimental validation of a cfd and an ε-ntu model for a large tube-in-tank pcm system, International Journal of Heat and Mass Transfer 55 (21-22) (2012) 5931–5940.

[77] A. Bourdillon, P. Verdin, C. Thompson, Numerical simulations of water freezing processes in cavities and cylindrical enclosures, Applied thermal engineering 75 (2015) 839–855.